# Development of an online system for characterization of irradiation-induced defects in semiconductors

Vegard Rønning

Thesis submitted for the degree of
Master of Science in Materials Science and Nanotechnology
60 credits

Department of Physics
Faculty of mathematics and natural sciences

UNIVERSITY OF OSLO

Spring / 2018

UiO : **Faculty of Mathematics and Natural Sciences**
University of Oslo

# Master's Thesis

## Development of an online system for characterization of irradiation-induced defects in semiconductors

Vegard Rønning
Materials Science and Nanotechnology
University of Oslo
Norway
Spring 2018

2018

Development of an online system for characterization of irradiation-induced defects in semiconductors

Vegard Rønning
http://www.duo.uio.no/

Trykk: Reprosentralen, Universitetet i Oslo

# Acknowledgments

First of all i would like to thank my day-to-day supervisor Christian Zimmermann, for holding up with me, answering my endless questions, and your thorough proof reading. I aslo thank you for introducing me to the world of optics and optical characterization. Secondly i would like to thank my main supervisor, Associate Professor Lasse Vines, for giving me the opportunity to work on this project, a letting my curiosity lead the way. I would also like to thank my co-supervisor Professor Edouard Monakhov for discussions on LabVIEW and electronics.

I would also thank Professor Bengt Gunnar Svensson, who introduced me to the field of semiconductor physics in my Bachelor's degree. Your passion and expertise in the field inspired me to continue with a Master's degree.

A special thanks to Viktor Bobal for always being available at the Micro- and Nanotechnology Laboratory (MiNaLab) and teaching me so much about experimental setups.

This work would not have been possible without the help and support from all om my colleagues at the Light and Electricity from Novel Semiconductor (LENS)- group. Many laughs and good times have been shared in the common lunch area that i will always remember. I thank you all.

Thanks to my family for always being there and supporting me.

Last but not least I would like to thank my beloved Sigrun Myhrvold for supporting me through this work. No matter how tough and sometimes frustrating this work has been, you always managed to lighten up my day.

I love you!

# Contents

# 1 Introduction

According to the United Nations, even today “One in five people still lacks access to modern electricity” [1]. At the same, climate change constitutes a viable threat to the livelihood and well-being of a significant portion of the global population. Hence, providing clean and affordable energy for all mankind was identified as one of the sustainable development goals of the United Nations in 2015. Semiconductors are expected to play a crucial role in achieving this goal, with energy/harvesting devices, like solar cells, or in energy-saving technologies, such as light emitting diodes or power electronics. Furthermore, semiconductors are the core component of all microtechnologies and hence the work horses of the digital society.

The success of semiconducting materials is rooted in the possibility to control and change their electrical and optical properties over a wide range. This is what makes them essential for electro-optical devices. Interestingly, it is their microscopic properties that determine their macroscopic behavior to a large extent. Tiny defects in the semiconducting material, are responsible for the wide range of properties one can obtain for the same material. These tiny defects can be intentionally introduced, e.g. impurities that act as dopants, or unintentionally. Understanding the influence and nature of the intentional as well as unintentional defects is paramount in order to make better materials, that will eventually lead to better and new devices.

One of the most sensitive way to study defects in semiconductors are so-called junction spectroscopy techniques. In junction spectroscopy, rectifying junctions, such as pn junctions or Schottky diodes, are used to study electrically-active defects in semiconductors. In such measurements, either the current or capacitance of a junction is measured, hence they belong to the group of electrical characterization techniques. Junction spectroscopy includes fairly simple techniques like Capacitance-Voltage measurements or Current-Voltage measurements as well as more advanced techniques such as deep-level transient spectroscopy. A sub class of junction spectroscopy techniques, that also probe optically-active defects, comprises techniques such as steady-state photocapacitance or deep-optical spectroscopy. These techniques have the advantage of probing optical as well as electrical properties of defects. This is an advantage exactly because in a host of applications, like solar cells or light detectors, light as well as electricity plays a role and hence both optical as well as electrical properties must be understood. One property, which is of utmost interest regarding defects is the energetic position of the corresponding defect level, because it determine to a large degree what effect the defect will have on the macroscopic material properties. These so-called defect levels can be distributed throughout the band gap of the semicondcutor.

The challenge, one has to face, when trying to perform SSPC or DLOS is the combination of an optical excitation system at variable wavelength with a system for electrical measurements. The objective of this master project was to overcome that challenge and combine these powerful tools to study defects with an ion accelerator, which is a powerful tool for generating defects in a controlled manner. Combining means of junction spectroscopy using optical excitation online with a MeV ion accelerator opens up entirely new ways to study defects in semiconductors. Online in this context means that a sample comprising a semiconducting material can be irradiated or implanted with various ions, thus introducing defects into the material, and studied directly afterwards. The setup to be modified, furthermore, allows for irradiation and ion implantation at low temperatures. This means that e.g. even very mobile intrinsic defects, like interstitial defects can be studied, because they tend to form complexes with other defects even at room temperature.

While silicon is the dominant semiconducting material today, being used in solar cells, power electronics as well as micro technologies, there are emergent materials that promise to be cheaper or exhibit better properties for some applications. One of these emerging materials is $Ga_2O_3$ . $Ga_2O_3$ is a wide band gap semiconductor (Eg = 5 eV), which has attracted interest for its possible use in power electronics and UV detectors. So far, only relatively few studies concerning electrically- and optically-active defects in $Ga_2O_3$ have been conducted and more insight into their properties is needed to make $Ga_2O_3$ more than just a promising material. Being a wide band gap semiconductor, that only exhibits n-type conductivity, junction spectroscopy techniques that utilize optical excitation are of paramount importance, because they also enable the study of the defect levels throughout the entire band gap of the material. With junction spectroscopy techniques solely utilizing thermal processes, only a fraction of the band gap is accessible.

# 2 Theory

In this chapter, the theory essential to this work related to semiconductors will be introduced. A special emphasis will be placed on defects in semiconductors and their electrical as well as optical properties. Furthermore, the fundamental principle of measurements related to electrically- and optically-active defects in semiconductors will be discussed. Finally, the main material used in the experimental work, gallium oxide ($Ga_2O_3$) will be described including its structure, material properties, and potential applications as a device.

This section is based on the works of Streetman [2], Kittel [3] and Blood & Orton [4].

## 2.1 Semiconductors

### 2.1.1 Crystals

Solids can be classified into three main categories: Crystalline solids with a long-range order, amorphous solids with only short range order and materials consisting of multiple crystalline regions, thus called polycrystalline. This work focuses on crystalline materials because of their importance in electronic devices and as model systems. Crystals are described as an almost infinitely large and continuous periodic structure of atoms in a crystal lattice. So rather than describing a crystal by its large amount of single atoms, crystals are described by their smallest unit, called the unit cell. The macroscopic crystal is just a continuous repetition of the unit cell, that by translation and symmetry represent the whole crystal in three dimensions. The orientation of the crystal surface is usually denoted with so-called miller indices, like $(h, k, l)$. The physical properties of crystals are often related to the crystal structure and can be directionally dependent.

### 2.1.2 Band Structure

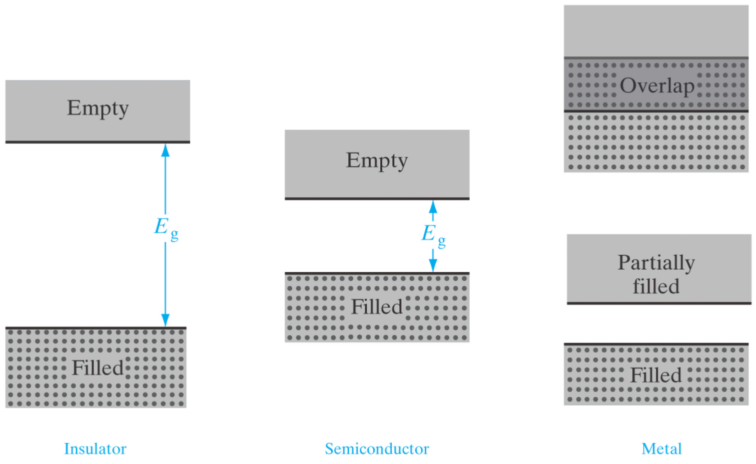

Figure 1: The representation of an insulator, semiconductor and metal/semi-metal in the energy band diagram model. From Streetman [2]

By definition, metals conduct electrical current, insulators do not, whereas semiconductors lie somewhere in between. Furthermore, the conductivity of semiconductors can be manipulated over a wide range, as will be apparent later. The conductivity stems from the electrons ability to move freely trough the solid if a voltage is applied. The band diagram of a semiconductor is made up of a conduction band (CB) and valence band (VB) with a forbidden energy gap in between. The formation of energy bands originates from the discrete energy levels of single isolated atoms, that when brought together in a solid form continuous energy bands. The primary property that determines if a material classifies as an insulator or semiconductor is the magnitude of the band gap, as illustrated in figure 1. With a sufficient transfer of energy e.g. thermal energy, electrons can be excited from the VB to the CB. Only partially-filled bands can contribute to the current flow.

### 2.1.3 Charge Carriers

Perfect semiconductor crystals, e.g. no impurities present in the material, are called intrinsic semiconductors where the intrinsic carrier concentration $n_i$ is given by

$$n_i = n = p \tag{2.1}$$

where $n$ and $p$ are the concentration of electrons in the CB and holes in the VB respectively. Holes are a quasi-particle used to describe the electrical impact of a missing electron in the VB.

Indeed, the ability to control the conductivity is what makes semiconductors suited for the use in electronic devices. The electrical conductivity of a semiconductor can change by many orders of magnitude by varying its temperature, illumination, or more importantly the impurity concentration in the semiconductor crystal. Intentionally introducing impurities into a semiconductor is called doping and is a fundamental technique for tuning material properties. When dopants dominate the electrical properties of a semiconductors it is said to be extrinsic.

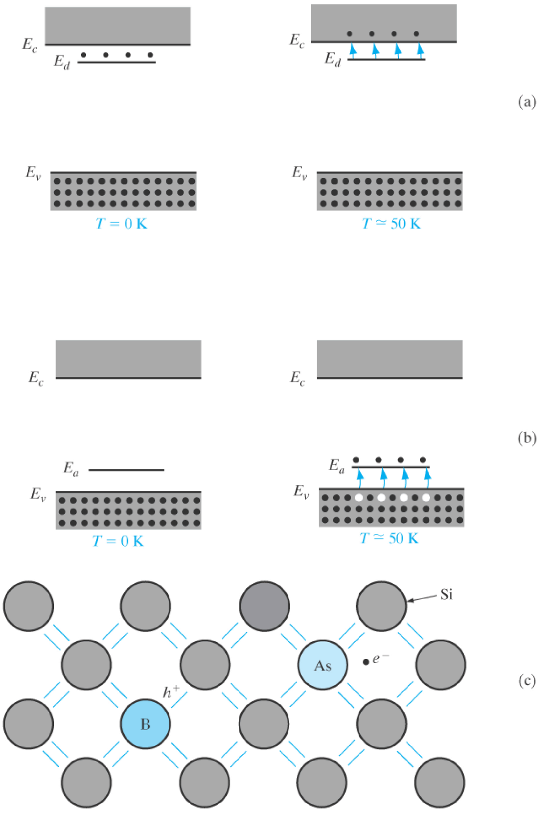

Figure 2: Illustration of dopants in Silicon (Si), presented in the energy band model (a) and b)) and the chemical bond model c). a) Show the effect of introducing a shallow donor or b) shallow acceptor and c) illustrates how substitutional donor and acceptor atoms in the covalent bond model of a Si host lattice.

The importance of doping can be described by using Silicon (Si) as an example. Si is a group IV element with four nearest neighbouring Si atoms with four valence electrons each. Due to quantum mechanical interactions between the shared electrons, two electron pairs form covalent bonds holding the structure together. By substituting a Si atom with an impurity, the spatial region of the substituted atom either increases or decreases its relative charge based on the valence of the substituted atom. Doping with lower valence atoms, breaks covalent bonds, and forms a positively charged hole while higher valence atoms introduces more electrons to the crystal as illustrated in Figure 2 c). This can be illustrated in the band diagram as follows: Impurities with lower valence form impurity states or levels, in the band gap that can accept electrons (acceptors), while higher valence impurities form energy levels that can donate electrons (donors). Figure 2 a) and b) show how electrons with sufficient energy can either be excited from the VB to a acceptor level ($E_a$) or from a donor level ($E_d$) to the CB. So-called shallow acceptors/donors have energy levels close to

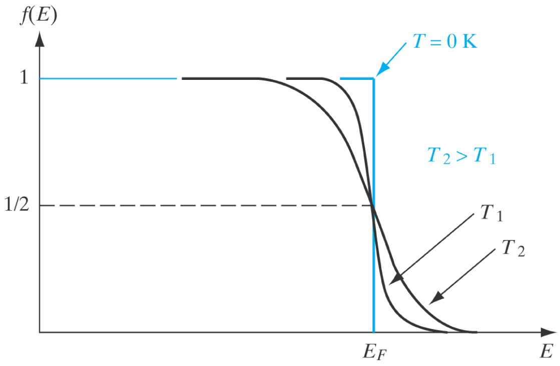

Figure 3: Temperature dependence of the Fermi-Dirac distribution function at $T$ =0 K, $T_1$ and $T_2$ where $T_2 > T_1$. At elevated temperatures the Fermi distribution has a less steep decline around $E_F$. The region of which it smears out is related to kT. From streetman [2]

the CB/VB and hence electrons can be excited even if comparatively low thermal energies are provided.

When electrons are excited from a state formed by a dopant, ionized donors (+) and acceptors (-) stay behind. The concentration of donors is denoted by $N_d$, while $N_a$ is called the concentration of acceptors. A semiconductor with a net donor doping is called a n-type semiconductor, while semiconductors dominated by acceptors are called p-type. In a n-type semiconductor, electrons are called majority carriers and holes minority carriers while the opposite applies for p-type.

Since electrons are fermions, Fermi-Dirac statistics is used to describe the distribution of electrons in the band diagram. The probability of an electron occupying an electron state with energy $E$ is given by the Fermi-Dirac distribution function

$$f(E) = \frac{1}{1 + e^{(E-E_F)/kT}} \tag{2.2}$$

where $k$ is Boltzmann's constant, $T$ denotes absolute temperature and $E_F$ is called Fermi energy. At 0 K the electron distribution is a step function at $E_F$, meaning that all electron-states below $E_F$ are occupied. Figure 3 illustrates how the probability distribution smears out around $E_f$ at elevated temperatures, enabling electrons to occupy higher energy states or the CB. The position of $E_F$ in an intrinsic semiconductor is close to the middle of the band gap, while in n- and p-type semiconductors $E_F$ is closer to the CB or VB. At elevated temperatures, $E_f$ moves toward the middle of the band gap because excitation of electrons from the VB to the CB becomes dominant. This is the case for both doped and intrinsic semiconductors.

The electron and hole concentration can be found by multiplying the density of states with the Fermi-Dirac distribution function at a given energy, and integrating over all energies as shown bellow:

$$n = \int_{E_c}^{\infty} f(E)N(E)dE \tag{2.3}$$

$$p = \int_{\infty}^{E_v} (1 - f(E))N(E)dE \tag{2.4}$$

where $E_c$ and $E_v$ is the CB and VB edge and $N(E)dE$ the density of states (DOS) in the energy range $dE$. When $E_c - E_F \gg kT$, the Fermi-Dirac distribution function (see Eq

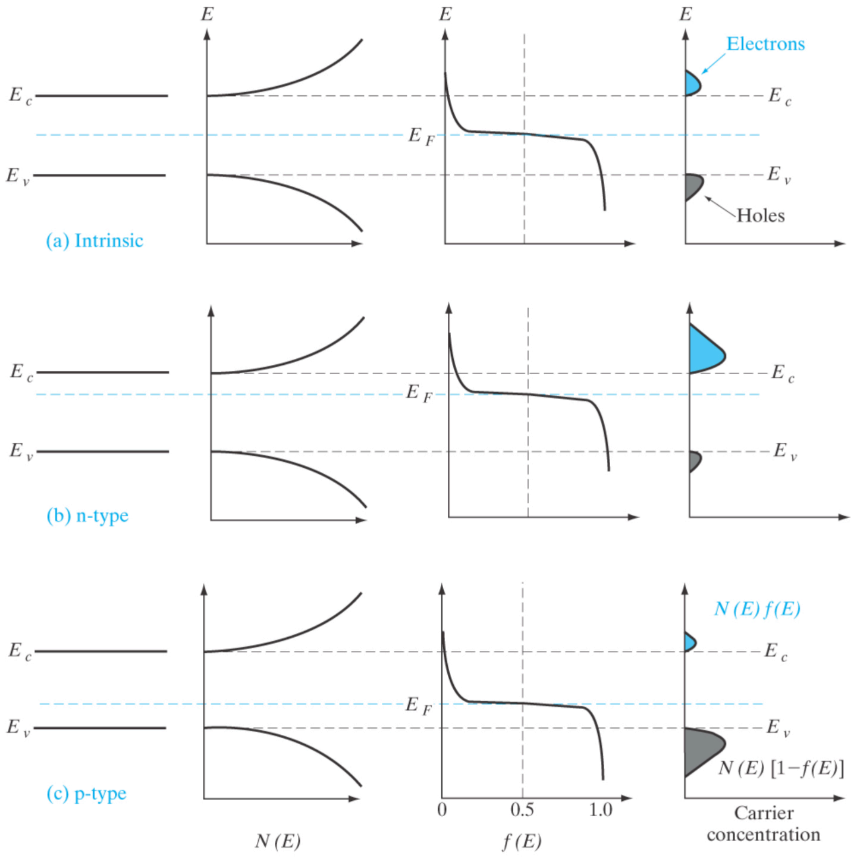

Figure 4: Illustration from left to right: band diagram, Density of states, Fermi-Dirac distribution and carrier concentration. This for (a) intrinsic, (b) n-type, and (c) p-type semiconductors at thermal equilibrium. From Streetman[2]

2.2) can be approximated by the simpler Boltzmann expression $f(E) \approx e^{-(E-E_F)/kT}$

$$n = N_d = N_c f(E_c) = N_c e^{-(E_c - E_F)/kT} \tag{2.5}$$

$$p = N_a = N_v(1 - f(E_c)) = N_v e^{-(E_F - E_v)/kT} \tag{2.6}$$

$N_c$ and $N_v$ are the effective DOS in the CB- and VB edges, respectively and given by

$$N_{(c,v)} = 2\left(\frac{2\pi m^*_{(n,p)} kT}{h^2}\right)^{\frac{3}{2}} \tag{2.7}$$

Where $m^*_{(n,p)}$ are the effective mass of electrons and holes respectively. The effective mass of electrons and holes is related to the bowing of energy bands in k-space as illustrated in figure 4 as $N(E)$. The result of equation 2.5 and 2.6 combined with equation 2.1 and the fact that in intrinsic semiconductors electrons and holes are created in pairs, the intrinsic carrier concentration can be written as

$$n_i^2 = np = N_c N_v e^{-(E_c - E_v)/kT} = N_c N_v e^{-E_g/kT} \tag{2.8}$$

This is a useful approximation since $n_i^2$ is constant at a given temperature $T$ and it still holds for doped materials due to it being independent of $E_f$.

### 2.1.4 Light absorption in the band gap

Electrons can not only be excited from the VB to the CB by thermal energy, but also by photons. This process is called light absorption. If light with an intensity $I_0$ is incident on a solid, the intensity $I_t$ of the transmitted light is described by Beer-Lambert's Law:

$$I_t = e^{-\alpha d} I_0 \tag{2.9}$$

Where $\alpha$ is the extinction coefficient, and $d$ the thickness. For the absorption process related to an electron being excited from VB to CB, $\alpha$ is often described as $\alpha = \frac{1}{E} A \sqrt{E - E_g}$ for the case of a direct band gap.

The energy of a photon, denoted as $E_{ph}$ is defined as:

$$E_{ph} = h\nu = \frac{hc}{\lambda} \tag{2.10}$$

where $h$ is Planck's constant, $\nu$ photon frequency, $c$ the light speed and $\lambda$ is wavelength. In semiconductor physics, the most commonly used unit for energy is electron volts (eV). A convenient way to calculate the photon energy in eV from wavelength (nm), or vice-versa, can be done by:

$$E_{ph}\ [\mathrm{eV}] \simeq \frac{1240\ [\mathrm{nm\,eV}]}{\lambda\ [\mathrm{nm}]} \tag{2.11}$$

Another measure of light intensity is the photon flux, $\Phi$, that is defined as the number of photons that pass through an area per unit time (second)

$$\Phi = \frac{\#\mathrm{Photons}}{\mathrm{s\ m^2}} \tag{2.12}$$

The photon flux for a given wavelength $\lambda$ can be calculated from optical power measurements since the power density $H[\mathrm{W\,cm^{-2}}]$ is defined as:

$$H(\lambda) = \frac{P(\lambda)}{A} = \Phi E_{ph}(\lambda) \tag{2.13}$$

Where $P$ is the power from the power meter, $A$ the power meter sensor area and $E_{ph}$ is given in joules. By rearranging the expression and adding the elementary charge $e$ to convert $E_{ph}$ to electron volts from joules the photon flux is given as:

$$\Phi(\lambda) = \frac{P(\lambda)}{A \times e \times E_{ph}(\lambda)} \tag{2.14}$$

### 2.1.5 Defects

Defects are often of interest in the study of semiconductors since they can alter the electrical characteristics of the material. By knowing how a defect impacts a material, one can intentionally introduce defects to controllably alter the material properties. Defects are often characterized by their dimensionality, where zero dimensional defects are called point defects. Four common point defects are: substitutional impurities which is when a foreign atom replaces a atom on the lattice site of the host material, vacancies are simply empty lattic sites in the crystal, interstitial and self-interstitial impurities are either foreign or atoms from the host material in non-lattice site.

#### 2.1.5.1 Charge carriers interaction with traps

As mentioned in section 2.1.3, impurities can introduce new energy states in the band gap and e.g. act as donors or acceptors. In general, impurities or intrinsic point defects can introduce energy states within the entire band gap and are usually divided in to two classes: shallow and deep traps. Shallow electron traps are located close to the CB-edge, while deep electron traps are formed further away from CB, but still in the upper part of the band gap. The opposite is true for holes, where shallow hole traps are close to the VB-edge and deep hole traps further into the bandgap Traps that are close to the middle of the band gap are of special importance because they can act as recombination centers for electrons and holes. The energy difference between a trap-level and the relevant band edge is labeled $E_t$. The concentration of traps is denoted by $N_t$. Trapping denotes the case when a state captures a charge carrier, inhibiting its ability to contribute to conduction. Recombination is when both an electron and a hole are captured and annihilate. The way charge carriers interact with traps is important since there can be multiple traps in the band gap and the electronic interplay contribute e.g. to the semiconductors conductivity.

### Capture- and emission rates

In order to extract information about the characteristics of traps it is not only sufficient to know the total amount of traps $N_t$, but also the trap occupancy $n_t$. Figure 5 illustrates the four dynamic capture and emission processes for electrons and holes that characterize the interplay between traps and charge carriers.

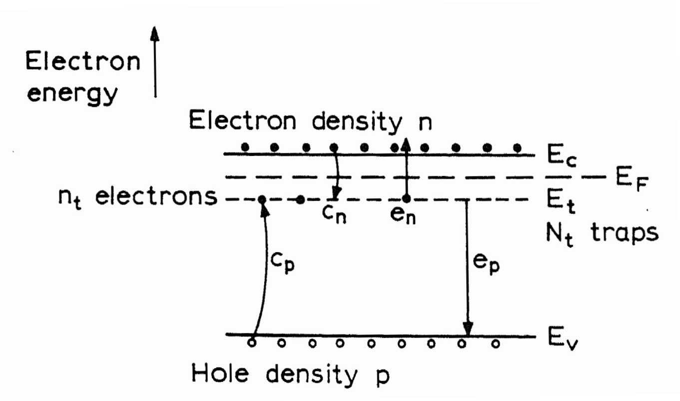

Figure 5: Illustration of electron and hole emission and capture processes for a trap at energy $E_t$ and trap density $N_t$ contain $n_t$ electrons. In the semiconductor, $E_C$ have a electron density of $n$, $E_V$ a hole density of $p$ and a Fermi level at $E_F$. From Blood & Orton [4]

The capture rate for electrons $c_n$ is characterized by its capture cross section $\sigma_n$, and is defined as:

$$c_n = \sigma_n \langle v_n \rangle n \tag{2.15}$$

Where $\langle v_n \rangle n$ is the flux of electrons(at thermal velocity) per unit area per unit time that a trap is exposed to. A similar expression holds for holes

$$c_p = \sigma_p \langle v_p \rangle p \tag{2.16}$$

Emission on the other hand is the competing process of carrier capture. Where an electron or hole is emitted from the defect level to CB or VB, respectively, and denoted as $e_n$ as the electron emission rate and $e_p$ the emission rate of holes. In the case of a n-type material, as shown in figure 5 the trap occupancy $n_t$ describe how traps occupied by electrons emit electrons or capture holes $(e_n + c_p)$, and how empty traps $(N_t - n_t)$ capture electrons or emit holes $(c_n + e_p)$. The net rate of change of electron occupancy is given as:

$$\frac{dn_t}{dt} = (c_n + e_p)(N_t - n_t) - (e_n + c_p)n_t \tag{2.17}$$

### Thermal equilibrium

At thermal equilibrium the net occupancy do not change, which leads to the detailed balance:

$$e_n n_t = c_n(N_t - n_t) \tag{2.18}$$

$$c_p n_t = e_p(N_t - n_t) \tag{2.19}$$

Then $\hat{n}_t$ can be expressed by rearranging the equilibrium occupancy to

$$\frac{\hat{n}_t}{N_t} = \frac{c_n}{c_n + e_n} = \frac{e_p}{e_p + c_p} \tag{2.20}$$

Furthermore, since the occupancy is in thermal equilibrium, it can be expressed by the Fermi-Dirac distribution function for a deep state at energy $E_t$ with degeneracy $g_0$ when empty of electrons and $g_1$ when occupied by a single electron as:

$$\frac{\hat{n}_t}{N_t} = \left(1 + \frac{g_0}{g_1} e^{\frac{(E_t - E_F)}{kT}}\right)^{-1} \tag{2.21}$$

The ratio between $g_0$ and $g_1$ is close to unity, so by combining equation 2.20 and 2.21 and neglecting the degeneracy expressions for the capture and emission rate for charge carrier is:

$$\frac{e_n}{c_n} = e^{\frac{E_t - E_F}{kT}} \tag{2.22}$$

$$\frac{e_p}{c_p} = e^{\frac{E_F - E_t}{kT}} \tag{2.23}$$

By examining the special case where $E_t = E_F$ it is clear that the capture and emission rates are close to unity. This imply that the the Fermi level position, relative to the trap level gives information on the trap occupancy. If the Fermi level is higher than the trap level, $c_n$ and $e_p$ dominates so that the trap is occupied. Inversely, lower $E_F$ suggests that the trap is empty since $c_p$ and $e_n$ dominates.

As mentioned, the carrier emission are the competing process to carrier capture from equation 2.15 and 2.16. Unlike the capture rate, which is dictated by the materials doping concentration, the emission rates is an intrinsic property of a trap. An expression for the electron emission rate can be found by combining equation 2.15, 2.22 and 2.5 to:

$$e_n(T) = \sigma_n \langle v_n \rangle N_C e^{-(E_C - E_t)/kT} \tag{2.24}$$

where several of the factors in the expression have a temperature dependency:

$$\langle v_n \rangle = \left(\frac{3kT}{m^*}\right)^{3/2} \tag{2.25}$$

$$N_C = 2M_C \left(\frac{2\pi m^* kT}{h^2}\right)^{3/2} \tag{2.26}$$

Here $m^*$ is the effective mass of the energy band and $M_C$ the number of conduction band minima. Furthermore, the temperature dependency of a capture cross section with activation energy $\Delta E_\sigma$ and $\sigma_\infty$ corresponding to the extrapolated value for infinite temperature is:

$$\sigma_n(T) = \sigma_\infty e^{-\frac{\Delta E_\sigma}{kT}} \tag{2.27}$$

By inserting the above equations in to Eq. 2.24 a more precise expression for the temperature dependence of electron emission rate is given as:

$$e_n(T) = \gamma T^2 \sigma_{na} e^{-\frac{E_{na}}{kT}} \tag{2.28}$$

Where the capture cross section is modified by the degeneracy as $\sigma_{na} = \frac{g_0}{g_1}\sigma_\infty$ and the physical constants are captured in $\gamma = 2\sqrt{3}M_C(2\pi)^{3/2}k^2 m^* k^{-3}$. The activation energy $E_{na}$ deviates from $E_t$ by a factor of $\Delta E_\sigma$ and is given by: $E_{na} = (E_C - E_t) + \Delta E_\sigma$. It is important to note that $(E_C - E_t)$ is assumed to be temperature independent.

Experimental techniques like DLTS utilize equation.2.28 to characterize traps in a semiconductor. Plotting $e_n/T^2$ as a function of inverse temperature in a semi-logarithmic plot produces a straight line, where $\sigma_{na}$ is the extrapolated intercept with the y-axis and $E_{na}$ from the slope. The values for $E_{na}$ and $\sigma_{na}$ extracted this way does not represent the real capture cross section or the ionization energy of the trap. In order to do so, Gibbs free energy has to be taken in to account so that equation 2.24 becomes:

$$e_n(T) = \sigma_n \langle v_n \rangle N_C e^{-\frac{\Delta G}{kT}} \tag{2.29}$$

$$e_n(T) = e^{\frac{\Delta S}{k}} \sigma_n \langle v_n \rangle N_C e^{-\frac{\Delta H}{kT}} \tag{2.30}$$

This shows that $E_{na}$ is the enthalpy of the ionization and the capture cross section has a added entropy term $\sigma_{na} = e^{\frac{\Delta S}{k}}\sigma_n$.

Values for $\Delta H$ and $\sigma_{na}$ can be extracted from an Arrhenius plot, so by collecting the temperature independent terms $\langle v_n \rangle$ and $N_C$ in $\beta$, Eq. Eq. 2.30 becomes:

$$\ln\left(\frac{e_n}{T^2}\right) = -\frac{\Delta H}{kT} + \ln(\beta\sigma_{na}) \tag{2.31}$$

### Transient respons

For convenience, expressions for the sum of all emission or capture rates contributing to electron gain $a$ or electron loss $b$ in traps can be derived as:

$$a = \sum \text{rates of "electron gain"(e.g. } c_n + e_p) \tag{2.32}$$

$$b = \sum \text{rates of "electron loss"(e.g. } e_n + c_p) \tag{2.33}$$

Then equation 2.17, that describe the change in electron occupancy per time can be simplified to:

$$\frac{dn_t}{dt} = a(N_t - n_t) - bn_t \tag{2.34}$$

Transients refers to an event within a short time frame. Spectroscopic techniques like DLTS uses short electrical pulses and measure the subsequent transient response to characterize the dynamic of emission from traps. To understand the transient behaviour of a semiconductor we start by the general solution of equation 2.34 when $n_t = n_t(t = 0)$ is:

$$n_t(t) = \frac{a}{a+b}N_t - \left(\frac{a}{a+b}N_t - n_t(0)\right) e^{-(a+b)t} \tag{2.35}$$

The steady state occupancy is when $t = \infty$:

$$n_t(\infty) = \frac{a}{a+b}N_t \tag{2.36}$$

and more generally:

$$n_t(t) = n_t(\infty) - (n_t(\infty) - n_t(0))e^{-t/\tau} \tag{2.37}$$

Where $\tau$ is the time constant given by:

$$\tau = (a+b)^{-1} = (e_n + c_n + e_p + c_p)^{-1} \tag{2.38}$$

From the above it can be seen that a momentary change in the initial occupancy causes a exponential relaxation to the steady state occupancy according to the time constant. When a trap is initially empty, $n_t(t)$ increases with time or when a trap is initially full, $n_t(t)$ decreases with time:

$$n_t(t) = \begin{cases} n_t(\infty)\left(1 - e^{-t/\tau}\right) & \text{when} \quad \mathrm{n}_t(0) = 0 \qquad (2.39\text{a}) \\ \dfrac{a}{a+b}N_t + \dfrac{b}{a+b}N_t e^{-t/\tau} & \text{when} \quad \mathrm{n}_t(0) = N_t \qquad (2.39\text{b}) \end{cases}$$

#### 2.1.5.2 Optically induced effects on trap

In this section, the optical counterpart to the thermal emission rates and how they interact with traps will be discussed. In order to distinguish between thermal and optical emission rates, $e_n^{th}$ and $e_p^{th}$ denotes the thermal emission rates, where as $e_n^o$ and $e_p^o$, denotes the optical emission rates fro electrons and holes respectively. The capture rates on the other hand are thermal in nature and is often assumed to be unaffected by illumination, so that Eq 2.15 and 2.16 still holds.

The optical emission rate $e_{n,p}^o$ is defined by the incident photon flux $\Phi(E_{ph})$ and the optical cross section $\sigma_{n,p}^o(E_{ph})$ for of electrons or holes respectively.

$$e_{n,p}^o = \Phi(h\nu)\sigma_{n,p}^o(h\nu) \tag{2.40}$$

Unlike the thermal emission rates that can be described only by the trap properties and temperature, the optical emission rates also depend upon local photon flux. This causes the optical cross section to be the trap characteristic of interest, rather than the rates themselves. Quantifying the absolute local photon flux is often challenging since surface reflections and the competing absorption in the depletion region have to be taken into account.

The Lucovsky[5] model states that the optical cross section have the proportionality

$$\sigma^o \propto \frac{1}{E_i}\left[\left(\frac{E_i}{E_{ph}}\right)\left(1 - \frac{E_i}{E_{ph}}\right)\right]^{3/2} \tag{2.41}$$

where $E_i$ is an ionization energy. Figure 6 illustrates the shape of the optical cross section as a function of photon energy. This simple model have in some cases shown good agreement with experimental data for $\sigma^o(E_{ph})$, but there are also many cases where it does not. It shows that the optical cross section is zero for photon energies lower than the ionization energy $E_i$, thus optically induces emission do not occur. Furthermore, it shows that the maximum value for $\sigma^o$ occur at $E_{ph} = 2E_i$ and slowly decay with increased photon energies. This contrasts with shallower states with a hydrogenic nature, where the maximal value of the cross section occur at the peak ionization threshold. This approximation is useful in the way that it shows that the optical cross section of deep traps can be found by the ionization threshold at $E_i$.

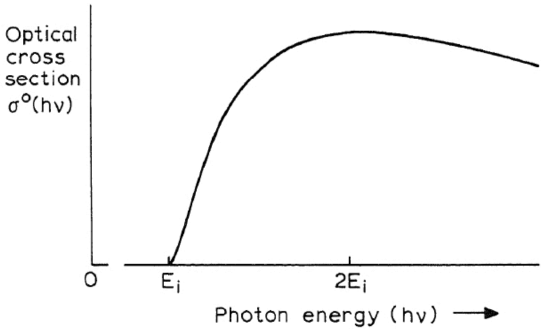

Figure 6: The shape of optical emission cross section $\sigma^o(E_{ph})$ as function of photon energy $E_{ph}$ according to the Lucovsky model[5]

When considering optical emission processes, it is beneficial to do so within a depletion region. The principal advantage is that the relative emission rates for electrons and holes dominate, such that the capture rates can be neglected. To extract information about the trap occupancy from optical stimuli, one has to differentiate between thermal and optical emission. The simplest way to suppress the thermal emission rate is to reduce temperature so that the optical emission dominates.

In principle, the steady state occupancy for traps given by Eq. 2.36 also holds for traps under illumination, but with the added contribution of $e_n^o$ and $e_p^o$. By suppressing the thermal processes however, so that the assumption $c_n, c_p, e_n^{th}, e_p^{th} \ll e_n^o e_p^o$ holds, the optical steady state occupancy, denoted as $n_t^o$ is given by

$$n_t^o(\infty) = \frac{e_p^o}{e_n^o + e_p^o} N_t \tag{2.42}$$

Similarly, the optical transient response is given by Eq. 2.35, so with the assumption that the optical emission dominates:

$$n_t^o(t) = n_t^o(\infty) - \left[n_t^o(\infty) - n_t^o(0)\right] e^{-(n_n^o + n_p^o)t} \tag{2.43}$$

The above expressions assumes an ideal case, but one can not necessarily assume that only the optical emission rate is dominant. More generally the steady state occupancy is given with the additional thermal contributions as:

$$n_t^o(\infty) = \frac{e_p^o + e_p^{th}}{e_n^o + e_n^{th} + e_p^o + e_p^{th}} N_t \tag{2.44}$$

It is assumed that illumination does not modify the capture rates. In general the electron capture rate $c_n$ at depth $x^0$ is defined by

$$c_n(x^0) = e_n^o + e_n^{th} + e_p^o + e_p^{th} \tag{2.45}$$

So with the assumption that when all thermal emission rates can be neglected:

$$c_n(x^0) = e_n^o + e_p^o \tag{2.46}$$

## 2.2 pn-junction

When bringing a n- and p-type semiconductor together, a pn-junction is formed in the intersection. In the following, homogeneous doping concentration in both materials as well as a sharp interface is assumed.

The difference in mobile charge carriers in the two materials of different doping leads to diffusion and drift of charge carriers between the materials. Figure 7a illustrates the processes in a pn-junction at equilibrium. Charge carriers that diffuse across the junction leave behind ionized dopant atoms. These atoms have opposite polarity on either side of the junction, thus inducing a electric field over the junction that introduces a drift current that inhibits diffusion of mobile charge carriers. At some point the drift current and diffusion current equalize and hence a dynamic equilibrium is reached.
In order to describe properties of junctions some assumptions are made: The depletion region formed on either side of the junction is described with a depletion depth $x_{n,p}$ on n- and p-side respectively. To simplify the deduction, the depletion region is assumed to be a void of free charge carriers. On the n-side only ionized donors, $N_d^+$, are present in the depletion layer, while on the p-side only ionized acceptors, $N_a^-$, can be found. Within the depletion region, the total charge $Q$ is equal to the amount of dopant ions on either side of the junction. In addition, the electric field induced by the dopant ions is assumed to be confined within the depletion region. This implies that the depth of the depletion region on either side depends on the relative doping concentration on each side. Thus, the charge $Q$ can be described by

$$|Q| = eAN_dx_n = eAN_ax_p \tag{2.47}$$

Where $e$ is the elementary charge, $A$ the junction area and $x_{n,p}$ depletion depth on n- and p-side. The electric field, $\mathcal{E}$ can be found by solving the Poisson equation $\Delta^2 V = -\Delta\mathcal{E} = \rho/\varepsilon$, with $\rho$ as charge density, $\varepsilon$ the permitivity so that the maximal possible electric field is:

$$\mathcal{E}_0 = -\frac{q}{\varepsilon}N_dx_n = -\frac{q}{\varepsilon}N_ax_p \tag{2.48}$$

Since the field is set up by localized ionized atoms in the junction it can be expressed as a spatial variation in the potential of the junction as

$$\mathcal{E}(x) = -\frac{dV(x)}{dx} \tag{2.49}$$

In the depletion approximation, the built-in voltage $V_0$ defined as the potential difference between the n- and p-side due to the potential being constant outside the depletion region at $V_n$ and $V_p$ (see Fig.7a), thus $\mathrm{V}_0 = \mathrm{V}_n$-$\mathrm{V}_p$ and can be expressed by

$$-V_0 = \int_{-x_p}^{x_n} \mathcal{E}(x)\ dx = \frac{\mathcal{E}_0 W}{2} \tag{2.50}$$

$$V_0 = \frac{qN_dx_nW}{2\varepsilon} \tag{2.51}$$

The potential difference at the junction causes a relative shift in the band structure so that the Fermi-level is constant throughout the material in equilibrium. With this an expression for the depletion width can be derived with respect to doping concentration. Since $W = x_n + x_p$, it follows that:

$$x_n = \frac{N_a}{N_d + N_a} \tag{2.52}$$

so that

$$V_0 = \frac{qW^2}{2\varepsilon}\left(\frac{N_dN_a}{N_d + N_a}\right) \tag{2.53}$$

$$\Rightarrow W = \left(\frac{2\varepsilon V_0}{q}\left(\frac{N_a + N_d}{N_aN_d}\right)\right)^{1/2} \tag{2.54}$$

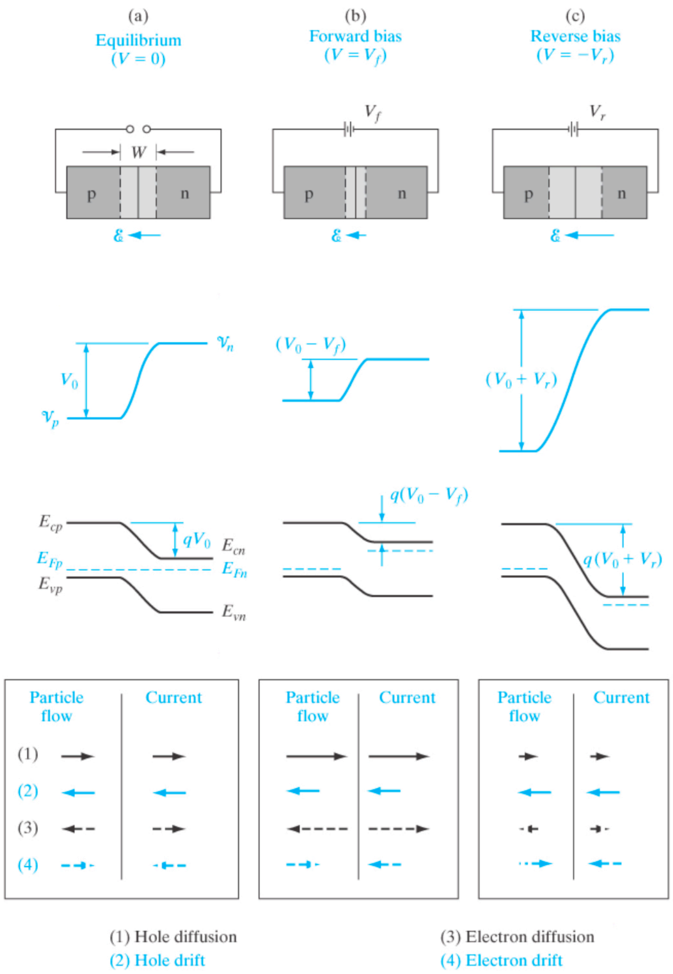

Figure 7: Schematic of equilibrium (a), forward bias (b) and reverse bias (c) on a pn-junction. From top to bottom: Electrical field and depletion region, elecrostatic potential, energy band diagram and particle-/current flow. From Streetman[2]

This representation of the depletion width $W$ clearly shows the relationship between some of the key parameters that material characterization techniques based on pn-juntions utilize. Equation 2.54 assumes equilibrium and in reality systems are often not in a steady-state. The drift current is dictated by the internal electrical field in the junction which can be tuned by an external electrical field or simply an external bias voltage. Due to the close relationship between diffusion and drift current an external bias voltage alters the contact potential such that a total junction voltage can be derived as $V_j = V_0 - V$, where $V$ is the applied bias. Figure 7 illustrates how a pn-junction is influenced by applied bias. In order to illustrate the potential difference of a biased junction two points of reference have to be defined on either side of the junction. Since the Fermi level is only defined at equilibrium conditions, quasi Fermi levels are used with a separation of $qV$. The polarity of the applied bias $V$ has to be taken in to account, denoted as either to be a forward- or reverse bias. Applying positive voltage $V$ to the p-side of a pn-junction is defined as forward bias. This decreases the total junction potential, thus lowering the electrical field which causes an exponential increase in diffusion current. In a band diagram this is illustrated as a lowering in the potential barrier height. Reverse bias causes a broadening of $W$ illustrated as an increase in barrier height and an electrical field in the junction that reduces the diffusion current. It is important to note that in an ideal case, although the increased field causes the drift current to dominate inside the junction, the current flowing through the junction does not depend on the magnitude of the reverse bias. Instead, the rate of which minority carriers arrives at the depletion region edge limits the current through a reverse biased junction and depends on the diffusion properties and carrier concentration of the junction materials. This asymmetric behaviour with respect to conductance means that the junction behaves like a diode which only conducts current in one direction. This IV characteristic is this often denoted as rectifying. The total current through a pn-junction as a function of applied voltage is expressed by the ideal diode equation.

$$I(V) = I_0 \left( e^{\frac{qV}{kT}} - 1 \right) \tag{2.55}$$

where $I_0$ is the reverse saturation current and only describe the ideal case of a diode. A real diode is not perfect and an ideality factor $n$ is introduced to take some deviations from ideality into account.

$$I(V) = I_0 \left( e^{\frac{qV}{nkT}} - 1 \right) \tag{2.56}$$

Deviations compensated by the ideality factor can for example be recombination processes in the depletion region. Reverse biasing increases the electrical field in the junction, sweeping carriers across before recombination can occur. Forward biasing can induce significant recombination of carriers that may cause deviations in $I$ compared to the ideal behaviour. Furthermore, shunts can often alter the diode characteristics. At high forward biases the series resistance can also significantly influence the current through a pn-juntion.

## 2.3 Metal-semiconductor junctions

The previous section considered junctions between two semiconductor materials. However, a similar behaviour can be achieved by combining a semiconductor with an appropriate metal.

Metal-semiconductor(MS) junctions are commonly used for contacting purposes. This is due to the simplicity of their fabrication. MS contacts can be applied to a clean semiconductor surface by simply depositing an appropriate layer of metal. Contact shape and size can be designed by either lithography methods or simply shadow masking the surface during metal deposition.

Both rectifying and non-rectifying behaviour can be achieved, called Schottky and Ohmic respectively, and is described by the relative difference in the work function of the metal and semiconductor. The work function of a metal $q\Phi_m$ is defined as the energy separation of the Fermi level and vacuum level. This is also the case for the semiconductor work function $q\Phi_a$. Another parameter of importance is the separation between the vacuum level and semiconductor conduction band minimum, called the electron affinity $\chi$. These quantities are illustrated in Fig.8.

For a n-type semiconductor, ohmic contacts are formed if $\Phi_m < \Phi_s$. If on the other hand $\Phi_m > \Phi_s$, a rectifying contact (Schottky) is formed, which can be described analogously to pn-juntions with a very heavily doped part (metal). The built-in voltage $V_0$ is ideally defined as $qV_0 = q(\Phi_m - \Phi_s)$. For p-type semiconductors the opposite applies, such that rectifying contacts form when $\Phi_m < \Phi_s$ and ohmic ones when $\Phi_m > \Phi_s$.

In real systems however, non-ideal interfaces may form. Semiconductor surfaces contain surface states due to unsaturated covalent bonds and impurities can introduce defect states in the band gap. Bardeen [6] describes the influence of electron states as pinning the Fermi-level. This pinning effect can reduce the influence of the metal work function on the barrier height. The current-voltage relationship of a Schottky contact is based on a similar diode equation as for a pn-diode. The Schottky contact, however, mainly conducts majority carriers across the junction.

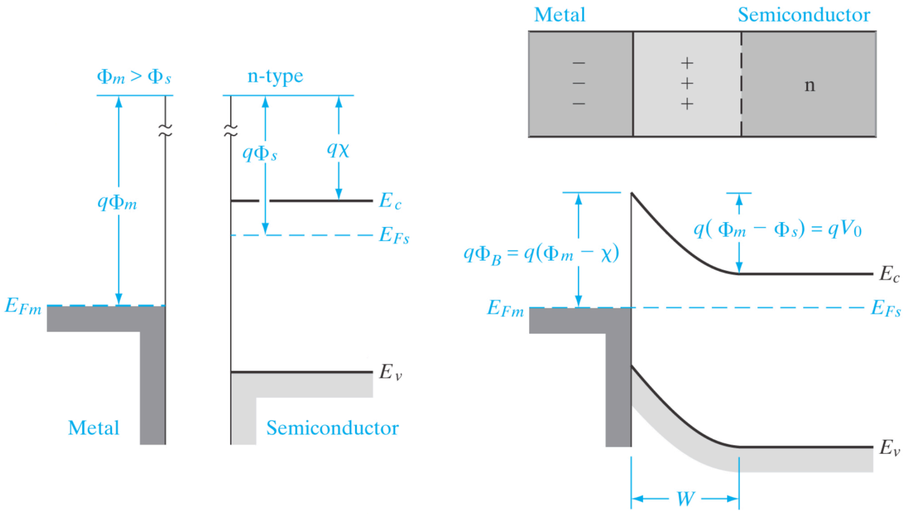

(a) (b)

Figure 8: Schematic of a Metal and Semiconductor before (a) and after (b) put together to form a Schottky junction. From Streetman[2]

## 2.4 Depletion capacitance

The arrangement of charges in the depletion region of a pn or MS junction share some similarities to a parallel plate capacitor known from electronics. This is used to describe the relation between measured capacitance and properties of a junction. The separation of charges on either side of a junction is given by $W$ and varies based on applied bias and charge carrier concentration. Capacitance is the the ability for a material to store charge $Q$. Capacitors with a linear capacitance-voltage relationship are described by $C = Q/V$. Since the charge on each side in the depletion region varies non-linearly with applied bias, a more general definition is:

$$C \equiv \left| \frac{\Delta Q}{\Delta V} \right| \tag{2.57}$$

From the section above, the relationship between charge and depletion width can be derived by inserting equation 2.47 into equation 2.52, yielding the expression:

$$|Q| = qA \left( \frac{N_d N_a}{N_d + N_a} \right) W \tag{2.58}$$

A general expression for depletion capacitance can be found to be

$$C = \varepsilon A \left( \frac{q}{2\varepsilon(V_0 - V)} \left( \frac{N_a N_d}{N_a + N_d} \right) \right)^{1/2} = \frac{\varepsilon A}{W} \tag{2.59}$$

which is equivalent to the solution for a parallel plate capacitor. In the case of an asymmetric junction, e.g., an MS-contact or a pn-junction where one side is much more heavily doped, the depletion region extends primarily into the less heavily doped side. Simplifying equation 2.59, the capacitance is then determined by the doping concentration of the less heavily doped side $N_{a,d}$ of the junction:

$$C = A \left( \frac{q\varepsilon}{2(V_0 - V)} N_{a,d} \right)^{1/2} \tag{2.60}$$

This is also the case for MS junctions.

## 2.5 Gallium oxide

After the early work on $Ga_2O_3$ in the mid 1900s, the material has received a renewed and intense interest in the last few years due to its intriguing properties and applications with power electronics and UV devices.

The following description of $Ga_2O_3$ is based on the works of Geller[7], Ahman[8] and Romanov[9].

$Ga_2O_3$ can form several different polymorphs ($\alpha$-, $\beta$-, $\gamma$-, $\delta$-, $\varepsilon$-), where $\beta$-$Ga_2O_3$ is of interest in this work. $\beta$-$Ga_2O_3$ is the most common and well-studied polymororph and exhibit a band gap of 4.85 eV at room temperature (RT). It has a monoclinic crystal structure and belongs to space group C2/m shown in Fig.9. $\beta$-$Ga_2O_3$ is the only polymorph that is stable through out the whole temperature range to the melting point at ~1795 °C. The thermal stability of $\beta$-$Ga_2O_3$ enables bulk single crystal and epitaxial films to be produced by crystallistation from a melt or vapour phase epitaxy. This makes production potentially very cost effective, since these production techniques are well established for other materials, including Si.

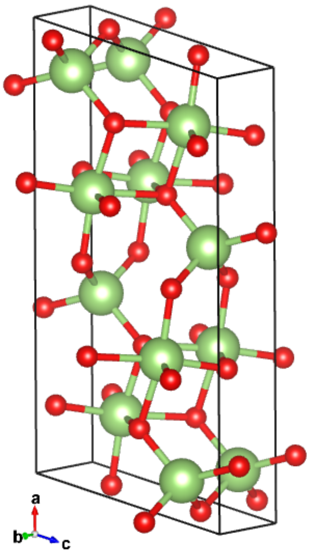

Figure 9: Illustration of the conventional unit cell of $\beta$-$Ga_2O_3$ generated by first principle calculations.

| **Property** | **Value** |
|---|---|
| Crystal structure | monoclinic |
| Symmetry group | C2/m |
| Lattice parameters | |
| a | 12.214 Å |
| b | 3.0371 Å |
| c | 5.7981 Å |
| $\beta$ | 103.83° |
| Density | 5.95 $g\,cm^{-3}$ |
| Dielectric constant | 9.9-10.2 |
| Melting point | 4.85±0.1 eV |
| Refractive index | |
| @532 nm | |
| \|\|[010] | 1.9523 |

Table 2: Physical properties of $\beta$-$Ga_2O_3$ . From [9]

The unit cell of $\beta$-$Ga_2O_3$ is illustrated in figure 9, Gallium occupy two crystallographically inequivalent sites, Ga(I) has tetrahedral geometry, and Ga(II) octahedral geometry. Oxygen on the other hand, have three crystallographically different sites: O(I), O(II) and O(III) where two are coordinated trigonally and one is coordinated tetrahedrally.

Being a wide band gap semiconductor, $\beta$-$Ga_2O_3$ is colorless and highly transparent for visible light with wavelengths higher than ~255 nm. It usually possess n-type conductivity, which are normally attributed to Si or Sn impurities substituting on the Ga site in $\beta$-$Ga_2O_3$ . Colorations in the crystal can occur due to impurities from production, where n-type crystals have a bluish coloration. The bluish coloration is often attributed to absorption of light by free carriers in the red and near infra-red (NIR)[9].

# 3 Experimental methods

The purpose of this section is to present the experimental methods used in this work and the components need to do so. The focus will be on how the experimental setup utilize some of the fundamental concepts presented in the theory section. The buildup and operation will be highlighted as well.

The techniques presented in this thesis are well established in the scientific community. Characterization techniques such as IV, CV and DLTS are already developed in the lab, but with older versions of LabVIEW, with some programs dating more than 15 years back. The issue with old program-code is that it is often based on out-dated programming conventions that often are computationally inefficient, and also challenging to maintain. In particular, when older programs is based on internal code that is no longer supported, backwards compatibility often becomes and issue with newer versions of the LabVIEW software. Utilizing the computational power of modern systems and increasing scalability was achieved by rewriting most of the code. Other programs for techniques such as SSPC had to be designed from the ground up based on theory acquired in literature.

The hardware used will be presented and as well as the experimental techniques used in sample preparation.

## 3.1 Characterization techniques

### 3.1.1 Current-Voltage

Current-voltage (IV) measurements are commonly used to characterize contact performance and quality of a diode. In this work, IV measurements were used as a qualitative method for investigating rectification properties and stability of manufactured diodes. More information about the material and the contact (see Sec. 2.3) can be obtained from IV measurements, e.g., the ideality factor and barrier height, but was considered to be out of the scope of this work. IV measurements were done by performing a bias voltage sweep of a diode while measuring the electrical current. A Keithley 6487 picoammeter/Voltage source was used to supply direct current (DC) to the Schottky contact. Current passing through the sample (from the front- to the back-contact) was measured and saved for post processing, where the current meter is able to measure currents down to the pA range.

When presenting IV measurements, current and voltage are typically plotted in a semi-logarithmic plot. The rectifying properties of diodes are found by comparing the absolute difference of measured current at equal voltage of opposite polarity. Low to no change in absolute current between the two polarities show ohmic properties.

Over time diodes can degrade, e.g., by oxidation or interdiffusion between the two sides of the junctions. External stimuli, e.g., illumination or irradiation, can also alter the characteristics of a diode. Since CV,DLTS, and SSPC rely on rectifying contacts, IV measurements were done between every processing step to ensure that the contacts were rectifying, and to investigate if, e.g., illumination/irradiation degraded the contact.

Although no quantitative analysis of such data was performed, knowing its origin is useful for qualitative discussions. From the theory section, the current voltage relationship in an ideal Schottky diode with $n = 1$ is described by

$$I(V) = I_0 \left(e^{\frac{qV}{nkT}} - 1\right) = A^* A T^2 e^{-\frac{\phi_B^{IV}}{kT}} \left(e^{\frac{qV}{nkT}} - 1\right) \tag{3.1}$$

Where $\Phi_B^{IV}$ is the barrier height measured with IV. $I_0$ has a proportional relationship with the barrier height of the junction

$$I_0 \propto e^{\frac{-q\Phi_B}{kT}} \tag{3.2}$$

The ideality factor $n$ can be extracted from the IV-curve by finding the slope $s$ of the linear region in the low forward bias region. When $V > 3kT/q$ equation 3.1 can be simplified to

$$\ln I(V) = \ln I_0 + \frac{qV}{nkT} \tag{3.3}$$

Taking the logarithm of and rearranging the expression gives

$$n = \frac{q}{skT} = \frac{q}{kT}\left(\frac{dlnI}{dV}\right)^{-1} \tag{3.4}$$

This can be used to find the barrier height of the junction. Extrapolating the linear region of the curve to where it intercepts the y-axis gives the value of $I_0$. From equation 3.1 the exponential term holding $V$ is removed due to $V = 0$, so by taking the logarithm and rearranging the equation with respect to the barrier height it can be expressed as

$$\Phi_B^{IV} = kT \ln \frac{A^* A T^2}{I_0} \tag{3.5}$$

### 3.1.2 Capacitance-Voltage

Capacitance-voltage measurements are essential for characterizing electrical properties in semiconductors. Assuming a rectifying junction, it enables a quick and simple way to extract values including; carrier concentration on the low doped side of the junction, built-in voltage $V_0$ and the barrier height. The simplicity of analyzing CV measurements becomes clear when plotting $1/C^2$ as a function of the applied reverse bias. Rearranging equation 2.60 gives

$$\frac{1}{C^2} = \frac{2(V_0 - V)}{q\varepsilon A^2 N_{a,d}} = \underbrace{-\frac{2}{q\varepsilon A^2 N_{a,d}}}_{a} V + \underbrace{\frac{2}{q\varepsilon A^2 N_{a,d}} V_0}_{b} \tag{3.6}$$

which should give a straight line for a near perfect rectifying junction with homogeneous doping concentration. By simplifying equation 3.6 to a line equation ($y = aV + b$), the carrier concentration can be calculated by the slope $a = -2/(q\varepsilon A^2 N_{a,d})$. The built-in voltage is then $V_0 = -b/a$, where $b$ is the y-axis intercept point.

Furthermore, by extracting $V_0$ from CV measurements, the barrier height can be calculated by:

$$\Phi_B^{CV} = V_0 + \frac{kT}{q} + \xi \tag{3.7}$$

where

$$\xi = \begin{cases} (E_C - E_F) & \text{for n-type} \\ (E_F - E_V) & \text{for p-type} \end{cases} \tag{3.8}$$

By combining Eq. 2.5 and 2.7 an expression for $\xi$ can be obtained. For a n-type material:

$$n = N_d = N_C e^{-\frac{(E_C - E_F)}{kT}} = N_C e^{-\frac{\xi}{kT}} \tag{3.9}$$

And by taking the logarithm and rearranging the expression:

$$\xi = -kT \ln \frac{N_d}{N_C} \tag{3.10}$$

### 3.1.3 Deep Level Transient Spectroscopy

Deep Level Transient Spectroscopy (DLTS) is a characterization technique for electrically active defects in semiconductors that were introduced by Lang in 1974[10]. DLTS utilizes the thermal transient-behavior of electrically active deep defects, as described in section 2.1.5.1 to deduce the energy position, apparent capture cross section, and concentration of traps within the band gap.

The principle of DLTS is to characterize electrically active defects in the depletion region by introducing a external electrical stimuli. A rectifying contact is set to a constant reverse bias, before introducing a short pulse where the bias is either removed or changed to another value, before restoring the constant reverse bias. The short filling pulse is usually in the order of milliseconds, and during that time the traps within the depletion region that are below the Fermi level are filled. The subsequent reverse bias causes emission of electrons and holes from the filled traps which is measured by the capacitance change of the system. This is repeated several times for different temperatures in a temperature sweep to generate a DLTS spectrum. Fig. 10 illustrates the capacitance response in the material caused by the electrical pulses.

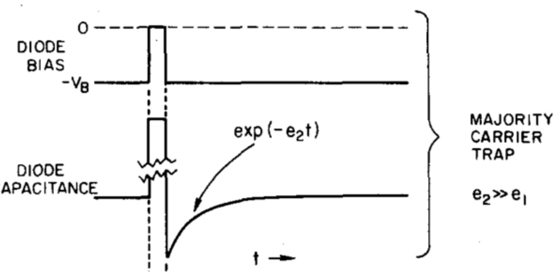

Figure 10: The capacitance transient response of a diode from an external electrical pulse. From Blood & Orton [4]

The DLTS spectra is based on the transient response of the material and is generated from the capacitance change of the transient. By considering two fixed points in time ($t_1$ and $t_2$) after the filling pulse and calculating the capacitance change $C(t_1) - C(t_2)$ in the interval, a signal can be obtained when the emission from trap is within the set time interval. This is shown in Fig. 11, where time between $t_1$ and $t_2$ is called the time window. The DLTS spectra is a function of temperature, and by assuming an electron trap, it is defined as:

$$S_i(T) = \underbrace{\frac{C_{rb}N_t}{2N_d}}_{\Delta C} \underbrace{\frac{1}{n_i}\sum_{t=t_d}^{t_d+t_i} e^{e_n t}\omega(t)}_{F_i} \tag{3.11}$$

where $i$ is the index of the time window, $C_{rb}$ the reverse bias capacitance, $N_t$ the trap density, $n_i$ the number of measurements acquired in the rate window, $t_d$ the data acquisition delay after the filling pulse, $t_i$ the duration of a rate window, $\omega(t)$ the weighting function [**?** ] applied on the transient to generate the DLTS spectra and $F_i$ is a parameter related to the weighting function and the time window. From the DLTS spectrum illustrated in Fig. 11, it is apparent that the peak position can be found by solving the derivative of $S_i$ with respect to $T$ equal to zero. By changing some variables this yields the expression:

$$\frac{dS_i}{dT} = \left(\frac{dS_i}{d(e_n t_i)}\right)\left(\frac{d(e_n t_i)}{dT}\right) = 0 \tag{3.12}$$

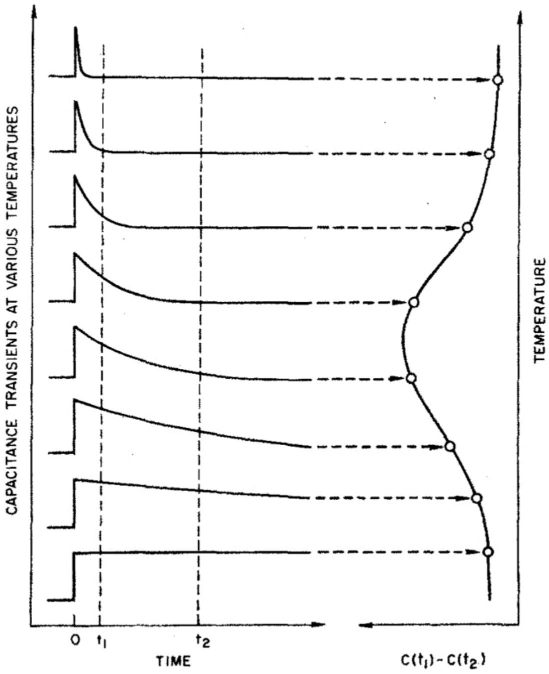

Figure 11: Illustration of the generation of a DLTS signal from capacitance transients in the time window $t_1$ to $t_2$. From Blood & Orton [4]

By investigation the expression, it is clear that $\left(\frac{d(e_n t_i)}{dT}\right)$ approaches zero only when $T \to 0$ or $T \to \infty$. Thus, by solving $\frac{dS_i}{dT} = \left(\frac{dS_i}{d(e_n t_i)}\right) = 0$, numerical values for $e_n$ and $F_i$ can be deduced for each time window. From Eq. 3.11, $N_t$ is proportional to the height of the peaks in the DLTS spectrum. Moreover, the emission rates obtained from peaks at temperature $T$ can be plotted in a Arrhenius plot as Eq. 2.31. Where $\Delta H$ is obtained from the slope of the Arrhenius plot and $\sigma_{na}$ by extrapolating the line to $T \to \infty$.

**The DLTS configuration of online-setup** The DLTS measurements conducted in this study was done on the developed online-setup. A schematic overview of the components comprised of the system is presented in Fig. 12

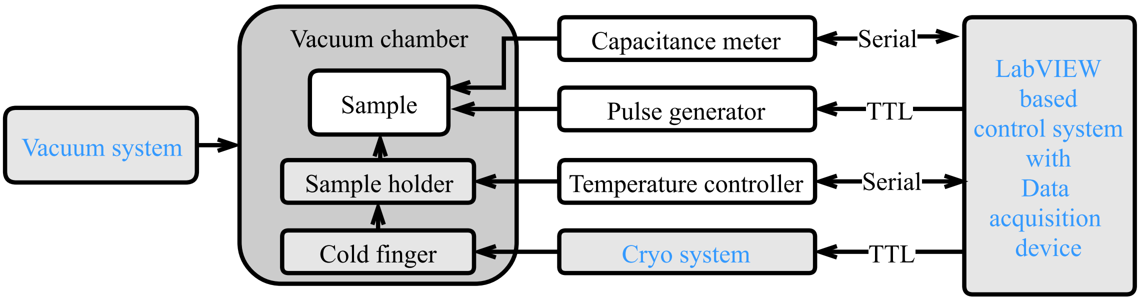

Figure 12: Schematic overview of the components used in a DLTS system.

Analysis and post-processing of the generated DLTS spectra was done with Python-scripts developed by Christian Zimmermann. Suggestion for further development of system is to include post processing scripts in the DLTS software.

### 3.1.4 Steady State Photocapacitance

Steady State Photocapacitance (SSPC) is a method for measuring deep levels in semiconductors with the use of optical excitation. SSPC measurements investigates the steady state photo-induced capacitance as a function of photon energy. By applying a constant reverse bias on a rectifying contact and subsequently illuminating the sample with photons of incrementally increasing energy, a SSPC spectrum is obtained. In section 2.1.5.2 the steady state occupancy of traps under illumination was given by Eq. 2.42 with the assumption that the thermal emission rates was suppressed by reducing the sample temperature. An energy band diagram of a rectifying contact under constant reverse bias is shown in Fig. 13, with the capture and optical emission processes induced by photon illumination.

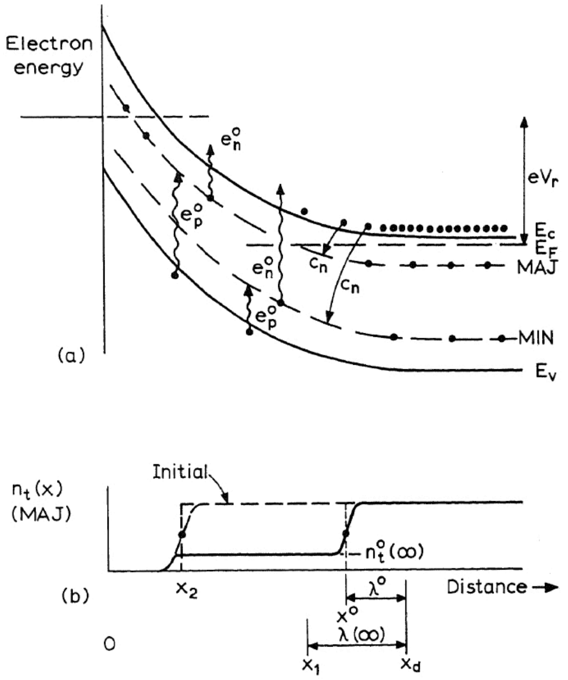

Figure 13: Energy band diagram of: a) a reverse biased Schottky contact of a n-type semiconductor showing the emission and capture processes. b) show the majority carrier (MAJ) trap occupancy at the beginning (dashed line) and end (solid line) of optical excitation. The electrons is emitted up to the end of the transition region $\lambda^o$, at a depth of $x_d - \lambda^o$, where $x_d$ is the depletion depth. From Blood & Orton [4]

The features generated in a SSPC spectrum is approximately located at the ionization threshold $E_i$ of the specific trap.In the case of majority carrier traps in a n-type material and from the assumption that $e_n^{th} \ll e_n^o$, emission from the initially filled traps is assumed to not occur until $E_{ph} > E_i$. The photo induced excitation of traps at $E_{ph}$ causes a capacitance change in the depletion region which generates a signal in the SSPC spectrum. As long as $E_{ph} < 1/2E_g$, only majority carrier emission is possible.The SSPC spectrum is expected to have a step-like shape as illustrated in Fig. 14, where each positive step is a result of electron emission and negative step, the complementary hole response.

In order to relate the measured capacitance signal to material properties, the capacitance change, just as $E_{ph}$ crosses the ionization threshold $E_i$ is given by:

$$\frac{\Delta C}{C} = \frac{1}{2}\left(\frac{(x^o)^2 - (x_2)^2}{x_d^2}\right)\frac{N_t}{N_d} \tag{3.13}$$

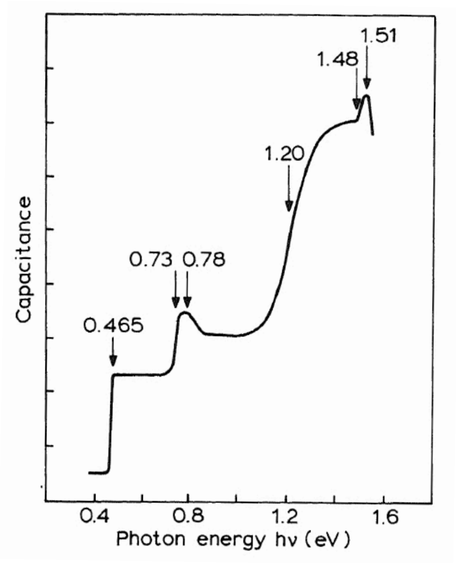

Figure 14: SSPC spectrum where the photocapacitance of a GaAs sample is plotted as function of photon energy indcident on the sample. From Blood & Orton [4]

This expression however, is only valid when the system is at a steady state and $E_{ph} < 1/2E_g$, since majority carrier emission is dominant. When $E_{ph}$ exceeds half the band gap, the minority carrier emission has to be accounted for, so for a n-type material the expression becomes:

$$\frac{\Delta C}{C} = \frac{1}{2}\left(\frac{(x^o)^2 - (x_2)^2}{x_d^2}\right)\left(\frac{e_n^o}{e_n^o + e_p^o}\right)\frac{N_t}{N_d} \tag{3.14}$$

The effect of the minority carrier emission taking place can be observed from Fig. 14 where a peak appear at 0.73 eV due to electron emission, followed by a drop at 0.78 eV due to a complimentary hole response. The signal then stabilized and regaining a steady state around 0.9 eV.

The specifics of how the SSPC measurements were conducted in this study will be presented and described in the result section.

### 3.1.5 Deep Level Optical Spectroscopy

Deep level optical spectroscopy (DLOS) is the optical counterpart to DLTS as already discussed. The purpose of this section is just to mention the existence of the DLOS technique, since a future goal is to implement DLOS capabilities in to the online-setup developed in this thesis. The only hardware difference between a SSPC and DLOS setup is that DLOS require a high seed shutter for timing light pulses. A similar high speed data acquisition device (DAQ, as used in DLTS) is also required to acquire the electrical signals from t he sample. Fig. 15 shows a schematic overview of various DLTS and DLOS techniques that all should be possible to run in the developed online-setup with custom made software in, e.g., LabVIEW.

## 3.2 Hardware components

Commercially available hardware was used for, e.g., measuring capacitance and current, applying voltage and controlling the temperature. A list of the hardware components used is listed in Tab. 3

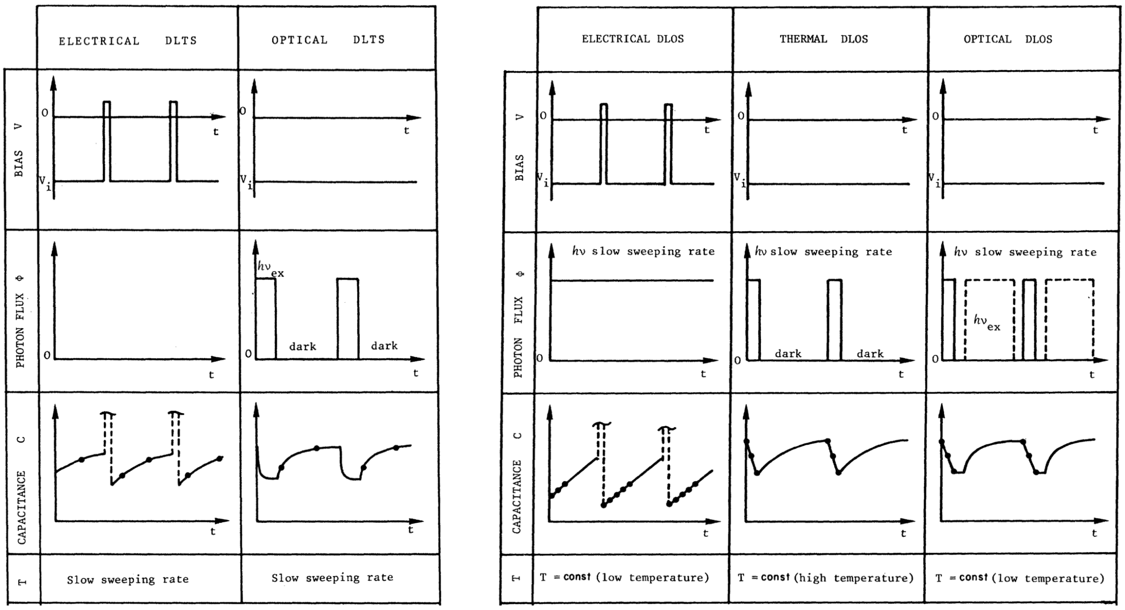

(a) (b)

Figure 15: Schematics showing the principle of operation of 2 DLTS and 3 DLOS techniques for characterizing electrically active defects. (a) Regular thermal DLTS and optical DLTS acquire transient data wile sample is in dark after a electrical or optical pulse, respectively. (b) Three categories of DLOS that all acquire data while sample is under illumination, but with different combinations of electrical and optical pulses, as well as temperature. From [11]

| Hardware name | Description | Used in |
|---|---|---|
| Boonton 7200 | Capacitance meter | CV, DLTS, SSPC |
| Agilent 81110A | Pulse generator | DLTS |
| LakeShore 332 | Temperature controller | DLTS, SSPC, IV, CV |
| Keithley 6487 | Picometer/Voltage source | IV |
| Andor Shamrock 500i | Spectrograph | SSPC |
| Energetiq eq-77 | Broadband Laser-driven light source | SSPC |

Table 3: Component list

### 3.3 LabVIEW

Laboratory Virtual Instrument Engineering Workbench (LabVIEW)[12] is a graphical programming language developed by National Instruments (NI). LabVIEW is commonly used in system for system control and data acquisition purposes due to its ease of use when integrating hardware with software with the extensive driver support from NI. In this work LabVIEW were used as the main software development platform to create custom programs for various characterization techniques. By connecting hardware and developing logic in software techniques like: IV, CV, DLTS and SSPC was developed.

Signal analysis of almost every part of an electrical system can be done by utilizing a general purpose data acquisition device (DAQ)[13]. In this work a NI PCIe-6321 DAQ-card with a BNC-2110 connector block was used to acquire and generate analog and digital signals. Acquired analog signals can be digitized in for further post-processing and analysis by using the DAQmx-tools in LabVIEW. An example of this is the Boonton 7200 capacitance meter, that outputs a analog signal that is proportional to the measured capacitance value of the Boonton. This enables high speed data acquisition of, e.g., capacitance transients that is important for DLTS. Being able to probe and acquire electrical signals in a system is crucial when developing a electrical system.

LabVIEW code is similar to circuit diagrams in electronics, where circuit element are connected together with wires. A program is called a virtual instruments (VI), which comprises a "front panel" with virtual buttons, knobs and indicators and a "block diagram" where the program logic is coded. A benefit of using a high level coding language LabVIEW, compared to other low level text-based programming languages (e.g., C and C++) is that the front-end (user interface) is automatically generated based on the back-end code. Reducing the time and knowledge required to develop both the user interface and the underlying program logic. This is the main strength of LabVIEW, that enables quickly prototyping when developing new system designs. A drawback of LabVIEW is the graphical nature of the code, which is easy to make unorganized and hard to scale if done improperly. In LabVIEW, program architecture is important to develop structured code, maintain scalability and modularity. In this work, programs was developed with and emphasis on being user friendly and easy to maintain, so a event driven architecture with state machines[14] was used.

The developed programs will be presented in the results section.

## 3.4 Sample preparation

### 3.4.1 Physical vapour deposition

This section is based on the works of Mahan [15] and Mattox [16].

Physical vapour deposition (PVD) is a collective term for a range of vacuum techniques used for thin film deposition, where two of the most common methods are sputtering and evaporation. In this thesis PVD by evaporation has been utilized. In this case, an electron beam was used to transform a target material into a gaseous phase, where it is subsequently precipitate at surfaces within the line of sight. Layer thickness is based on the deposition rate measured with a quartz crystal, and can be as thin as a few nanometers.

PVD is often used to deposit electrical contacts on semiconductor substrates. For example, circular contacts are readily made by e-beam deposition through a shadow mask. In this respect, the exact diode area is an important parameter since contacts are used as a tool to characterize a substrate material. In this work, the diode area is important due to the contact area dependency in CV measurements, as discussed in the theory section.

In the present study, a Ångstrøm EvoVac PVD system was used.

### 3.4.2 Wire Bonding

Wire bonding is a technique widely used in the electronics industry to create interconnections between electrical components.

The concept of wire bonding is to create surface-bonded connections with thin metal wires between two points in order to make a electrical connection, but it is at the cheer scale at which this connections is done that makes it so powerful. Wires can be only a few tenths of microns in diameter.

Wire bonding uses a probe with an internally threaded wire, which feeds out wire when moving from a bond site to the desired endpoint When starting a new wire bond, the probe touches down on the contacting surface and uses ultrasonic vibrations to bond the internally threaded wire to the surface. With the first contact point bonded, the probe head feeds out wire while moving to the endpoint where the endpoint gets bonded.

Wire bonding can be used on a large range of material surfaces and by tuning bond height and lengths very intricate interconnections can be achieved.

### 3.4.3 Ion Implantation

This section is based on the works of Campbell [17] and Streetman [2].

As the name suggests, Ion implantation is a technique designed to implant ionized particles into a target. By accelerating ions in a electric field, controlling the implantation dose and energy, a implantation profile can be achieved in the target material. Fig. 16 show a schematic overview of an ion implantation system that comprises an ion source, mass separator, accelerator, scanning unit and a sample holder with a beam current integrator. The principle of operation is that particles are ionized from a solid or from a gaseous source and accelerated in to the mass separator, that bends the path of the particles based on its mass given by:

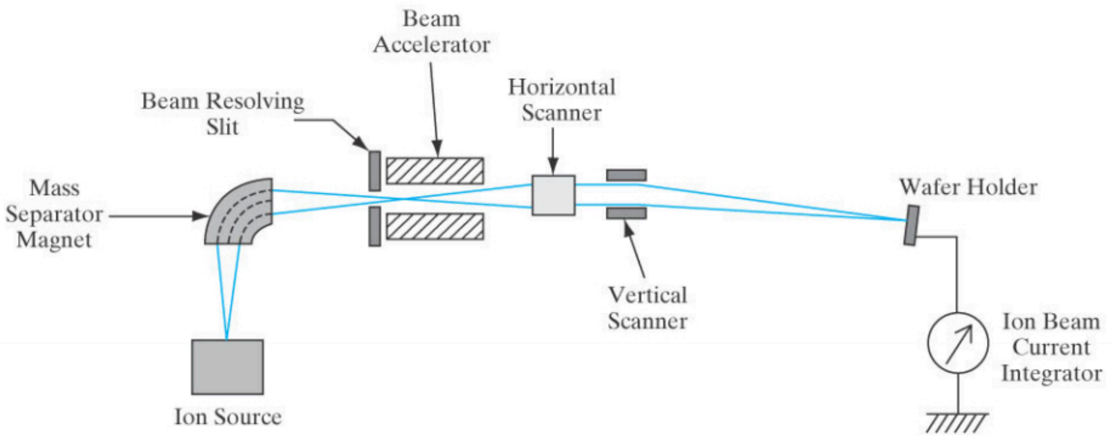

Figure 16: Schematic overview of an ion implantation system that comprises many other parts as labeled in the figure. From Streetman [2]

$$\frac{mv^2}{r} = qvB \tag{3.15}$$

where $m$ is the ion mass, $v$ the velocity of the ion, $q$ the charge and $B$ the applied magnetic field in the mass separator. Based on the velocity or applied magnetic field, ions are selected and further accelerated through a horizontal and vertical scanning unit to align and focus the beam on to a sample. The beam current is then measured in order to determine the implantation dose.

The ion implanter used in this work is a 1 MeV tandem accelerator from NGC The advantage of the ion implantation system situated at MiNaLab is that it is able to do both low energy irradiations and high energy implantations in the energy range of keV to MeV. Thus both very deep and shallow implantation profiles can be achieved. Implantation profiles are calculated by the use of the SRIM-software [18] which is based on Monte Carlo simulations to generate dose vs depth profiles of implanted ions.

In this work the proton irradiation was done at 600 keV with a dose of $1 \times 10^{13}\,\mathrm{cm}^{-3}$ in $\beta$-$Ga_2O_3$ . SRIM calculations estimate a peak depth of approximately 4.3 µm in to the sample, thus only the tail region of the irradiation profile is within probing range of the characterization techniques used.

# 4 Results and Discussion

The main objective of the work presented in this thesis is to develop an electrical characterization system connected to a 1 MeV ion accelerator capable of online characterization of semiconductor systems including optical junction spectroscopy like SSPC and DLOS. In this chapter the development and experimental verification of the system will be described and discussed. First, the development of the experimental setup related to the integration of optical excitation will be described, including choice and testing of the components. Second, the application of the system on oxide semiconductors will be demonstrated, with particular emphasis on optical junction spectroscopy on $Ga_2O_3$ .

The setup is connected to one of the beamlines of an MeV ion accelerator from NEC. The electrical characterization of , e.g., electrically active defects can be carried out during or after ion implantation without breaking vacuum or changing temperature, hence the term “online”. Importantly, the implantations/irradiations can be carried out at a selected temperature, e.g. at low temperatures where intrinsic or impurity-related defect migration is negligible. This potentially enables studies of properties and the formation of fundamental defects, like interstitials or vacancies To the best of our knowledge, there are currently no other system which combine optical and electrical online characterization at a MeV ion accelerator, and only a few systems connected to to electron irradiation facilities exists worldwide.

The starting point for the work was an existing vacuum chamber with a vacuum and cryogenic system for low temperature electrical measurements, and hardware like capacitance meter, electrometer, temperature controller, etc. However, the vacuum chamber needed to be modified in order to include optical excitation, and later on to be compatible with optical spectroscopy measurements. In particular, the development of the optical excitation capabilities and related components has been a major focus in the present work, and will be given special attention in this section. Custom software for CV, IV and DLTS was also available from previous system, but developed in older LabVIEW versions that were becoming outdated. Thus, the LabVIEW control programs for all the major measurement techniques where built from scratch, including the development of an instrument library.

The work presented in this section will be split into two parts. The first part covers the development of the existing experimental setup describing the integration of optical excitation, including testing of the additional components. The second part covers the utilization of the system that has been built-up to study $Ga_2O_3$ and ZnO

## 4.1 Development of Online-Setup

The online setup that is developed in this thesis needs to perform both "basic" measurements like CV and IV, as well as more advanced techniques for deep level defect studies. Since a new platform based on LabVIEW was developed, the work included every aspect of development like;

- Planning layout
- Designing custom components
- Building software
- Testing operation conditions

The basis of the work was re-purposing the former online-chamber in order to develop the proposed experimental techniques. A schematic overview and the design of the online-setup is shown in Fig. 17, 18. The different parts will be described in the following subsections, and an overview is found in Table 4 below and includes the main development.

A lot of customized equipment was required for the setup. However, often components are designed to either do one specific task very well or compromises performance for added flexibility. Even simple issues like metric and imperial unit miss-match between components introduce challenges that had to be solved. Standards within electrical signaling protocols were another example that had to be taken in to account. Most of the mechanical compatibility issues were solved by designing custom components with a Computer-Aided Design and Manufacturing (CAD/CAM) program called Fusion360 by Autodesk[19]. In collaboration with the Instrument laboratory (Ilab) at the physics department at UiO, the parts required were manufactured from design sketches (See Appendix A). Signal communication was handled with LabVIEW in order to incorporate a host of different instruments into one experimental setup.

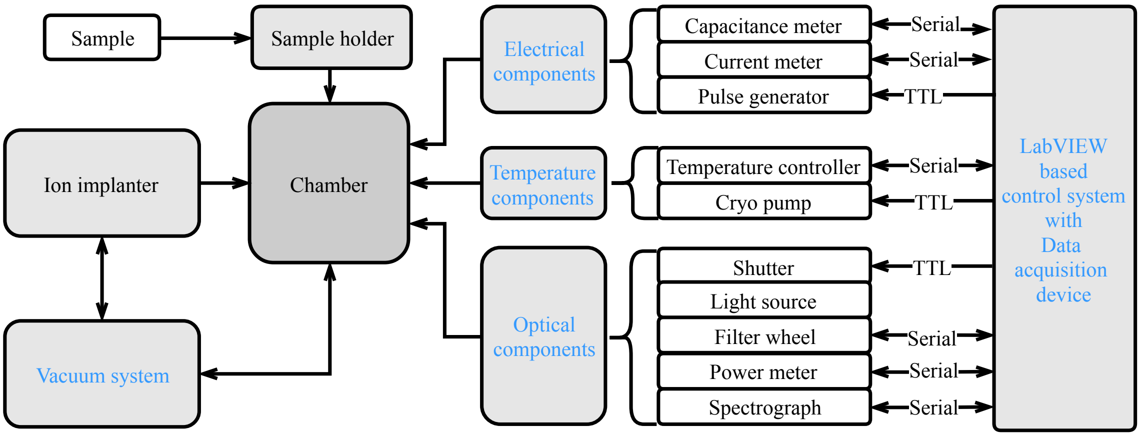

Figure 17: Schematic overview of the systems and units that is used in the online-setup

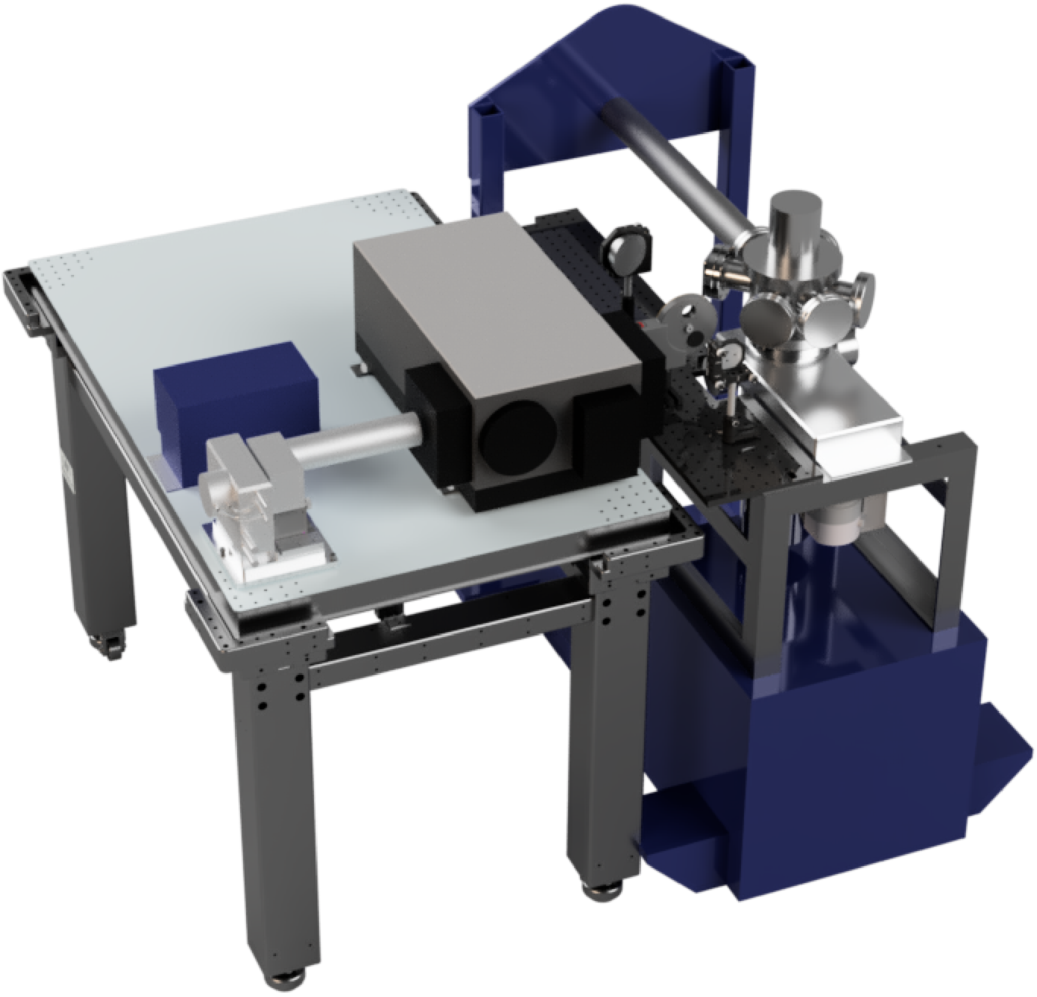

Figure 18: Illustration of the online-setup and the optical components. CAD files of components from Newport and Thorlabs was acquired from company website [20, 21]

| **Part** | **Purpose/content** | **Main development** |
|---|---|---|
| Ion implanter beam line | Irradiation/implantation of the smples | New extended beamline with beam scanner (mainly organized by MiNaLab engineers) |
| Chamber | Host sample and connect to beamline | Re-organize output ports and feedthroughs, including optical access and electrical feedthroughs |
| Sample stage | For sample mount | Improve electrical connectivity and design of an implantation compatible heat shield |
| Measurement hardware | Units for measurements of current and capacitance, and applying bias and voltage pulses | Combining the appropriate hardware for the various experimental techniques that where developed |
| Cryogenic system with temperature controller | Achieve cryogenic temperatures in sample chamber | Implement temperature control in experimental techniques |
| Optical excitation system | Enable optical junction spectroscopy | Develop and investigate the spectral resolution and capabilities for use in experimental techniques |
| LabVIEW control system | Control of all units | New platform for IV,CV and DLTS and development of SSPC and DLOS software |

Table 4: Overview the work done on parts of the online-setup

### 4.1.1 Chamber

At the beginning of the master project, a vacuum chamber was already connected to the beam line of the MeV ion accelerator, as shown in Fig 19. The chamber was equipped with a turbo pump (Pfeiffer HiCube ECO and HiPace 80) capable of achieving high vacuum close to $10^{-8}$ Torr measured with a vacuum gauge (Edwards, Wide Range Gauge[22]). On the bottom part of the chamber a cold-finger is mounted which is connected to a closed-cycle helium cryopump. The vacuum chamber comprises 8 side-output ports and one lid that all use Viton rubber O-ring seals. Although the setup was capable of conducting electrical measurements like IV, CV and DLTS, it was not designed for optical characterization techniques. The first necessary modification was to enable light from a light source outside the vacuum chamber to be incident on a sample inside without significant intensity loss while maintaining high vacuum. This was achieved by designing a general purpose window holder for hold 2” optical windows of up to 8 mm in thickness. The design and technical drawings was developed in Fusion 360, as shown in Appendix A. In order to create a vacuum tight seal, rubber o-rings of Viton was used. Grooves for the s-rings in the window holder body was designed according to specifications by Otto Olsen AS [23]. An advantage of using o-rings is that it enables windows to be changed if necessary, rather than permanently gluing the window in place. A disadvantage is that rubber o-rings is not able to hold ultra high vacuum ($\sim 10^{-9}$ Torr). The window holder was equipped with a 2 mm thick 2” sapphire window to enable a broad range of light to pass trough. A transmission study on sapphire is presented later in this section.

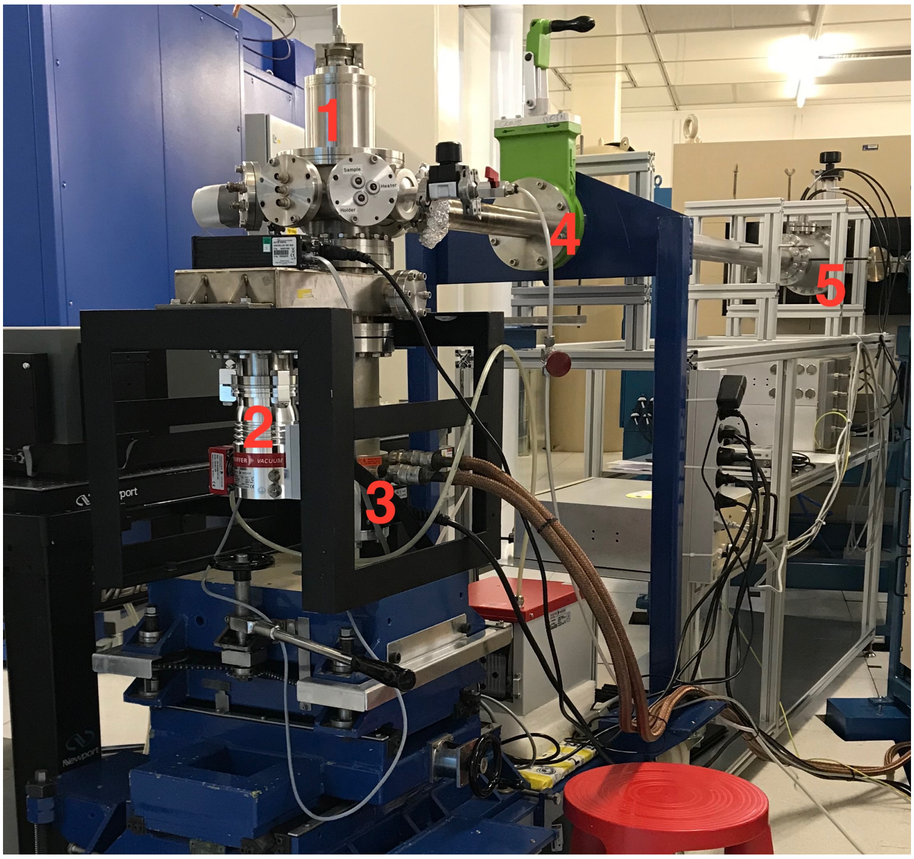

Figure 19: Image of the online-setup after the scanning unit(5) was installed (before the optical excitation system was implemented.) where: 1) is the vacuum chamber 2) HiPace 80 turbo pump 3) Closed-cycle helium cryostat with cold finger 4) vacuum valve to the beam line 5) vertical and horizontal scanning unit to control the ion beam.

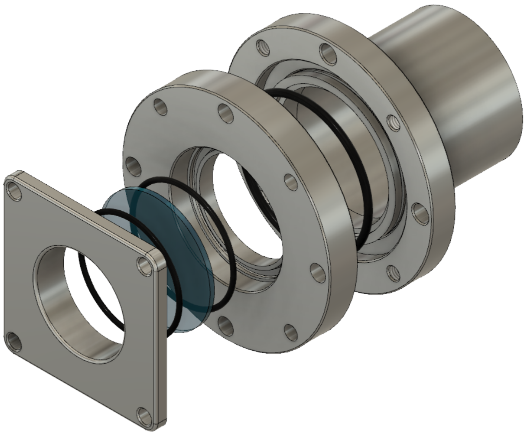

Figure 20: Illustration of the general purpose 2” window holder, designed for the output-ports of the vacuum chamber in the online-setup. O-rings of Viton rubber is used as vacuum seals.

Another modification done on the vacuum chamber was to extend the number electrical feedthroughs in the vaccum chamber. Initially the setup was equipped with only four electrical contact-points for signaling purposes. One of the four contact points is always connected a Faraday cup inside the chamber used for measuring beam current. Most samples us one common back contact and separate front contact, which means that only two diodes could be electrically accessed after the chamber was pumped down to vacuum. The principle advantage of online measurements is that a sample can be measured before and after irradiation without breaking vacuum. With the previous setup, online measurements was only possible for two diodes or samples at one time. Due to the time and cost linked to irradiation studies, increasing the amount of contact points can drastically increases productivity as well as reducing cost. A new output-port was designed with 7 BNC feed thorough to enable access to six contact points on a sample with the Farady cup connected.

### 4.1.2 Sample

One of the key requirements for performing SSPC and DLOS is the ability to deliver light to the depletion layer of a rectifying junction, e.g., a Schottky contact. As described in section 3.1.4, it is beneficial to illuminate from the front side. Therefore, a new contact design and sample mount had to be developed in the present system for front side illumination. In case of a Schottky contact, sufficiently transparent contacts are required. The contact configuration was developed to ensure sufficient transmittance, good electrical properties, mechanical stability for contacting and easy manufacturing. To maximize the amount of light entering the depletion region, shadowing effects from the front contact and contacting wires had to be taken in to consideration. In this section the development of such contacts will be presented using $Ga_2O_3$ as an example. The $Ga_2O_3$ samples used have a surface orientation of (010) and a nominal charge carrier concentration of $1.5 \times 10^{17}\,\mathrm{cm}^{-3}$. Rectifying junctions on $Ga_2O_3$ can be fabricated by using a Ni front contact to form a Schottky barrier. Ti/Al is used as an ohmic back contact, where a Ni thicknesses of 150 nm where used[24].

#### 4.1.2.1 Contact development

In order to utilize Ni/$Ga_2O_3$ Schottky contacts, the geometry of the contact was changed to achieve sufficient transparency. All materials are transparent when they are sufficiently thin, described by the Beer-Lambert law (Eq. 2.9). Reducing the Ni contact thickness to below ~20 nm, light transmission was achieved through the contact. Figure 21a illustrates the cross section of the final sample configuration which consists of a Schottky front contact (Ni) and an ohmic back contact (Ti/Al). A top view of the contact pattern is shown in figure 21b.

To investigate the transmitted light through the Ni contact, transmission measurements were carried out on three model systems: Ni/borosilicate glass, Ni/Aluminum oxide ($Al_2O_3$) and Ni/$Ga_2O_3$(010). Borosilicate glass was mainly chosen due to it being a relatively inexpensive material which has a relatively high transmittance in the visible spectrum, unfortunately it is highly absorbing in the UV. Crystalline $Al_2O_3$ on the other hand has the benefit of being transparent in the UV, but is more expensive than borosilicate glass. $Al_2O_3$ is also used as the window material for the vacuum chamber (see Sec. 4.1.1). $Ga_2O_3$ was chosen due to it being the material to be studied by SSPC measurements, so investigating how Ni influences the transmittance was of great interest. Comparing the results from the three model systems can unveil if borosilicate glass can be used to gauge what metal thickness is sufficient to achieve transparent contacts for other materials e.g. ZnO.

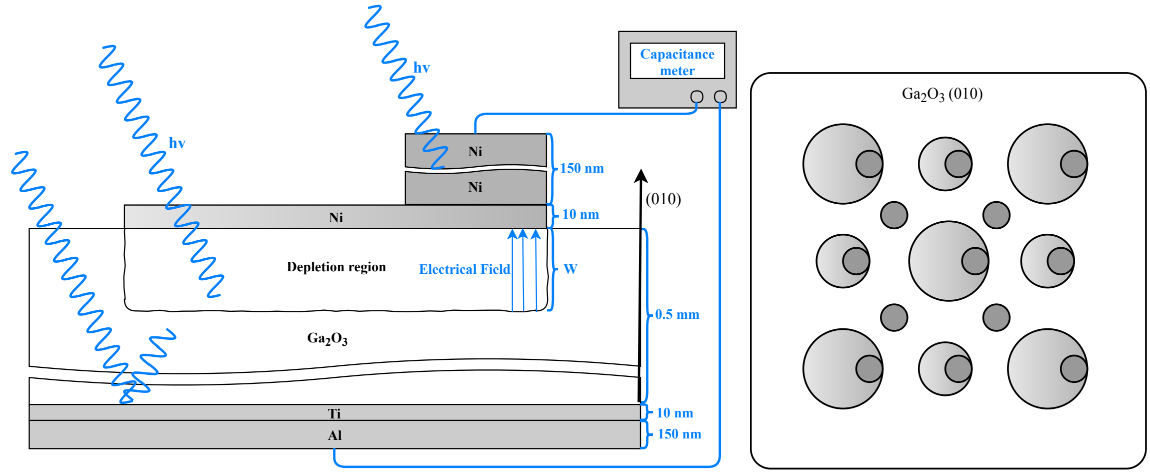

(a) Side view (b) Top View

Figure 21: Sample stack

Ni was deposited by e-beam PVD. The $Ga_2O_3$ samples had a polished front-side surface finish and grinded back side. For each model system: Ni thicknesses of 0 nm, 5 nm, 10 nm and 15 nm were tested. Figure 22 shows the results from transmittance measurements.

As shown in 22a, borosilicat glass absorbs strongly in the UV and hence, reduced transmission shoud be expected in this region. Generally, it can be seen that while qualitatively similar results are achieved for $Al_2O_3$ and $Ga_2O_3$ , the magnitude of transmittance depend strongly on the material. Figure 22a shows that around 90% of the incident light is transmitted by borosilicate glass without Ni contacts. When Ni is introduced the transmittance at 3 eV decreases to ~ 55% for 5 nm Ni, ~ 40% for 10 nm Ni and ~ 25% for 15 nm Ni. This confirms the theory that transparent contacts could be achieved with sufficiently thin nickel layers. It also shows that boronsilicate glass can be used as test substrate

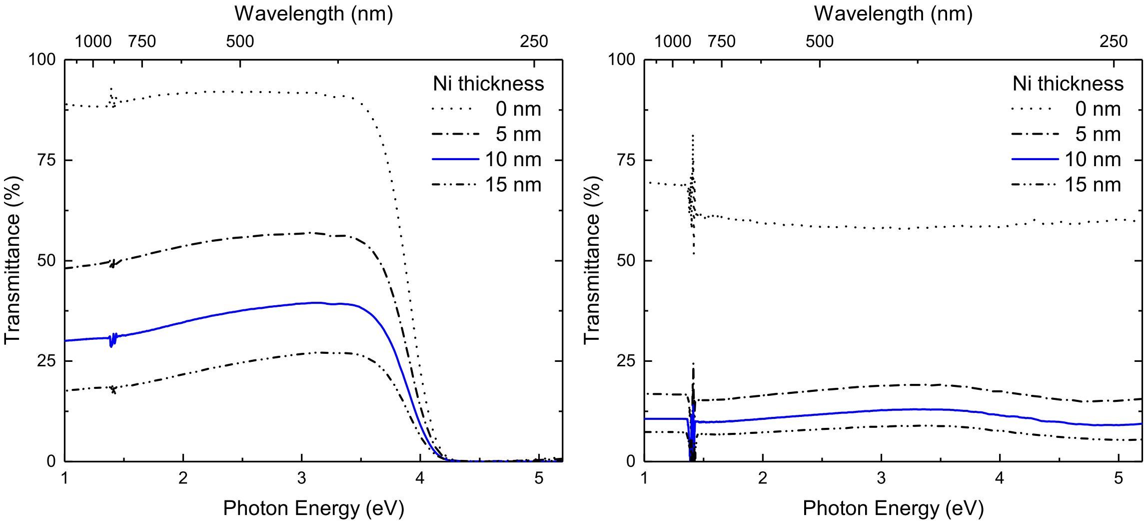

(a) Ni/Borosilicate glass

(b) Ni/Aluminum oxide

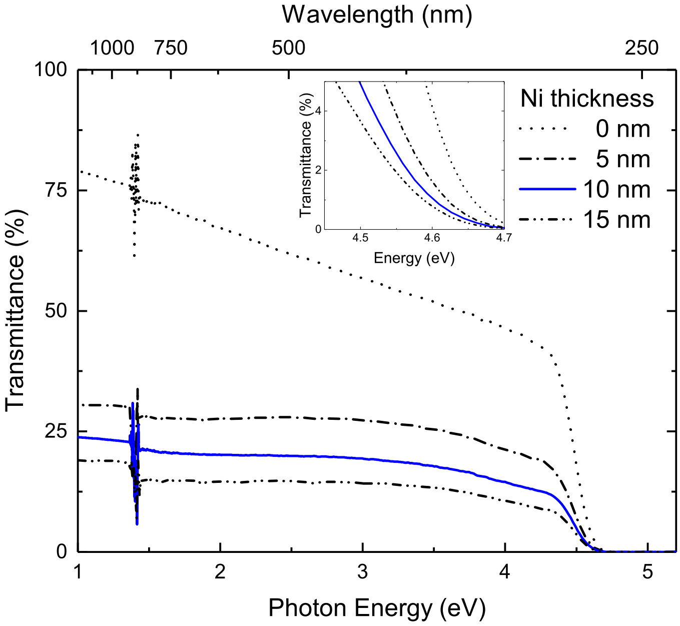

(c) Ni/Gallium oxide(010)

Figure 22: Transmittance measurements of Ni thin-films deposited by physical vapour deposition on: (a) borosilicate glass, (b) $Al_2O_3$ and (c $Ga_2O_3$ (010)

for future transmission studies of other contact material intended for semiconductors with $E_g <\sim$ 4eV. To investigate the transmittance trough the Ni contact in the UV outside the range of borosilicate glass, $Al_2O_3$ was used and results are shown in figure 22b. A factor that can cause a shift in the total transmittance of a sample is surface roughness. This was not measured for any of the samples since only the relative change in transmittance with respect to the added Ni thickness is of interest. The transmittance of $Al_2O_3$ without Ni is fairly constant in the whole spectrum. Introducing Ni reduces the transmittance similar to that of borosilicate glass but show no significant absorption in the UV as expected. This result show that Ni is suited for use as contact material in SSPC, since it has a constant and wide transmittance curve.

Lastly, figure 22c show results from $Ga_2O_3$ . Without Ni, the transmittance of $Ga_2O_3$ constantly decreases when increasing photon energy until reaching energies close to the band gap of $Ga_2O_3$ . The optical band gap of $Ga_2O_3$ extracted from transmission mea-

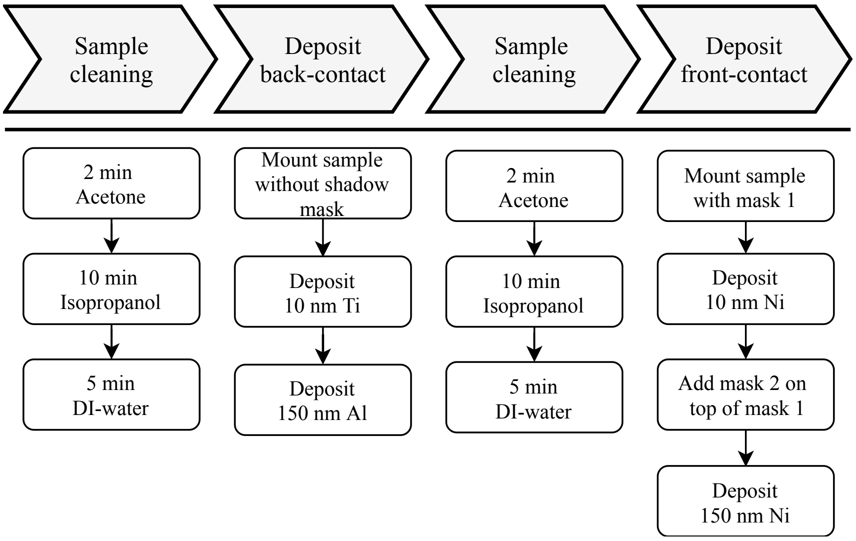

Figure 23: Illustration of work-flow for sample preparation. Cleaning done in ultrasonic bath and dried with $N_2$ gas between steps. Deposition done in a Angstroem EvoVac PVD

surements does not shift significantly with added Ni layer thickness, as can be seen from inset of Fig. 22c, where $E_g$ was found to be $\sim 4.68\,\mathrm{eV}$ for $Ga_2O_3$ without Ni. Depositing Ni on $Ga_2O_3$ reduces the transmittance, as expected from the measurements above. Nickel causes the transmittance curve to flatten compared to bare $Ga_2O_3$ . In conclusion, the transmission study show that Ni with thickness below ~20 nm is a suitable contact material for optical excitation.

A drawback of a very thin metal contact is low mechanical stability, such that the contact itself might break when contacting. To improve this, mechanically stable and semi-transparent contacts were fabricated by depositing two regions of different thickness, as shown in Fig. 21a. This illustrates that the transparent region of the contact was 10 nm thick, while another more mechanically sturdy region had a thickness of 150 nm.

For the back contact, a stack of 10 nm titanium (Ti) and 150 nm aluminum (Al) covering the entire backside of the sample was used. The highly reflective metallic surface of the back contact is also beneficial for illumination of the depletion region, since light that would otherwise be transmitted, could be reflected back into the depletion region.

Shadow masks were designed with the CAD/CAM software Fusion 360[19] as shown in Appendix A. The CAD-files were then used by the ILab at UiO to manufacture the masks out of Al on a Haas Minimill (vertical CNC-machine). The CAM programming were done by technicians at the ILab. The small size of the holes and masks themselves made manufacturing challenging, approaching the limits of what the CNC-machine can handle. Each mask is only 500 µm thick and consists of 145 holes spread out over a 15x15 mm. The circular contacts illustrated in Fig. 21 where made by a sequential deposition with two shadow masks (Appendix A). Figure 23 show the developed deposition procedure. The pattern of the first mask (mask 1) consist of holes with diameters of 300 µm,600 µm and 900 µm, while mask 2 only has 300 µm holes. To achieve the desired pattern illustrated, it was critical that mask 2 aligns perfectly on top of mask1. To ensure this alignment, the masks were designed with small notches that restricts mask 1 and 2 to shift when stacked. Figure 24 show how the front contact pattern is achieved by deposition Ni with mask 1, then stacking mask 2 on top before deposition a second layer of Ni.

The contact layout proposed could also be manufactured by utilizing photolithography. The drawback with photolithography is that it requires more process steps in order to achieve results similar to sequential deposition with metal shadow masks. Therefore it

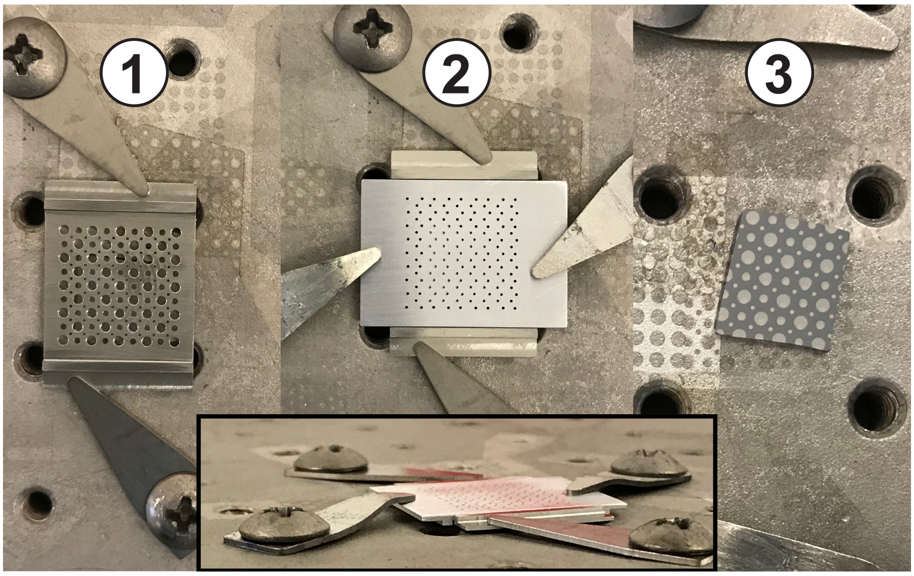

Figure 24: Correct diode-pattern is achieved by: (1) Secure mask 1 on top of sample with clamps before first deposition (10 nm). (2) Before 2nd deposition (150 nm), align mask 2 on top of mask 1 and secure with clamps. Important to not move mask 1! (3) Remove masks

is often more challenging to do lithography on small samples. Shadow masks of thin metal sheets, on the other hand, have the advantages of being easy to use, allow for batch deposition, no added processing steps are required, can be used on any material and the masks are reusable.

Since the developed contact configuration consists of two layers with different area, it was important to investigate the active area of the diodes. To verify the contact design, CV measurements where conducted to determine the effective area of the diodes. As discussed in the experimental section on CV, the carrier concentration can be deduced from the slope of the curve of a $1/C^2(V)$ -plot, where uniform doping is assumed. Equation 3.6 shows that the dielectric constant $\varepsilon$ and the area of the diode has to be known in order to calculate the carrier concentration. Moreover, the carrier concentration depends quadratic on the area, making the carrier concentration very sensitive to deviations in effective area. Since the carrier concentration in the $Ga_2O_3$ samples were known (see Sec. 4.1.2), the active area was estimated by calculating carrier concentration for different area values and compared to that reported by the manufacturer ($1.5 \times 10^{17}\,\mathrm{cm}^{-3}$). Also comparing carrier concentration values of different diode sizes on one single sample yield results on active diode area. In the calculation, a dielectric constant of 10[9] was used for $Ga_2O_3$ , and a donor concentration of $1.5 \times 10^{17}\,\mathrm{cm}^{-3}$. The CV measurements on $Ga_2O_3$ verified that the capacitance originated from the entire contact area, with a deviation of ~5 %. Figure 25 show deposited diodes seen under a microscope.

### 4.1.3 Sample mounting

In order to electrically connect the samples for use in the online-setup, the sample needs to be mounted on an isolating ceramic plate that can be mounted on the sample stage in the chamber. The ceramic plate has 6 gold contacting points that are isolated from each other and one large region where the sample is glued in place with conductive silver paste to the back contact, see Fig.26a. In order to establish electrical contact to the front contact, wire bonding was used. This has the benefit of reducing shadowing for both ion implantation and incident light needed for SSPC. It also provides a robust connection during online

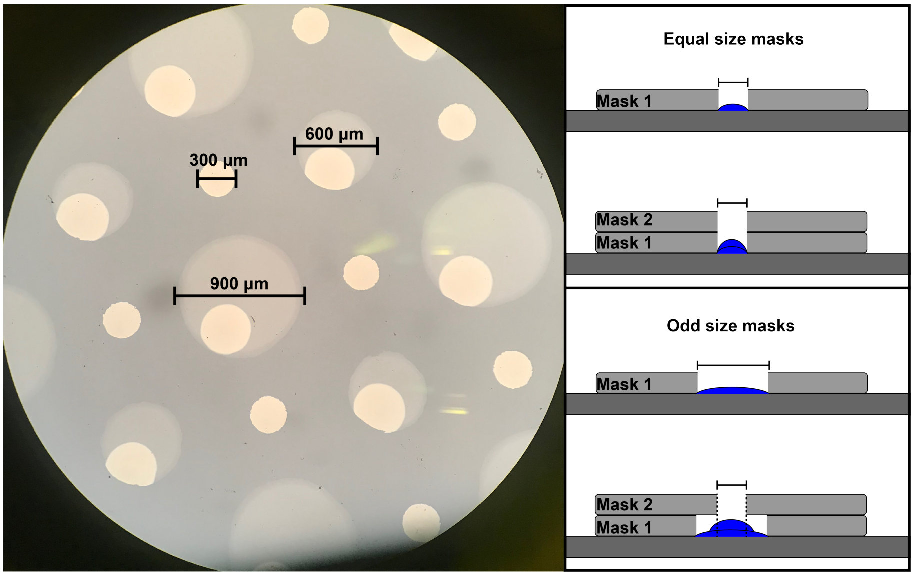

Figure 25: Picture of contact pattern under a microscope. In the left figure, some nonuniformities can be seen in some of the contacts caused by miss-alignment of the two shadow masks. The illustration on the right show that the thick 300 µm Ni region on top of the 600 µm and 900 µm Ni region can get slightly larger than 300 µm. This is due to shadowing effects from the PVD process, where the increased distance between the top mask and the sample can cause geometric changes to the mask pattern. The mask for single 300 µm contacts are in direct contact with the sample and can only cause a slight decrease in diode are.

measurements, reducing the influence of vibrations from the setup (mainly from the turbo pump and cryopump). However, stress in the metal contact can occur during wirebonding, leading to a reduced contact quality. In particular, the contact between the thick and thin region is fragile and may fracture/break during bonding. After deposition of all contacts, IV and CV was measured to check contact quality. Contacts were also checked after wire bonding, ensuring that contact performance is retained.

### 4.1.4 Optical excitation system

An important objective in this work was the integration of an optical excitation system of near monochromatic character with variable wavelength into the existing characterization setup. In order to achieve this objective the following is needed:

- White light source
- Monochromating system
- Light delivery system

In the following section, the challenges and work related to the optical components will be described. Figure 27 shows a schematic overview of all optical components part of the new online-setup.

As light source (labeled ① in Fig27), a EQ-77, broad-band Laser-Driven Light Source (LDLS) from Energetique[25] with a wide spectral radiance is used. The benefits of using a LDLS compared to, e.g., a halogen bulb is the flat spectral radiance (see Fig.28) and longer lifetime, since the LDLS does not use filament. The manufacturer states an operating range from 0.59 to 7.29 eV (170-2100 nm), which enables SSPC studies of wide band gap materials including $Ga_2O_3$ .

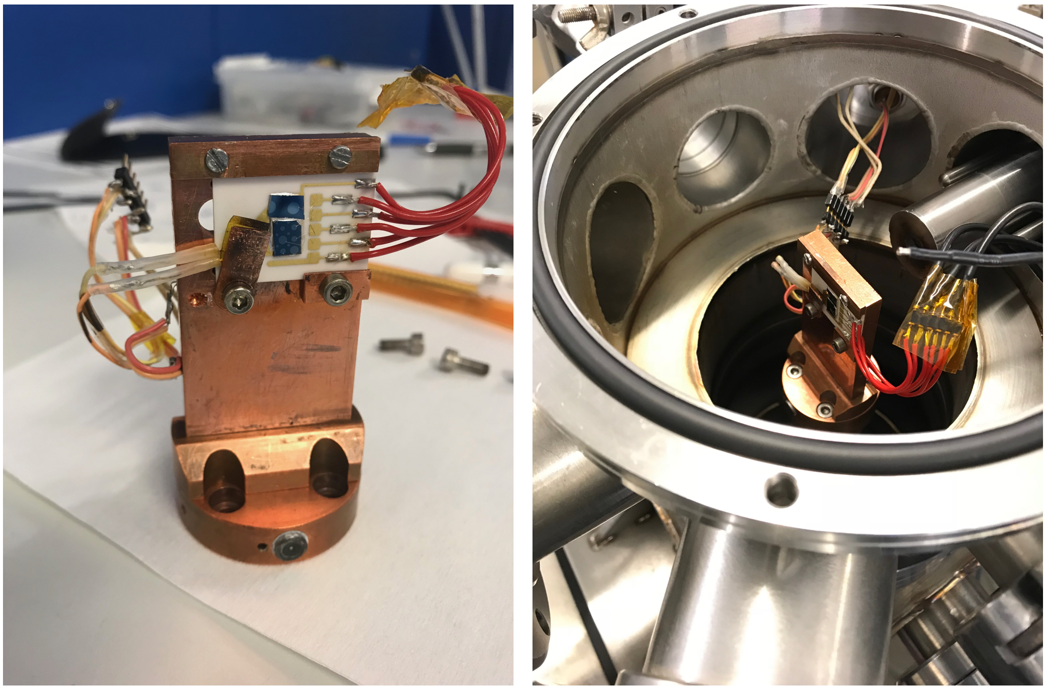

(a) Sample holder with two Si-test diodes on ceramic plate

(b) Sample holder mounted on cold-finger in chamber

Figure 26: Pictures of sample holder and placement in the online-setup

#### 4.1.4.1 Monochromator

In order to build an optical excitation system at variable wavelength, a monochromatic system is needed to split the light originating from the broad-band light source introduced in the previous chapter into its spectra components and select which component should enter the light delivery system, which will be described in the next section.

A grating monochromator can perform both tasks. The monochromator used in this theses is a Shamrock 500i purchased from ANDOR Technology. The Shamrock 500i comprises two input and two output ports. The monochromator can be controlled using LabVIEW software.

The broad-band light source was connected to one of the input ports (see Fig. 27). The light is focused into the plane of the entrance slit, whose width can be varied between 10 and 2500 µm. The light then bounces of two mirrors and is diffracted off the grating. The diffraction leads to different wavelengths of light being reflected off the grating with different angles. The angle between grating and incident light is varied in order to send the desired wavelength towards two further mirrors, that focus the corresponding light rays onto the output slits plane, where it leaves the monochromator.

Generally, it is important that the numerical aperture of the input determined by the parabolic mirror assembly of the light source and the numerical aperture of the monochromator match. The numerical aperture of the parabolic mirror assembly used is 0.094 [26], while the Shamrock spectrograph has a numerical aperture of 0.08. Ideally, the numerical aperture for the input should be lower or equal the spectrograph's numerical aperture. The current configuration leads to a slight over illumination of the grating within the spectrograph, which could result in stray light. This was tested at the development stage.

The spectral resolution of the monochromator is determined by its length (500 nm), the properties of the grating used as well as the width of the output slit (50 til 2500 µm). Here, a grating with 1200 l/mm was used, which is usually considered to be a high resolution configuration. This means that one has to compromise on output power. Both spectral

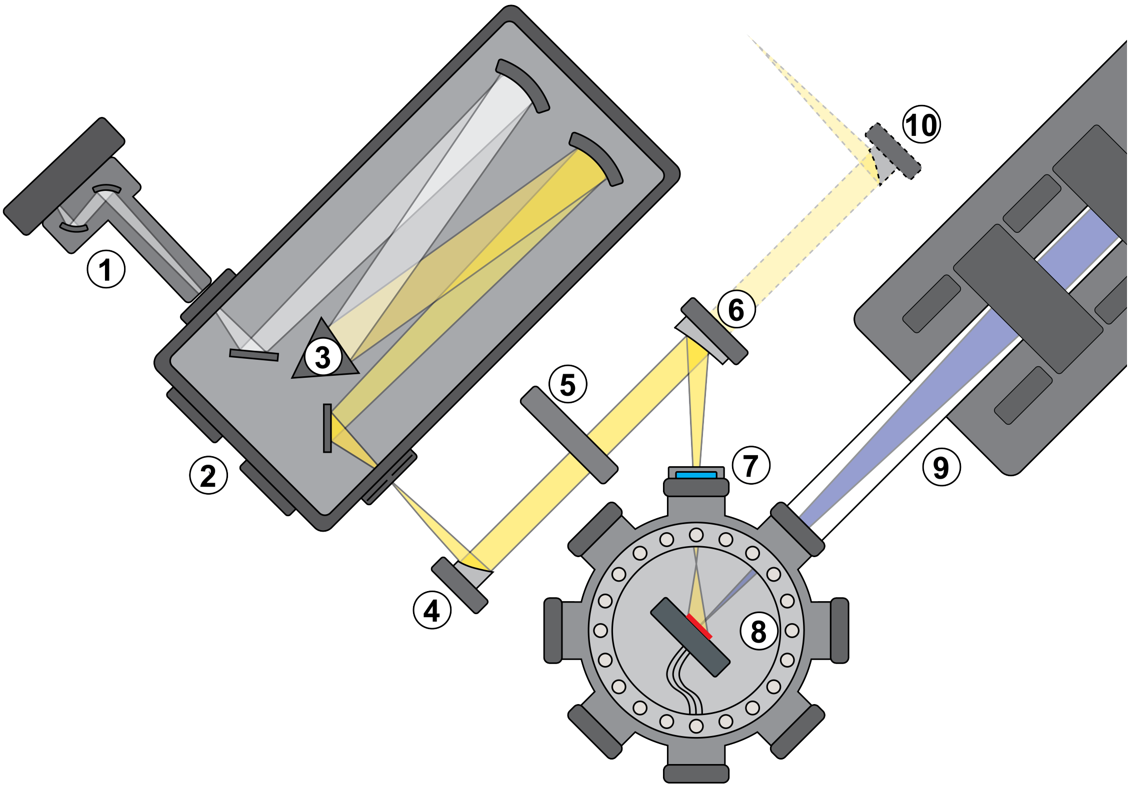

Figure 27: ① Broadband Laser Driven Light Source (LDLS) with parabolic mirror assembly. ② Spectrograph. ③ 3-slot reflective diffraction grating holder. ④ 1” 90° off-axis parabolic mirror. ⑤ Programmable filter wheel for 1” filter with 6 slots. ⑥ 3”45° off-axis parabolic mirror. ⑦ Custom window holder for sapphire window. ⑧ The online-chamber with sample holder in vacuum. ⑨ Ion-implanter beam-line. ⑩ Potential extension of the optical path for further development

resolution as well as resulting output power in dependence of the exit slit opening were tested.

The grating used in this study has a so-called blaze at 400 nm. That means it is most effective around 400 nm (see Fig. 69 in Appendix C). Hence, the gratings spectral response can be expected to be depend significantly on wavelength. One disadvantage of monochromators utilizing gratigs are second order effects. Grating monochromators disperse light spectrally by changing the angle between incident light and grating surface. Thereby a certain wavelength can be selected that will enter the beam path that leads to the output slit of the monochromator. When diffraction occurs, the angular direction for first order diffraction of light with wavelength $\lambda$ and the angular direction for the second order diffraction for light with the wavelength $\lambda/2$ will overlap. Hence, light at wavelength $\lambda$ and $\lambda/2$ will be steered to the output slit and leave the monochromator. Such second order effects must be compensated by optical elements in the light delivery system.

One of advantage of the monochromator used is its symmetric build-up which can be utilized at a later stage to add photoluminescence spectroscopy to the setup, where the monochromator will be part of the detection system for light instead of the excitation system.

#### 4.1.4.2 Light delivery system

A light delivery system from the monochromator to the vacuum chamber was developed, as shown in Fig. 27. One objective of the chosen layout was to minimize the beam path, to

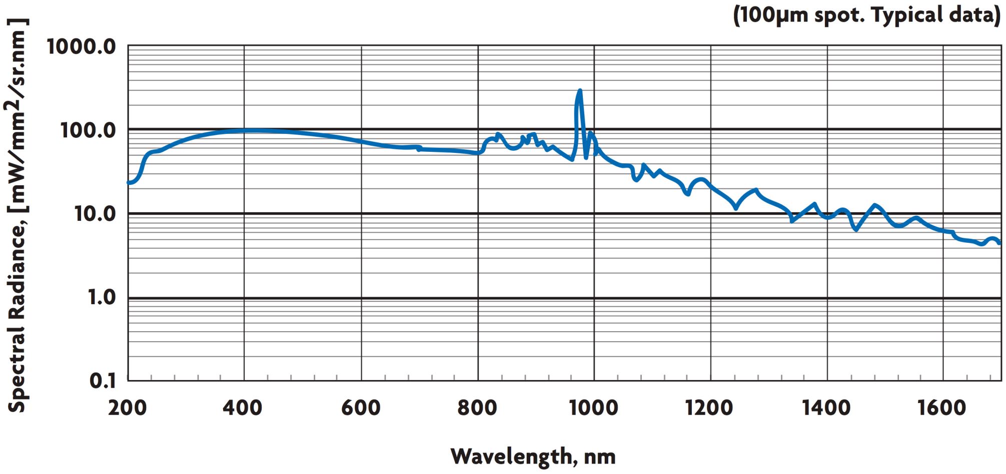

Figure 28: Spectral radiance vs wavelength of the Energetique EQ-77 LDLS[25]

reduce scattering losses, make enclosure and save space. Enclosing the setup is beneficial because this enables purging of the entire beam path to reduce gas absorption and also for laser safety. Furthermore, making sure that a part of the beam path was collimated(from ④ to ⑥) was beneficial since filters were being introduced in the system, a collimated beam is reduces potential optical aberrations that can occur in the filters. Another benefit of having a collimated beam is that the beam path can be extended significantly without losing intensity.

All optical components introduce spectral losses in some way, e.g., absorption in the optical component or scattering losses. Routing light from the light source, to the spectrograph and then to the sample without significant losses was important. Lenses are refractive optics that utilize refraction in order to e.g. focus or defocus a beam. Mirrors are reflective optics that can also be used to alter the beam path, as well as focus or collimate a light beam. The main disadvantage of using lenses in the online-setup is that lenses generally have a low spectral band width. As an example, lenses made from UV fused silica have a transmission range from 185 nm to 2100 nm[27]. Mirrors, on the other hand, generally have wider spectral range than lenses and can also alter the direction of a light beam. The light exiting the spectrograph is a divergent beam that eventually has to be focused onto the sa to maintain light intensity. Since lenses are less suitable, two OAP mirrors (④ and ⑥) were used to control the beam path as shown in Fig.27. OAP mirrors are designed to focus collimated light without introducing spherical aberrations. Parameters of interest are the effective reflected focal length and angle of reflection from the central ray axis. OAP mirrors can either focus a collimated beam or collimate a divergent bream based on the focal distance. A drawback is that OAP mirrors have a much smaller selection of focal lengths compared to lenses, but have the advantage of maintaining a high spectral bandwidth. A dissadvantage of OAP mirrors is that deviations between the incident light and the optical axis introduce comatic aberrations[28]. This can cause distortions in imaging techniques e.g. photoluminescence (PL) imaging. Such distortions are not a critical issue when conducting SSPC.

The first OAP mirror is 1”, thus the beam size in the section with parallel rays (from ④ to ⑥) is 1”. The distance from mirror to sample required a 3” OAP mirror, due to the limited selection of focal length of OAP mirrors. Since the sample size is 5x5 mm, a tightly focused beam is not needed for SSPC. In order to illuminate the whole sample the 45° OAP mirror was positioned further away from the sample than the focal point. This results in a defocusing of the beam, effectively increasing the spot size as illustrated ⑧.

A drawback of a monochromating system utilizing gratings are higher-order artifacts,

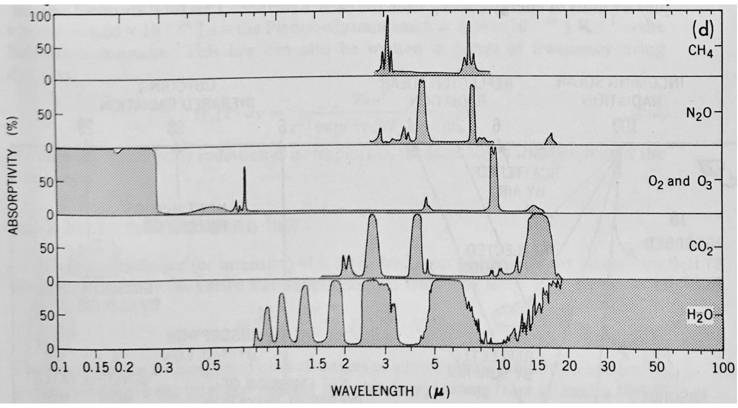

Figure 29: Absorption spectrum of common species in air: $CH_4$, $N_2O$, $O_2$, $O_3$, $CO_2$, $H_2O$. From Peixoto [29]

e.g., a certain grating positions not only light with one wavelength is reflected, but an additional contribution from the double of the set wavelength. Longpass filters can be used to filter-out the wavelength which is not desired. By programatically switching filter during a measurement, continues wide spectral measurements can be conducted. For this purpose, a programmable filter wheel was installed in the collimated beam path of the online-setup, shown in Fig. 27(⑤), and Longpass(LP) filters from 400 nm up to 1500 nm were acquired.

To probe the entire band gap of wide band gap semiconductors ($E_g > 3.1\,\mathrm{eV}$), high energy photons are required. When managing light in the Ultra-violet (UV) part of the electromagnetic spectrum it is important to also take gas absorption into account. Oxygen and Ozone from the air have a significant impact on light intensity, as shown in Figure 29 displaying absorption spectra for various gasses included in air. Ozone is generally formed in, e.g., the spectrograph due to the interaction of oxygen and deep UV light. The influence of atmospheric gas absorption was limited by purging the spectrograph with nitrogen ($N_2$) gas.

A benefit of the collimated light path is also that it enables the light source and spectrograph to be used for other potential experimental setups in the future. As illustrated in figure 27, a concrete example would be to remove mirror ⑥ and implementing another 90° off-axis parabolic (OAP) mirror ⑩ further down the beam path that focuses the beam back on to the optical table. Suggestion for further development is to develop e.g. a room temperature SSPC setup that can be run outside of the online-chamber or other experimental setups that utilize near-monochromatic optical excitation at variable wavelength.

### 4.1.5 Optical performance

Control over the intensity as well as spectral distribution of the light delivered to the samples is essential in order to understand the results of SSPC and DLOS measurements. Optical parameters of interest are: the spectral power distribution, photon flux, spectral resolution and wavelength offset. Most of the parameters are related to the light source, grating and spectrograph used in the system, but also mirrors, filters and other external factors influence the results.

#### 4.1.5.1 Power spectrum

The optical output power dependents on wavelength or photon energy, was measured using a Si photodiode (PD) and a thermal sensor. The PD and thermal sensor differ in range and sensitivity as explained in section. Tests where performed with the sensors placed on both sides of the sapphire window ⑦. The tests with the PD/thermal sensor were performed on different days. The tests performed can be summed up as follows: Measuring the power spectrum

- with and without longpass filters
- with variable output slit width
- with variable input slit width

Fig 30 shows the power spectrum recorded with both sensors inside the vacuum chamber, including measurements with variable output slit width for the PD. The spectral shape is fairly similar for both sensors and also for different output slit widths. The shape itself follows quite closely the spectral response of the grating used (see Fig. 69). This underlines the fact that the mirrors used do not introduce significant spectral distortions. The difference between the measured curves recorded with the PD and the thermal sensor are most likely due to the different day of measurement and/or slightly different positions of the corresponding measurement sensor. This indicates spectral and fluctuations of the spectrograph and light source output. As expected, with less open output slit width, a decrease in light intensity can be seen.

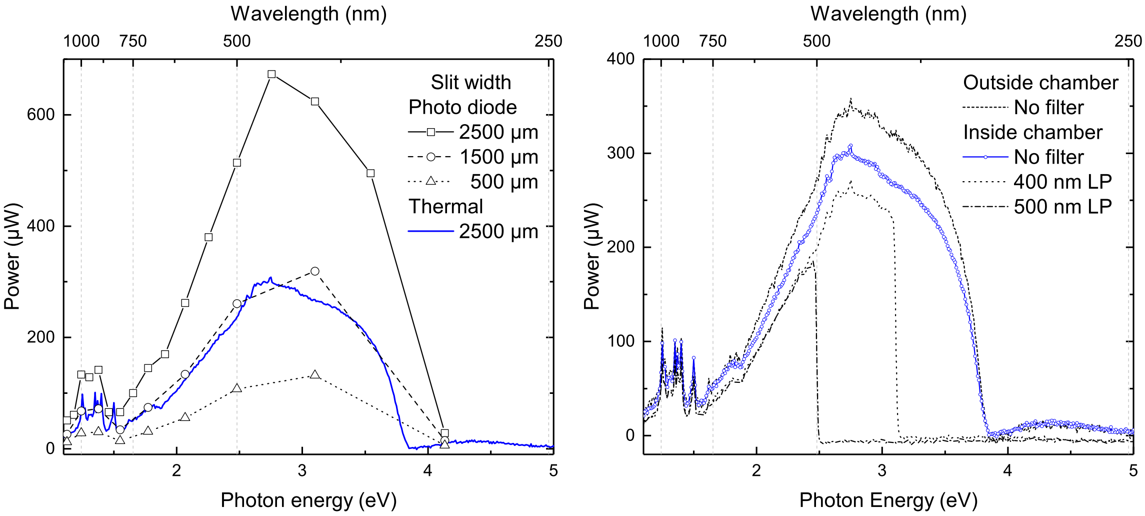

(a) Power spectrum comparing output slit width of the Shamrock 500i spectrograph. Lines with symbols are measured with Si-Photo diode, Solid blue line are measured with high resolution thermal power meter.

(b) Power measurements done with thermal power meter. Inside/outside the online-chamber and with/without Long-pass filters

Figure 30: Spectral power distribution of the online-setup measured with Si-photo diode and thermal power meter

Fig. 30b shows results, obtained with a thermal sensor inside and outside the vacuum chamber as well as using LP filters. Power measurements from inside and outside the chamber indicate that the sapphire window does not induce any distortions to the spectral distribution, only a reduction in intensity. The power reduction is assumed to mainly arise from reflections in the sapphire window, that is without anti-reflective coating. The beam-path, from spectrograph to chamber was encapsulated to prevent stray light, but not purged. It is assumed that absorption from atmospheric gasses might be one cause of the strong reduction in power in the UV-region. To maximize the potential of the light source, it is recommended that further studies are carried out to investigate how

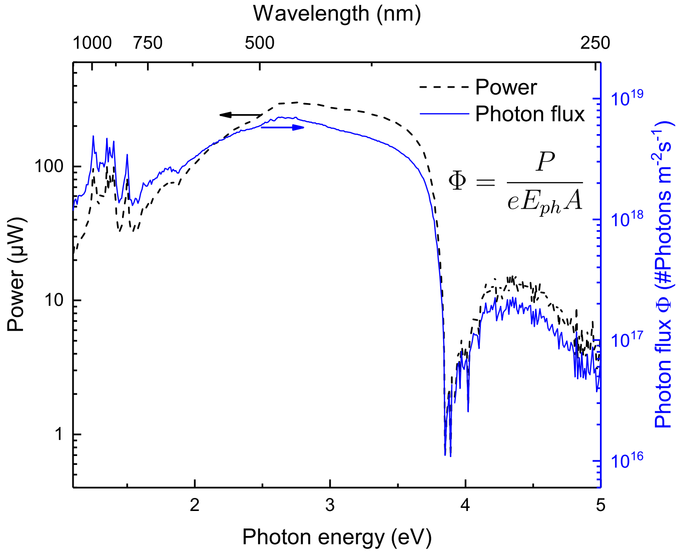

Figure 31: Photon flux calculated from power measurements inside chamber with no filter. Area was estimated to be 1 cm$^2$

purging the entire beam path influences the power spectrum. The filter performed as expected, shown in Fig. 30b, with an abrupt cut-off at the specified wavelength and high transmittance above the cut-off, Assuming that the beam was focused so the entire active sensor area ($A = 1\,\mathrm{cm}^2$) was illuminated, the estimated photon flux was calculated, Fig. 31. It is important to notice that although the power measurements indicate close to ∼10 µW for photon energies above ∼4 eV, there is still a significant amount of photons illuminating the sensor.

#### 4.1.5.2 Spectral resolution

Fig.32 shows the spectral distribution of the spectrograph output measured, when the spectrograph is set to a nominal wavelength of 1000 nm. The output slit width of the spectrograph was varied and the output was measured with another spectrometer. Fig.32 show the measured intensity for different slit widths as a function of photon energy $E_{ph} = 1240\ [\mathrm{nm\,eV}]/\lambda[\mathrm{nm}]$. it is evident that 2nd order artifact is generated by the reflective diffraction grating in the spectrograph. To suppress 2nd order artifacts, appropriate LP filters where used.

Using the data shown in Fig. 32 and similar data sets acquired at nominal wavelengths of , the spectral resolution and spectral offset of the spectrograph can be investigated. Gaussian functions where fitted to the peaks to obtain Full Width of Half Maximum (FWHM) and position. The FWHM and the offset of the photon energy set by the spectrograph is shown in Fig. 33 as a function of the output slit width. It is apparent that decreasing slit width decrease the energy offset and the energy spread, thus, increasing the overall resolution of the output signal. The energy spread also seems to increase with increased photon energy. The study show that the energy spread of the high resolution grating is relatively low, where the larges spread is seen to be approximately 17 meV.

Figure 34 illustrate the difference between changing slit width of the input and output of the spectrograph. No significant difference in spectral resolution was observed for changing input or output slits. For the SSPC study described later, the main concern was to retain the highest radiance as possible, so due to the low energy deviations, measurements were done with fully opened slits at 2500 µm.

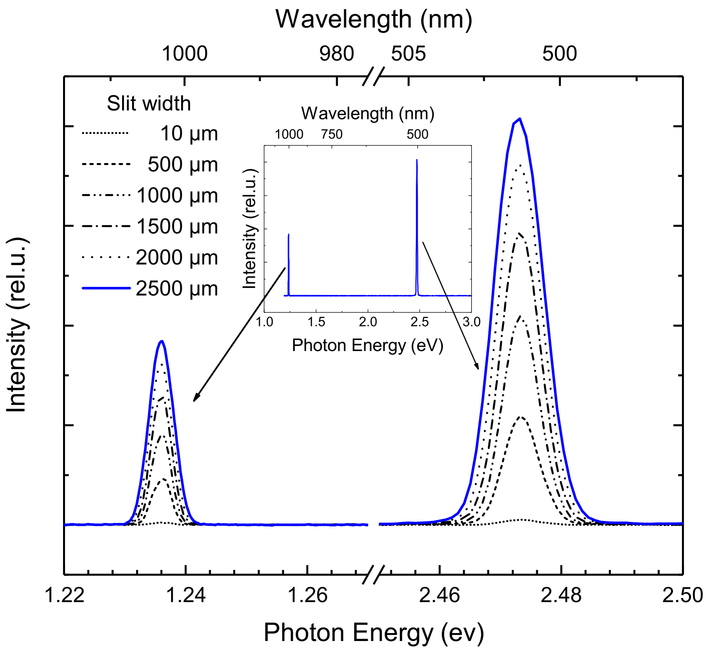

Figure 32: Observed intensity of monochromatic light from the Shamrock 500i spectrograph set to 1000 nm wavelength showing a 2nd order artifact from the reflective diffraction grating at 500 nm. Higher order artifacts should be lower in intensity, but due to the spectral efficiency of the grating (see Fig. 69 in appendix C) with a blaze 400 nm, the 2nd order is more intense than the first order.

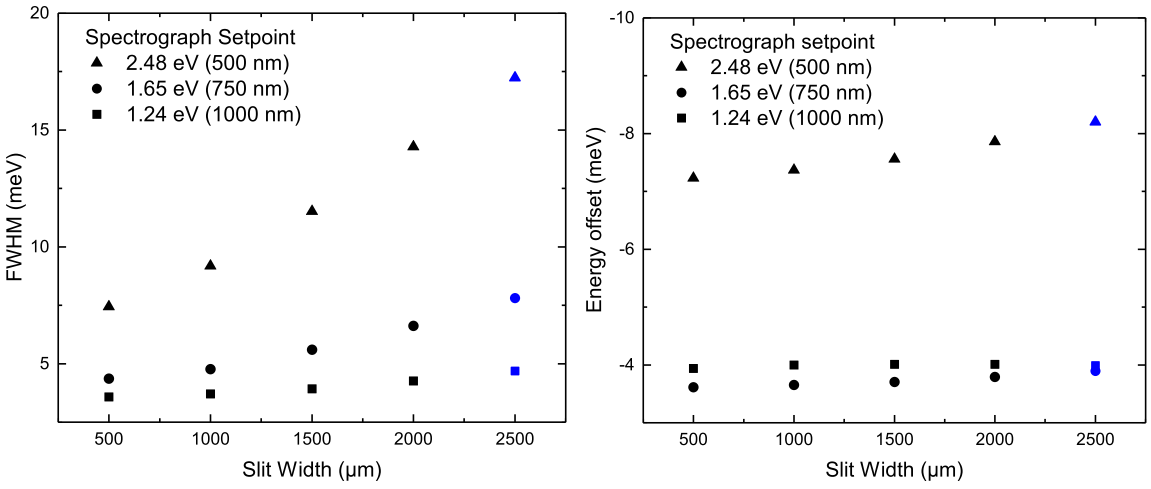

(a) FWHM

(b) Photon energy offset

Figure 33: Measurements of the photon energy resolution and offset from the Shamrock 500i spectrograph set to 500 nm, 750 nm and 1000 nm wavelength for different output slit widths.

## 4.2 Experimental Verification using the semiconducting oxides $\beta$-$Ga_2O_3$ and ZnO

In this section, the experimental results acquired utilizing the online-setup on two different materials ($Ga_2O_3$ and ZnO) will be presented, where special emphasis has been punt on $\beta$-$Ga_2O_3$ as previously stated. The results from each material will be presented separately,

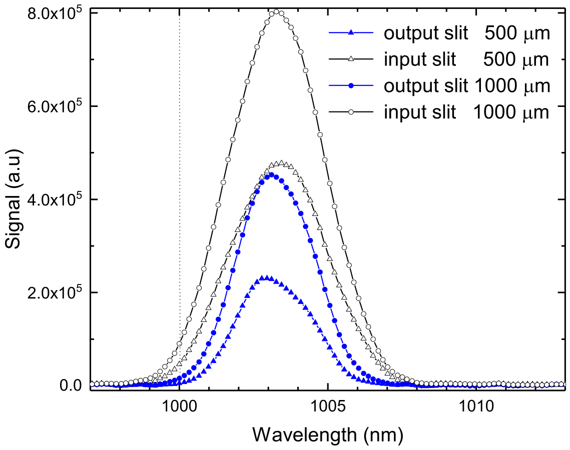

Figure 34: Comparison on how variations in input and output slit width of the spectrograph effects the spread and offset of the output signal

beginning with the contact quality assessed by IV and CV measurements. Afterwards, results concerning electrically-active defects in the two materials will be presented and discussed. These results were obtained by utilizing DLTS. Thereby the online setup as well as established DLTS setups at MiNaLab were used. Lastly, results from SSPC measurements will be presented and discussed thoroughly, since this has been a large part of the development and a major advance from previous systems.

### 4.2.1 $Ga_2O_3$

All measurements presented in this section are from the same contact on a $Ga_2O_3$ sample, but similar results can be found from other contacts. The contact geometry is displayed in Fig.25, whereby a diameter of 600 µm was used.

#### 4.2.1.1 IV/CV - Contact quality

Figure 35 and 36a show IV and CV data obtained with the online-setup. To verify that the contacts would perform under the required temperature ranges for DLTS and SSPC, measurements was conducted at room temperature and 120K.

IV results show that rectification of about 3 to 4 orders of magnitude were achieved for the contact at 120 K and 280 K respectively. It is apparent that the contact characteristics for reverse bias voltages below $-1$ V changes slightly and may be a cause of decreased shunt or parallel resistance.

The CV results in Fig.36a display that the $1/C^2$ curve increases linearly, as expected. Extrapolating $1/C^2$ curve to the x-axis intercept yielded a built in voltage of 1.70 V at 280 K and 1.87 V at 70 K.

Calculation of the carrier concentration from $1/C^2$ shown in Fig.36b show a fairly uniform doping concentration of $1.2 \times 10^{-17}$ at 280 K, and a small increases to around $1.3 \times 10^{-17}$ at 70 K. Carrier concentration specified by the manufacturer show similar values of $1.5 \times 10^{-17}$, and thereby verifying the contact geometry and experimental setup.

IV and CV results indicate that the developed contact design and procedure is able to produce contacts with rectifying behaviour at high and low temperature. This makes the contacts suitable for both DLTS and SSPC studies.

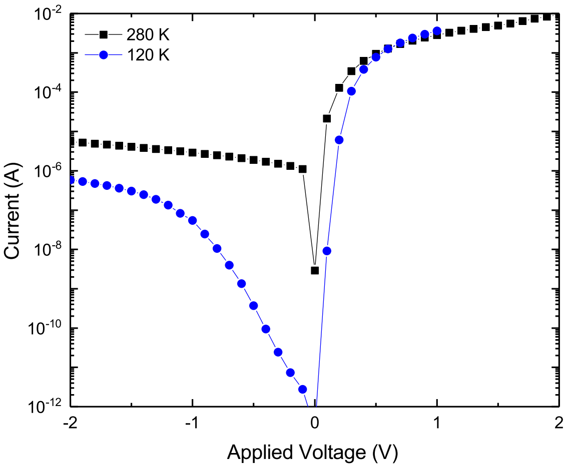

Figure 35: IV measurements of $Ga_2O_3$ at 120 K and 280 K, showing rectification of about 4 and 3 order of magnitude respectively

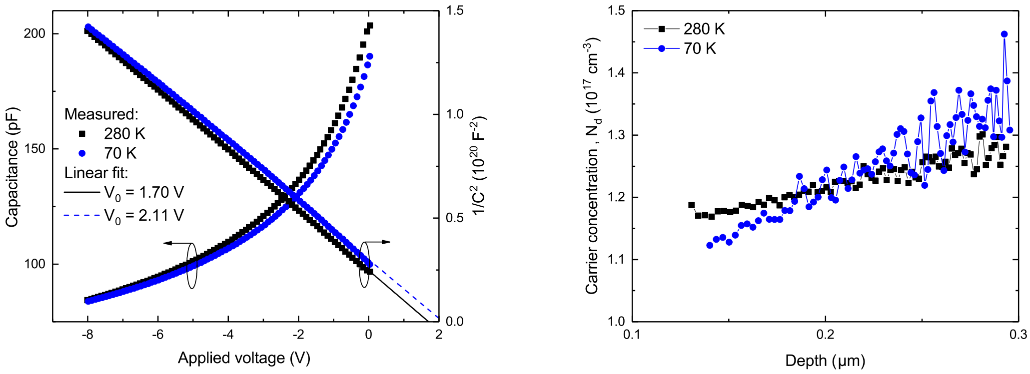

(a) CV measurements of $Ga_2O_3$ at 70 K and 280 K. Extrapolation of $1/C^2$ to the x-intercept yield values for the built in voltage

(b) Carrier concentration vs depth calculated from CV measurements on $\beta$-$Ga_2O_3$ at 120 K and 280 K

Figure 36: CV measurements on $\beta$-$Ga_2O_3$ at 120 K and 280 K with a) CV and $1/C^2(V)$ and b) carrier concentration as function of depth

#### 4.2.1.2 DLTS - Electrically-active defects

The DLTS measurements was carried out were on the same contacts as discussed in the IV/CV section above with a minimum window length of 100 ms, 6 windows and 5 ms delay time.

At least two defect levels are observed; one with a peak signature around 220 K when using window 6, and one with an expected peak slightly above room temperature, i.e., above the maximum temperature available in the online-setup. Qualitatively, the two defect levels are in accordance with the E1 and E2 peaks previously reported in the literature [24, 30, 31]. The E1 level is found to have energy level position around 0.48 eV below the conduction band edge, while the reported value by Ingebrigtsen is around 0.56 eV. The origin of this defect remains unknown, but it has been proposed to arise from an impurity. The E2 defect on the other hand, has been shown to arise from Iron, which is a common impurity in bulk Ga2O3 samples [24]. Hence, the present results corroborates previous observations and demonstrates that the online-DLTS system works.

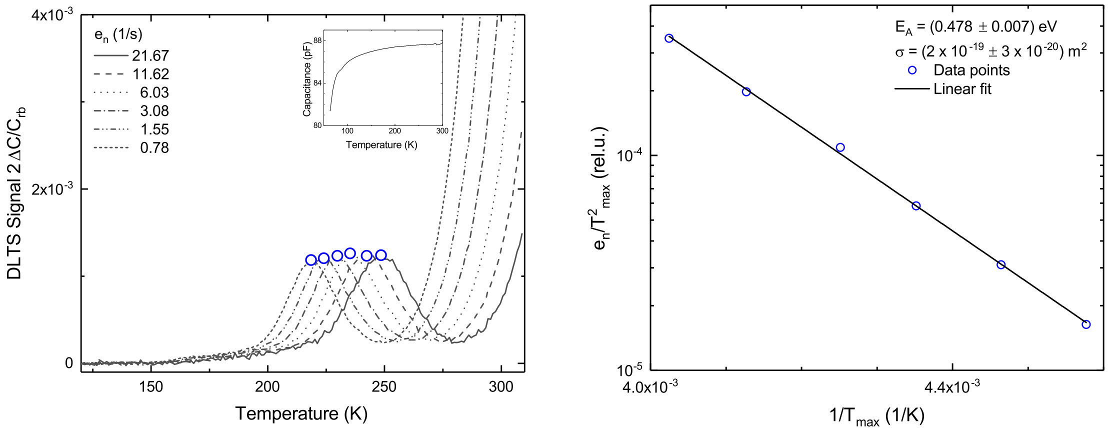

(a) DLTS a of bulk $\beta$-$Ga_2O_3$ with a (010) surface orientation. DLTS measurements was conducted before irradiation

(b) Arrhenius plot of the peak positions in the DLTS spectra in a)

Figure 37: DLTS and Arrhenius plots of measurements done on a $\beta$-$Ga_2O_3$ sample before irradiation

#### 4.2.1.3 SSPC

In this section the results from the first SSPC measurements from $\beta$-$Ga_2O_3$ will be presented.

**How to present SSPC data** Figure 38 illustrates how the SSPC signal is obtained. SSPC requires a material to be at steady state conditions for each data point in the SSPC spectrum. This is achieved by illuminating a sample with monochromatic light at a known photon energy for a sufficient time in order to achieve a steady state. At the end of the illumination time, a set of the last values are averaged to give one data point representing the steady state value at that photon energy. In this study a illumination time of 300 s was used and capacitance was acquired every 250 ms. The last 20 data points (4 s) were used for averaging. By repeating the $C(t)$ measurement for several different photon energies, saving the last capacitance values and plotting their average as function of photon energy, a SSPC spectrum is obtained. The main graph in Fig. 38 shows how the capacitance changes with time under illumination with monochromatic light between 3.3 eV and 5 eV. Each $C(t)$ represents a data point in the graph shown in the inset, which illustrates the final SSPC plot, as shown in Fig. 38

### Technicalities on measuring a SSPC spectrum

To understand how the measurement parameters influence the SSPC spectrum, a thorough investigation was conducted. This was also done as a way to verify that the features seen are caused by a response in the material, rather than artifacts from the online-system itself. The following was investigated:

- Measurements with increasing or decreasing photon energy steps

- Required illumination time to reach a steady state

- The effects of pre-illuminating a sample before measurement start

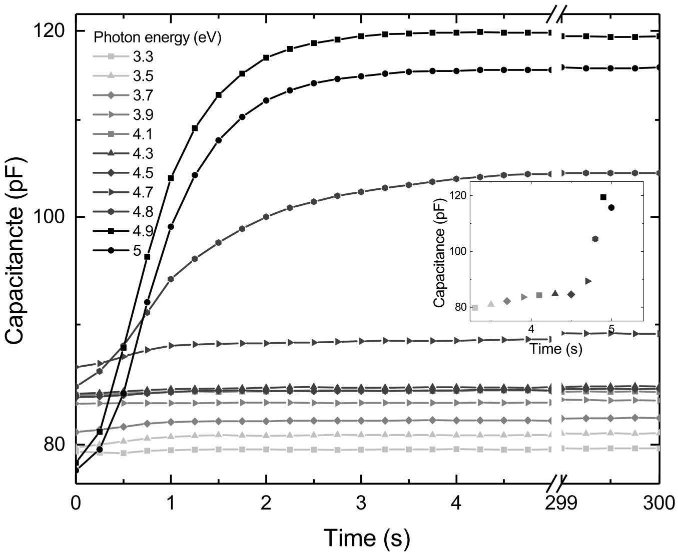

Figure 38: Illustration of how the SSPC signal (inset) is generated from capacitance vs time measurements, recorded during illumination with near-monochromatic light.

- How the initial capacitance in dark $C_0$ influences the SSPC spectrum

**Photon energy sweep** In principle, one can either record a SSPC spectrum by increasing or decreasing the photon energy from the subsequent measurements. The so-called sweeping direction was investigated by measuring one spectrum with increasing and one with decreasing photon energy. Both measurements were performed at room temperature without filters. The results obtained are shown in Fig.39.

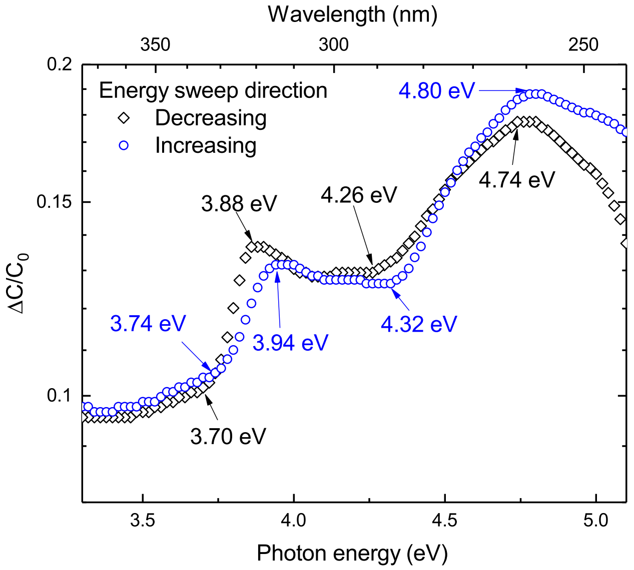

Figure 39: Room temperature SSPC measurements with increasing and decreasing photon energy sweeps.

When analyzing Fig. 39, one needs to consider how light interacts with traps in the depletion region. As discussed in the theory section, when light with energy $E_{ph} = h\nu$ interacts with a semiconductor, electron excitation from traps with $E_t$ may occur if the energy gap between the trap and the conduction band is less than the photon energy of the incident light $(E_C - E_t) < E_{ph}$ (see Fig. 5). This means that for each increase in photon energy in a SSPC measurement, the amount of possible traps that can be excited increases for each subsequent measurement. The inverse is true if measuring SSPC with decreasing photon energy, where the possible trap excitation decreases with each subsequent decrease in photon energy. If a steady state is not reached at one photon energy step, a shift can occur in the SSPC signal. The sweep direction seems to have low impact on the SSPC spectrum, but the general trend is that all peaks and onsets are shifted based on the sweep direction. Figure 39 confirm that all extrema are shifted and appear at higher photon energies for increasing energy sweep, compared to decreasing sweep direction. It is recommended for further studies to map the SSPC spectrum in both sweep directions to better understand how deep traps respond to optical stimuli. Furthermore, it should be investigated if similar results can be achieved for low temperature SSPC. In the following, all measurements were conducted with increasing photon energy sweep direction.

**Illumination time** According to equation 2.42 the interaction between light and the material is a time-dependent process. SSPC measurements rely on the material to be at steady state when acquiring data. Earlier studies on ZnO [32] document illumination times of 300 s to achieve steady state. From Fig. 38 it seems like steady state condition is achieved after approximately 5 s. It is beneficial to investigate if shorter illumination times can achieve similar results due to the often very long measurement times required. For example, a SSPC spectrum using 300 s illumination time per data point, from 1 eV up to 5 eV with 20 meV increments take about 16.5 hours to complete. By reducing the illumination time to 100 s the total measurement time amounts to only 5.5 hours. Shorter measurement time is not only beneficial from an experimental point of view, but can also avoid too pronounced degradation of samples. Some materials and contacts tend to degrade when put under, e.g., electrical stress. Thus shorter measurement times enables more measurements to be conducted before the sample is fully degraded. Figure 40 show results obtained from two SSPC spectrum at 120 K with 100 s and 300 s illumination time. It can be seen that all features are shifted towards higher photon energies when illumination time is decreased. The signal extremas are also shifted for the case of lower

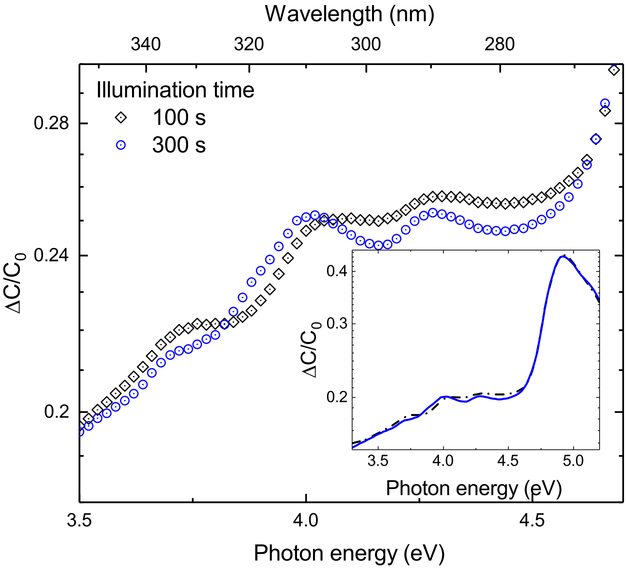

Figure 40: SSPC measurements showing how change in illumination time effects the spectrum.

illumination time, showing lower signal response and flatter curves. Reducing illumination seems to inhibit the hole response. The result shows that illumination times of 300 s generate SSPC plots with more pronounced features compared to 100 s, and is therefore used in this study.

**The effect of pre-soak** SSPC measurement on $\beta$-$Ga_2O_3$ revealed that the sample often did not reach steady state within 300 s at the start of th measurements. In order to achieve a steady state at the start of a measurement, the sample was illuminated (pre-soaked) with near-monochromatic light at the desired starting photon energy for 30 min. This pre-soak enables optically induced emission from defect levels below the starting energy of the measurement. A comparison of measurements with and without pre-soak at room temperature and 120 K are shown in Fig.41 (C vs $E_{ph}$). As expected, pre-saoking does not effect the entire SSPC signal, only the initial data points. From the inset of the figure, it can be seen that the first six data points (corresponding to 30 min of illumination) for the measurement without pre-soak display a tail that exhibits a lower signal than that for the measurement with 30 min pre-soak. Since pre-soaking does not influence the entire spectrum and works for both room and low temperatures, 30 min pre-soak was used in the irradiation study discussed later. A presoak dependence generally imply the presence of defect levels with a lower optical activation energy $E_a$ than the photon energy the SSPC measurement started with.

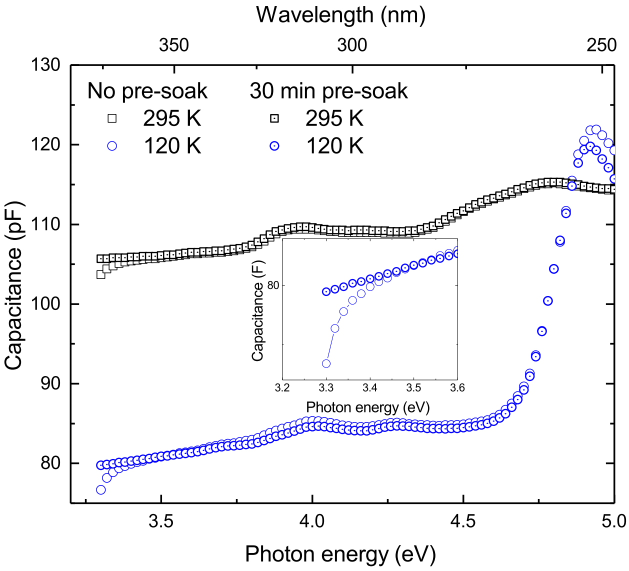

Figure 41: SSPC measurements with and without 30 min of sample illumination(pre-soak) before measurement start

**Effects of $C_0$** In the above discussion on pre-soaking, the data in Fig 41 was displayed as $C(E_{ph})$, rather than the usual $\Delta C/C_0(E_{ph})$. This was done to highlight the effect that $C_0$ have on the SSPC signal. Fig. 42 display the data from Fig 41 as $\Delta C/C_0(E_{ph})$. It is apparent that a shift in of the SSPC signal curve is displayed for measurements at 120 K, caused by different $C_0$ values. Since measurements were done consecutively, persistent charge in the material from previous measurements can influence the measured $C_0$ value. This shift in $C_0$ seems to be more pronounced in the case for lower temperature measurements, indicating that thermal processes influence the "reset" of the sample. This effect could be important to keep in mind when conduction low temperature SSPC measurements in order to enable quantitative analysis. It is assumed that persistent charges in the material can be prevented by either: increase the time between measurements, or introduce a forward biased filling pulse to "reset" the diode.

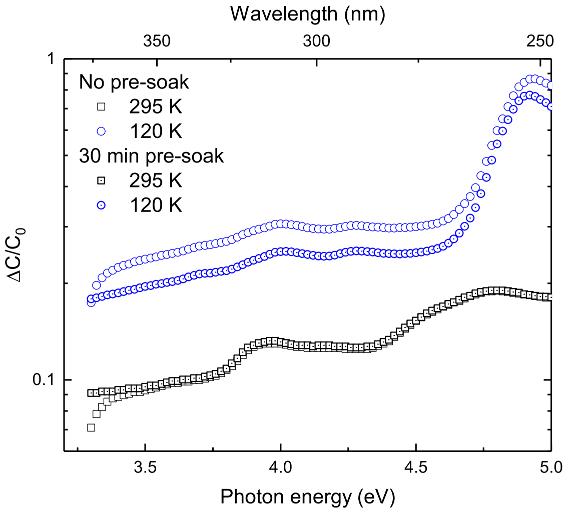

Figure 42: SSPC measurements illustrating the effect of 30 min illumination pre-soak at high and low temperature. Changes in $C_0$ can cause sifts in $\Delta C/C_0(E_{ph})$.

#### 4.2.1.4 Results from SSPC measurements on $\beta$-Ga$_2$O$_3$

At 120 K the signal clearly shows a response attributed to excitation of electrons from VB to CB with an onset of approximately 4.6 eV and a maximum at 4.9 eV. Further features are seen for lower photon energies, which correspond to electronic states in the band gap. This is illustrated in Fig.44 where a deconvolution of the individual contributions was performed.

For the room temperature measurement, the bandgap response is also seen, but a broadening of the onset is seen that is most likely due to higher influence of thermal emission processes as discussed in the experimental section. This clearly shows the need for low measurement temperatures in order to minimize thermal broadening on the SSPC signal.

Earlier SSPC studies have been carried out by Ringel [33] on $\beta-$Ga$_2$O$_3$ . From SSPC measurements at 300 K, Ringel obtained a bandgap signal at 4.84 eV and two positive onsets at approximately 2.20 eV and 4.40 eV. From Fig. 43, similar results were obtained at room temperature where a signal related to excitation from the CV to the CV can be seen at 4.8 eV. Furthermore a positive onset can be observed at 4.40 eV. No records of the observed defects at 3.70 eV, 4.00 eV and 4.28 eV from Fig.44 was found in literature.

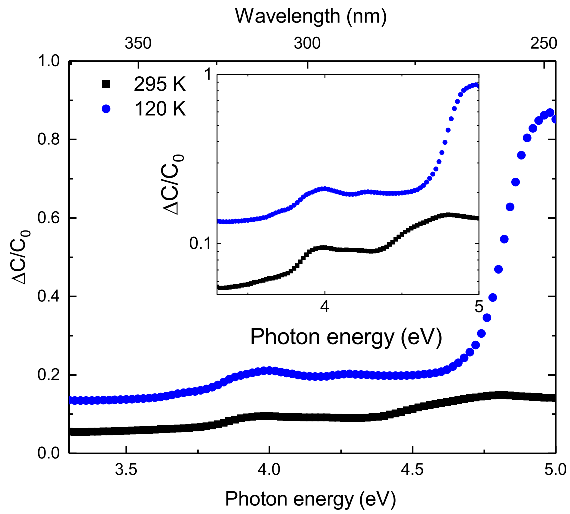

Figure 43: SSPC spectrum at 120 K and 295 K, illustrating the importance of low temperature in order to reduce the thermal emission processes so that the assumption of $e_n^o \gg e_n^{th}$ is fulfilled. Inset shows semi-logarithmic representation of the main plot.

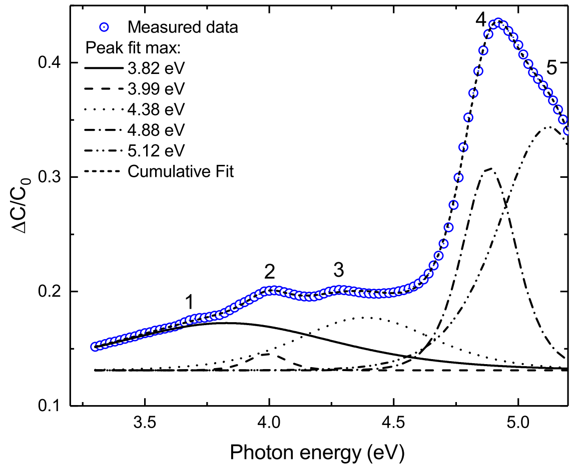

Figure 44: Deconvolution study of a SSPC signal at 120 K. The fitting was done with origin with the "logistpk" peak function.

#### 4.2.1.5 SSPC on irradiated $\beta$-Ga$_2$O$_3$

To test the capabilities of the newly developed online-setup, an irradiation study on $\beta$-Ga$_2$O$_3$ was conducted. The irradiation was done at 120 K, 600 keV and a dose of $1 \times 10^{13}$ protons. Simulations using SRIM software[18] suggest a implantation peak at a depth of 4.3 µm, thus only the implantation tail is within the probing region of IV, CV, DLTS and SSPC. The obtained results will be presented here by first showing the IV/CV characteristics of the contacts before and after irradiation. DLTS measurements will be presented in order to verify that electrically-active defects are present in $\beta$-Ga$_2$O$_3$ . Finally the SSPC results will be discussed.

**IV/CV** Figure 45 show the results from IV and CV measurements.

Before irradiation rectification of 3 to 4 orders of magnitude can be seen for room temperature and 120K respectively. Irradiation seems to have little effect on the contact characteristics. A small reduction in rectification is seen for both high and low temperature measurements, potentially caused by a decrease in shunt resistance $R_{sh}$. The less steep curve in the low reverse bias region for low temperature measurements also indicates a decrease in $R_{sh}$, compared to high temperature measurements. Calculated values for $I_0$, $n$, $R_s$ and $R_{sh}$ are presented in Tab 5.

There is however a kink in the IV curve after irradiation at 1.5 V, which may suggest that the proton irradiation had a (but no significant) damaging effect on the contact. IV measurements indicate that the contact characteristics was fairly unchanged through the irradiation study.

CV measurements from Fig. 45b show the expected decrease in capacitance with reduced temperature. Irradiation also decreases the overall capacitance of the sample, which is suspected be a result of creation of defects inside and/or outside the probing region. The implantation depth of the study was deeper than the probing range, thus only the tail region of the implantation is possible to investigate with CV. Further investigations of $1/C^2$ shows that irradiation decreases the built in voltage and also the carrier concentration, which agrees with the capacitance decrease observed in the CV. CV measurements before and after SSPC at 120 K after irradiation were done in order to detect if irradiation and illumination degrades the contact. CV measurements show satisfactory contact performance.

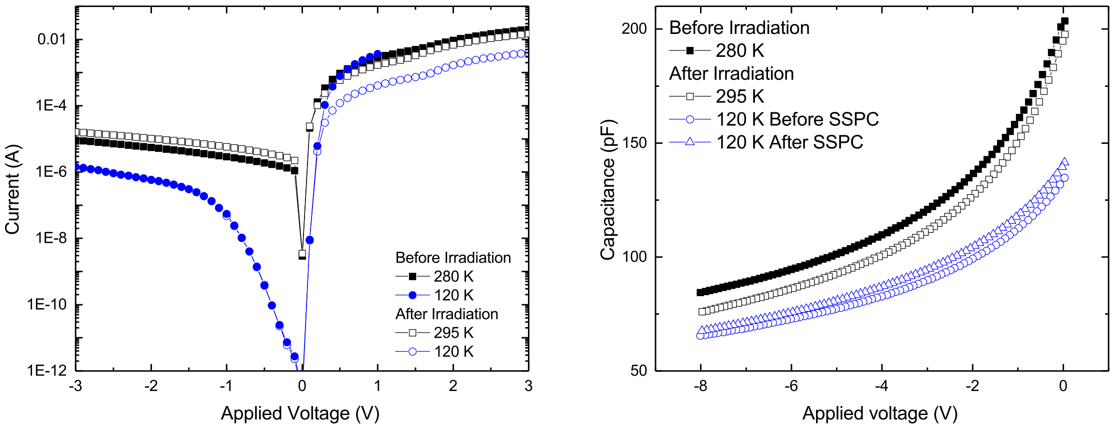

(a) IV results

(b) CV results

Figure 45: IV and CV results at room temperature and 120 K, before and after proton irradiation at 600 keV with a dose of $1 \times 10^{13}$

| **Irradiation** | $T$ [K] | $I_0$ [A] | $n$ | $R_s$ [Ω] | $R_{sh}$ [Ω] |
|---|---|---|---|---|---|
| Before | 120 | $2.776 \times 10^{-12}$ | 1.287 | 719.9 | $1.669 \times 10^{11}$ |
| | 280 | $7.965 \times 10^{-7}$ | 1.215 | 310.1 | $0.4841 \times 10^{6}$ |
| After | 120 | $2.354 \times 10^{-12}$ | 1.287 | 2240 | $7.8473 \times 10^{10}$ |
| | 295 | $2.336 \times 10^{-6}$ | 1.143 | 721.0 | $0.4391 \times 10^{6}$ |

Table 5: Values for $I_0$, $n$, $R_s$ and $R_{sh}$, calculated from IV results of irradiation study on $\beta$-$Ga_2O_3$ (see Fig. 45a). Calculations was done with a Pyhton script developed by Christian Zimmermann

From IV and CV analysis the contacts show satisfactory performance throughout the study, verifying that further defect studies may be conducted.

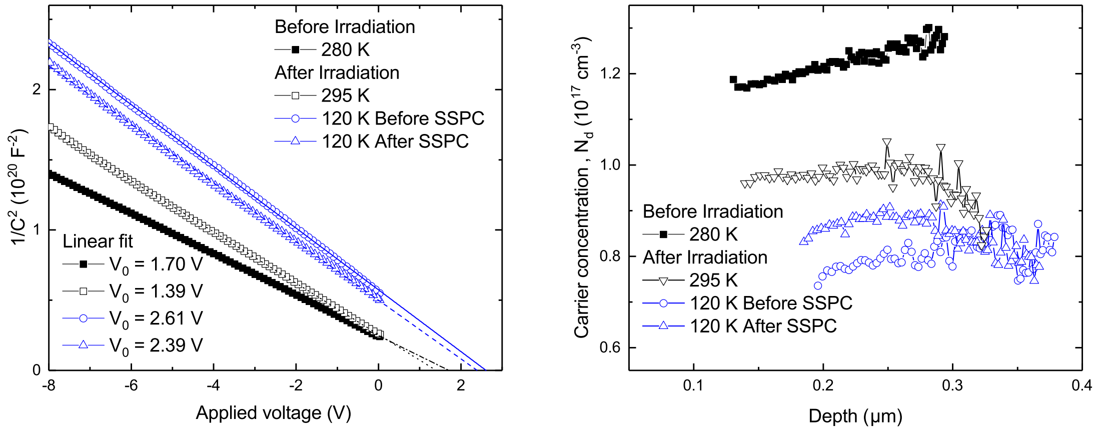

(a) $1/C^2$ vs applied bias

(b) $N_d$ vs Depth

Figure 46: Results of $1/C^2$ and carrier concentration vs depth at room temperature and 120 K. Measurements were conducted before and after proton irradiation at 600 keV with a dose of $1 \times 10^{13}$

**DLTS** DLTS measurements after irradiation is was conducted with the same parameters as described in Sec. 4.2.1.2. The DLTS spectra and corresponding Arrhenius plot is shown in Fig 47. It is apparent that shape of the DLTS spectra was changed after irradiation. The inset in Fig. 47a display the capacitance vs temperature, which changed compared to the DLTS measurement before irradiation. The capacitance decreases steadily with decreased temperature to approximately 230 K, then increased before decreasing again from 175 K. Ideally C(T) should show a steady decrease in capacitance with decreased temperature to carrier freeze out. The valley feature in the C(T) suggests less ideal contact performance, but is not indicated in IV or CV measurements. The feature also appear in the temperature region of the E2 peak, which could be the reason for the change in peak shape. From the Arrhenius plot a much higher activation energy was obtained for the E2 peak, at 0.59 eV. That is approximately 0.09 eV higher than before irradiation. The cause of the change in the DLTS could be due to the proton irradiation, or simply contact degradation due to electrical or optically induced stress on the contacts. Investigating this, however, is out of the scope of this thesis.

**SSPC** SSPC measurements where conducted at room temperature and 120 K before and after proton irradiation at 600 keV with a dose of $1 \times 10^{13}\,\mathrm{cm}^{-3}$. Figure 48 shows the results obtained from SSPC measurements. Before investigating the possible origin of features in the obtained SSPC spectrum, the curve shapes will be discussed.

As mentioned in the CV analysis, lattice damage from the implantation (only tail) could result in charge carrier compensation inside the probing region, thus lowering the overall capacitance signal obtained in CV. Results from Fig.48 displays a increase in $\Delta C/C_0(E_{ph})$ with irradiation for high and low temperature measurements.

For room temperature measurements, irradiation seems to have little effect on the spectral shape of the SSPC curve. For the low temperature measurements, a zoomed-in region of the spectra before and after irradiation is shown in Fig.49. Although the peak onset of a SSPC spectrum is the parameter of interest, onsets can be hard to obtain. Peaks, on the other hand, are easier to point to and are therefore highlighted in Fig.49 to show the influence of irradiation. The main difference is that the center peak at approximately 4.0 eV have a shoulder at ~3.9 eV before irradiation at 120 K. After irradiation, the peak at ~3.9 eV is not apparent anymore, or having a lower capacitance change compared to that

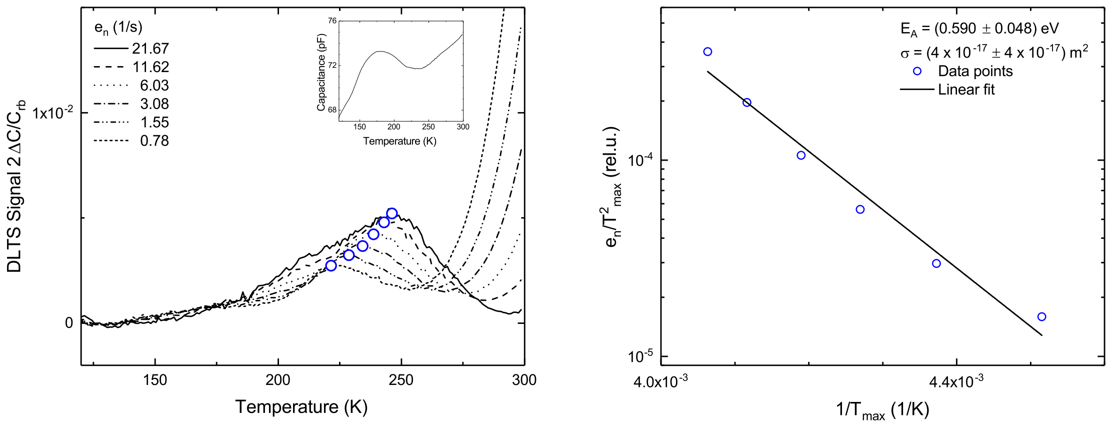

(a) DLTS a of bulk $\beta$-Ga$_2$O$_3$ with a (010) surface orientation. DLTS measurements was conducted after proton irradiation at 600 keV with a dose of $1 \times 10^{13}$ cm$^{-3}$

(b) Arrhenius plot of the peak positions in the DLTS spectra in a)

Figure 47: DLTS and Arrhenius plots of measurements done on a $\beta$-Ga$_2$O$_3$ sample after proton irradiation at 600 keV with a dose of $1 \times 10^{13}$ cm$^{-3}$

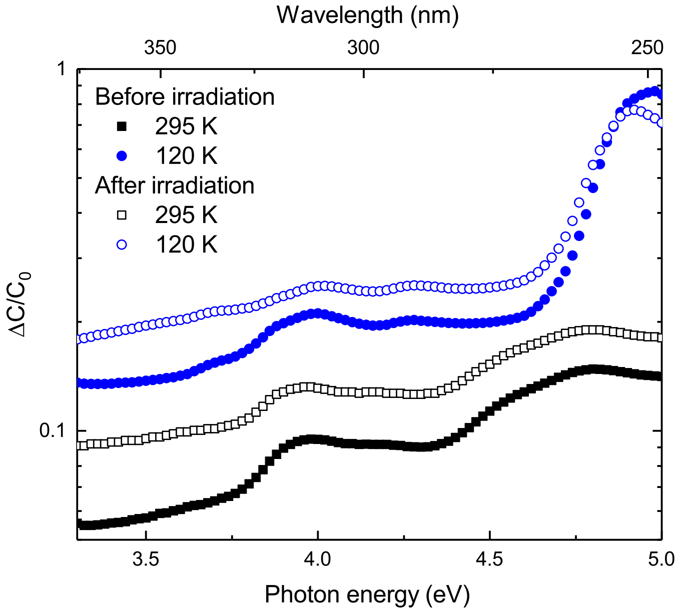

Figure 48: SSPC results obtained before and after proton irradiation at 600 keV with a dose of $1 \times 10^{13}$ cm$^{-3}$. Irradiation decreases the defect signal, indicating possible compensation outside the probing region.

of the 4.0 eV feature. Further investigations into SSPC are however necessary to clearly reveal irradiation-induced defect levels. Conducting a SSPC study that investigates dose dependency and implantation depth response would be of interest.

Fig. 50a summarize the results obtained after irradiation for high and low temperature. Since a goal was to verify the setups capability to conduct online measurements, results from room temperature is compared to the work of Ringel [31]. Similar room temperature SSPC studies were carried on $\beta$-Ga$_2$O$_3$ by Ringel where two deep defects where observed by SSPC. The two defect levels were assigned onsets at 2.20 eV and 4.40 eV respectively. From

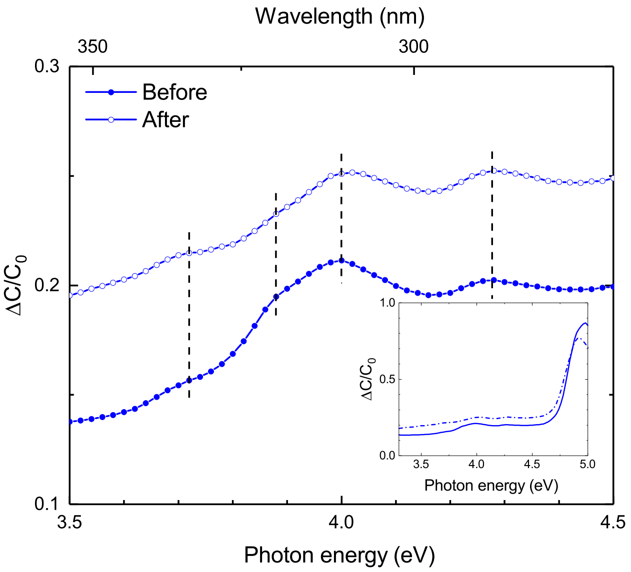

Figure 49: SSPC spectrum on $\beta$-Ga$_2$O$_3$ , comparing features before and after proton irradiation. One feature at approximately 3.9 eV seems to be much less apparent after irradiation, comparred to before.

the room temperature SSPC spectrum in Fig.50a, similar onsets are observed and thus further verify the observed features. One additional feature with onsets at 3.76 eV is seen for room temperature measurements. For measurements conducted at 120 K, additional defect levels are observed and are summarized in Fig.50b.

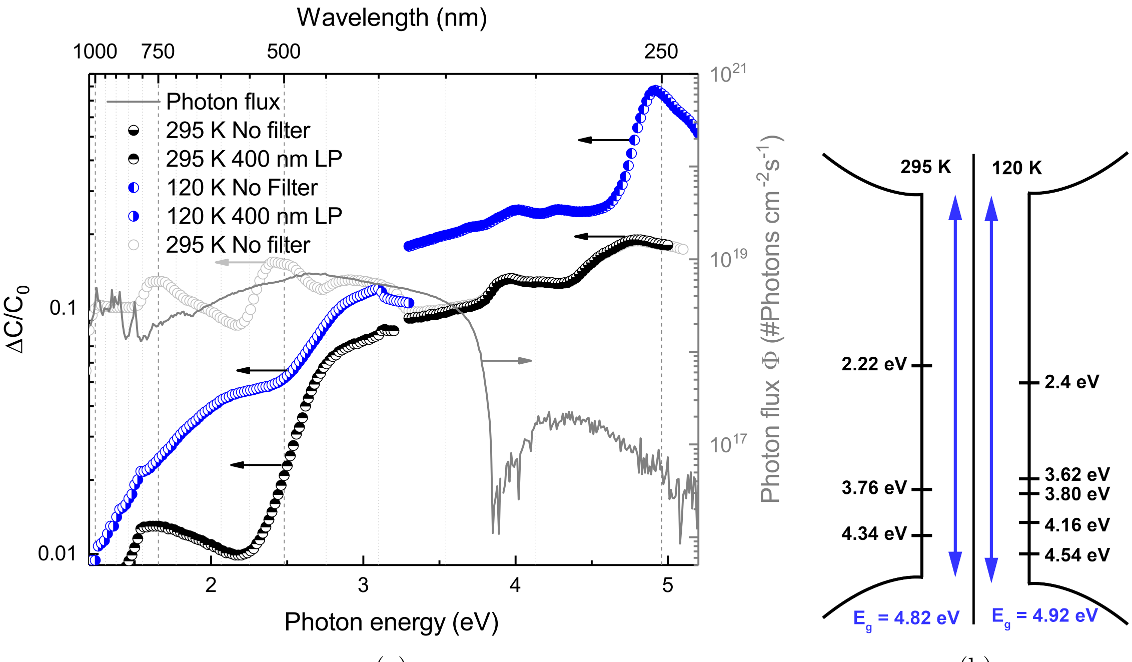

(a)

(b)

Figure 50: (a) SSPC results obtained after proton irradiation(left y-axis) and photon flux(right y-axis). Deviations between high and low temperature measurements suggest that thermal processes influence the SSPC signal, thus low temperatures is required to fulfill the assumption that $e_n^{th} \ll e_n^o$. (b) Illustration of the defect levels obtained from onsets in the SSPC spectrum in (a) at 120 K and 295 K

### 4.2.2 ZnO

For further verification of the online-system using an alternative material system. IV,CV, DLTS and SSPC measurements on ZnO were conducted. Contacts were deposited with shadow masks as described in section 4.1.2.1, with 15 nm + 150 nm Pd as front contact and 10 nm Ti + 150 nm Al back contact. The sample was cleaned in boiling $H_2O_2$ before front contact deposition.

#### 4.2.2.1 IV/CV - Contact quality

It is known that obtaining highly rectifying contacts in ZnO is challenging[34], where 2-3 orders of magnitude rectification is normally achieved. Room temperature IV measurements states rectification of only 1 order of magnitude, as can be seen in Fig.51a. Reduced rectification is also seen at 120 K. The reduced rectification can be due to the cleaning procedure that causes a roughening of the sample surface, which is not beneficial when depositing thin contacts. The main culprit seems to be shunt resistance $R_{sh}$

CV measurements show non-linear behaviour when displayed as $1/C^2$ versus voltage, which is not ideal for a Schottky contact when $N_d$ is assumed to be uniform. An almost linear region however, can be observed around −4 V reverse bias. Although IV and CV show poor rectification and capacitance behaviour, the contacts are worthwhile to test out on the system under −4 V reverse bias.

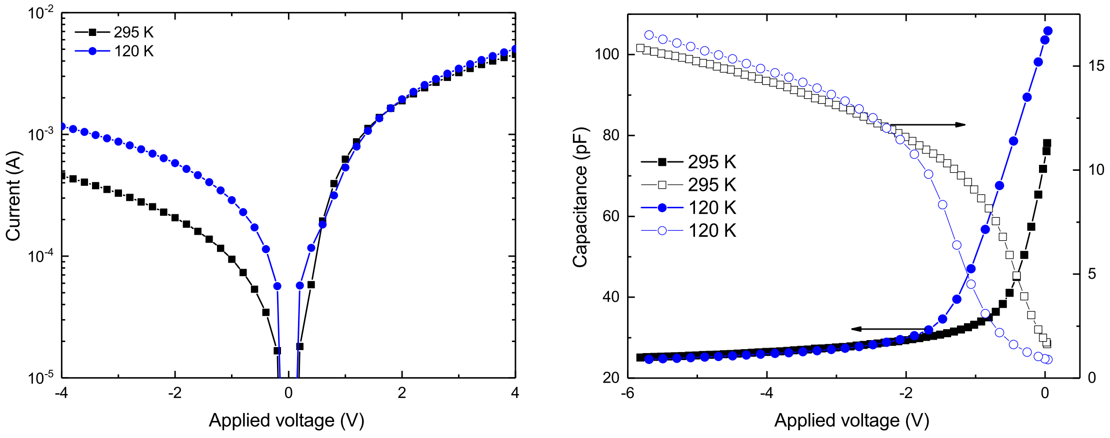

(a) (b)

Figure 51: Results from (a) IV and (b) CV measurements on ZnO at

#### 4.2.2.2 DLTS - Electrically active deep defects

Although IV/CV measurements reveal poor contact performance, DLTS measurements show spectra similar to previous reports on ZnO. The strong signal peak of the DLTS spectrum in Fig.52a is known from earlier reports as the E3 level in ZnO [35]. Several origins of the E3 peak has been reported, including oxygen vacancies and extrinsic impurities. More recent studies suggest that the E3 peak is hydrogen related, where $V_{Zn}$-3H is a potential candidate [36]. This being said, identification of these defect levels are out of scope of this thesis.

#### 4.2.2.3 SSPC - Optically active deep defects

In Figure 53 SSPC measurements on ZnO is shown. It is apparent that measurements at 120 K show response from band gap excitation at 3.34 eV as expected. No other signal response can be observed within the band gap, verifying that no effects of second harmonics

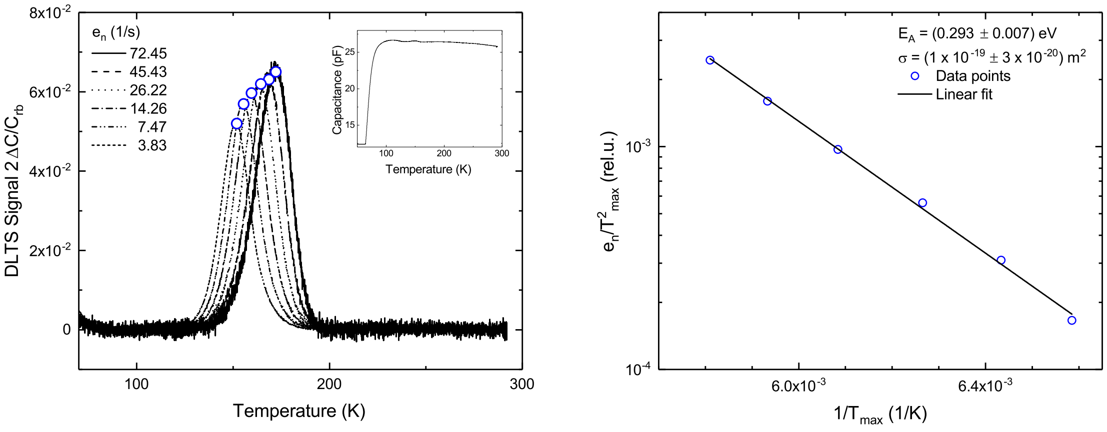

(a) (b)

Figure 52: (a) DLTS spectrum and (b) Arrhenius plot from DLTS measurements on ZnO

is introduced. This further confirms that the features seen in the SSPC measurements on the Ga2O3 sample arise from the material and not the setup, which was an important motivation for the ZnO measurements. Room temperature measurements on no signal for electron excitation, thus confirming that low temperature is needed to suppress thermal processes.

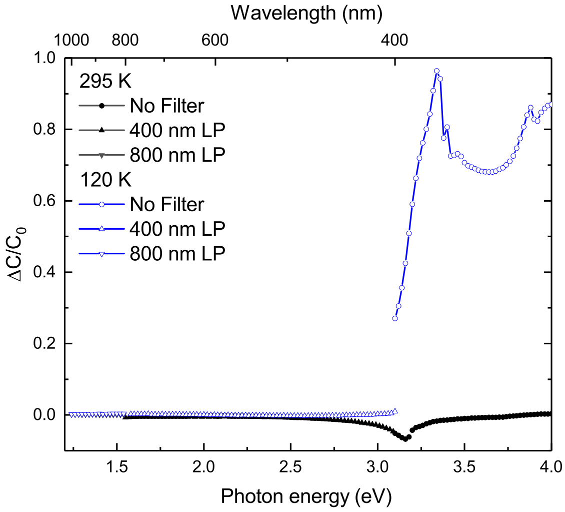

Figure 53: Results from SSPC measurements on ZnO at 120 K and 295 K. Measurements were conducted with two longpass filters (400 nm and 800 nm) to filter out possible effects from second harmonics. At 120 Ka band gap response from ZnO was obtained

# 5 Summary and conclusion

The objective of this master's project was to extend the online characterization capabilities which can be utilized at the MeV ion accelerator located at MiNaLab. More specifically, the task was to integrate optical excitation at variable wavelength into the existing online electrical characterization setup. The existing online electrical characterization setup was already capable to perform a host of different electrical measurements such as Capacitance-Voltage measurements or deep-level transient spectroscopy. The initial setup consisted of a vacuum chamber connected to the beam line of a MeV ion accelerator. Inside the vacuum chamber a sample holder was connected to a cryopump to enable low temperature measurements as well as ion implantation/irradiation at low temperatures. In order to perform the previously mentioned electrical measurements, the sample mounted on the sample holder inside the vacuum chamber could be electrically connected to electrical measurement devices outside the chamber itself. By making optical excitation at variable wavelength available, junction spectroscopy techniques such as steady-state photocapacitance measurement as well as deep-level optical spectroscopy can be utilized in the future.

As presented in the previous chapters, the experimental capabilities of the initial online setup were, indeed, successfully expanded by an optical excitation system with variable wavelength. To achieve this goal, a broad-band light source and a monochromator were integrated into a single unit to function as a light source operating at variable wavelength. Using off-axis parabolic mirrors and a sapphire window at one of the vacuum chamber ports, a light delivery system was developed to enable illumination of samples within the vacuum chamber. Further development was done to manufacture samples which are suitable for junction spectroscopy, where rectifying junctions are needed, and sufficiently transparent for the optical excitation. This goal was achieved by designing a new contact design for Schottky junctions and developing the tools to manufacture such contacts. To enable junction spectroscopy measurements using optical excitation, LabVIEW programs were developed. As a starting point measurement software for steady-state photocapacitance measurements was written.

After build-up of all the hardware and development of the software, intensive testing of the newly developed hardware and software was undertaken. The tests performed, include testing the spectral distribution and power output of the optical excitation system. Here, parameters such as spectral resolution and photon flux are of importance. It could be shown that in the photon energy range between 2.4 eV to 5 eV a resolution of about 10-20 m eV and photon fluxes between $10^{16}\,\mathrm{cm}^{-2}\,\mathrm{s}^{-1}$ to $10^{19}\,\mathrm{cm}^{-2}\,\mathrm{s}^{-1}$ at the sample position could be achieved. Furthermore, the setup was tested for possible artifacts. Corresponding studies revealed that especially second order effects due to the use of a grating monochromator have to be taken into account. Such artifacts were mitigated by introducing a filter assembly in the beam path of the light delivery system.

A crucial test for the newly developed system was to perform steady-state photocapacitance measurements on $\beta$-$Ga_2O_3$ and ZnO samples. These measurements revealed, that indeed physical signatures can be seen in SSPC measurements, when using the newly developed system on these oxide semiconductors. For both materials, it was evident that low temperature measurements are paramount when performing SSPC.

Last but not least, preliminary measurements were performed on $\beta$-$Ga_2O_3$ to unveil the potential of the newly developed setup for further defect studies. For this purpose, SSPC measurements at low temperatures were performed before and after proton irradiation of the samples at low temperatures. Besides a clear response originating from the band gap of $\beta$-$Ga_2O_3$ , optically-induced responses were also seen for lower photon energies at around 2.40 eV, 3.62 eV, 3.80 eV, 4.16 eV and 4.54 eV at 120 K, and 2.22 eV, 3.76 eV and 4.34 eV at 295 K, indicating the presence of several optically- and electrically active signatures in the material, that can be studied with the newly developed system. The preliminary study conducted here does not clearly show any significant changes regarding the SSPC spectra before and after irradiation, but paves the way for further in-depth studies.

## 5.1 Outlook

The further developtment of the setup can roughly be divided into two parts. Firstly, there is room for developtments concerning the software side. Secondly, there is also significant potential for further development regarding the hardware side of the setup.

On the software side, the existing SSPC software can be developed further by implementing a dynamic steady-state measurement with a non-static illumination time, determined by the derivative of the capacitance versus time, rather than a fixed value. Changing from software- to hardware timed data acquisition, optically induced transients can be captured for DLOS program development. Furthermore, it can be interesting to include constant light illumination into regular DLTS measurements. User-friendliness can also be improved by packing multiple programs in one main program.

On the hardware side, there is potential for improvements of the current system as well as potential for the development of more advanced techniques utilizing the newly developed optical excitation system. Utilizing capabilities of the monochromatic system, routing light on to the optical table, new experimental setups can be developed, while simultaneously using the online-chamber for electrical measurements. Achieving lower temperatures would be beneficial and could be achieved by refurbishing the old cryostat.

On the side of samples used in the online system, further studies on contact manufacturing could be conducted to achieve higher quality contacts.

# A Mechanical drawings

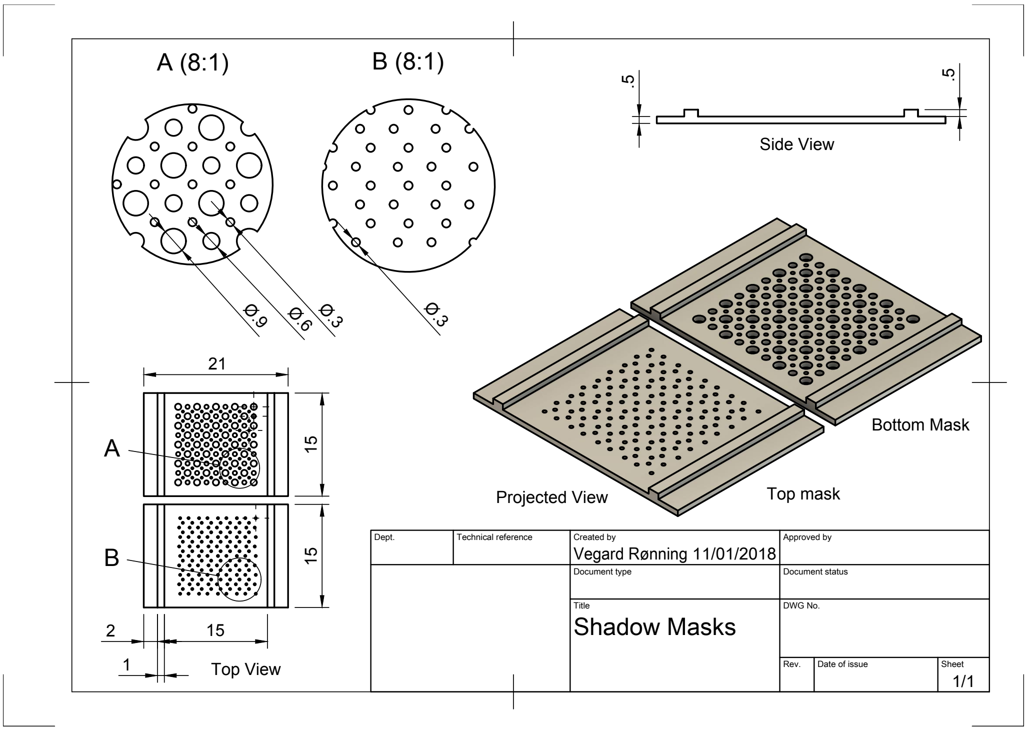

Figure 54: Sequence diagram

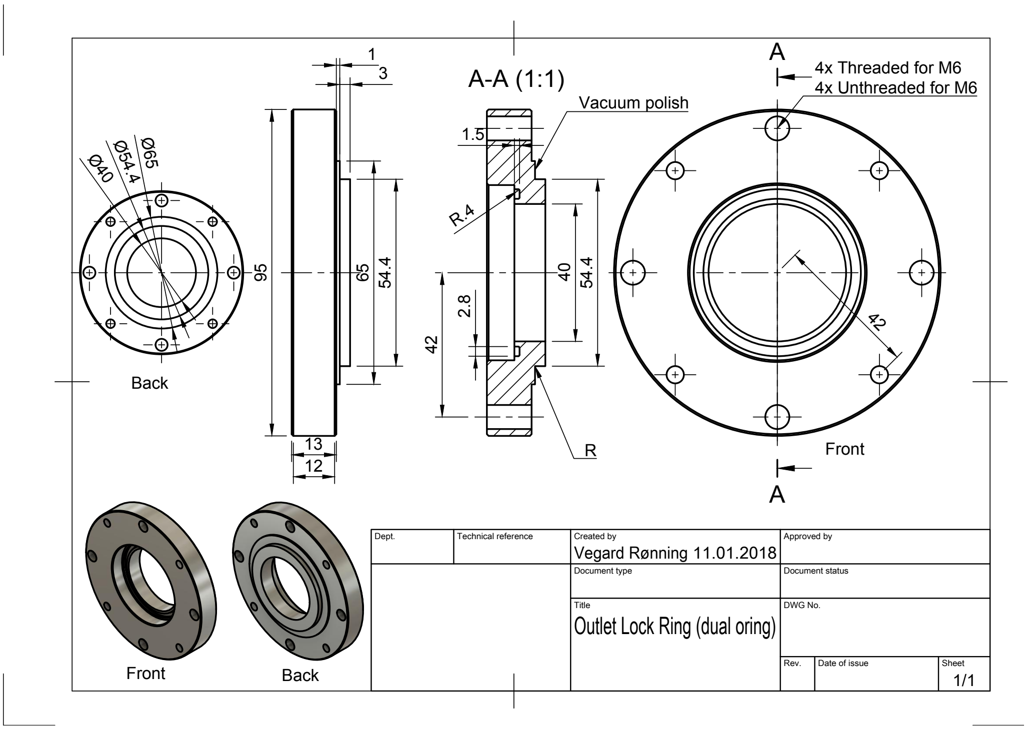

Figure 55: Caption

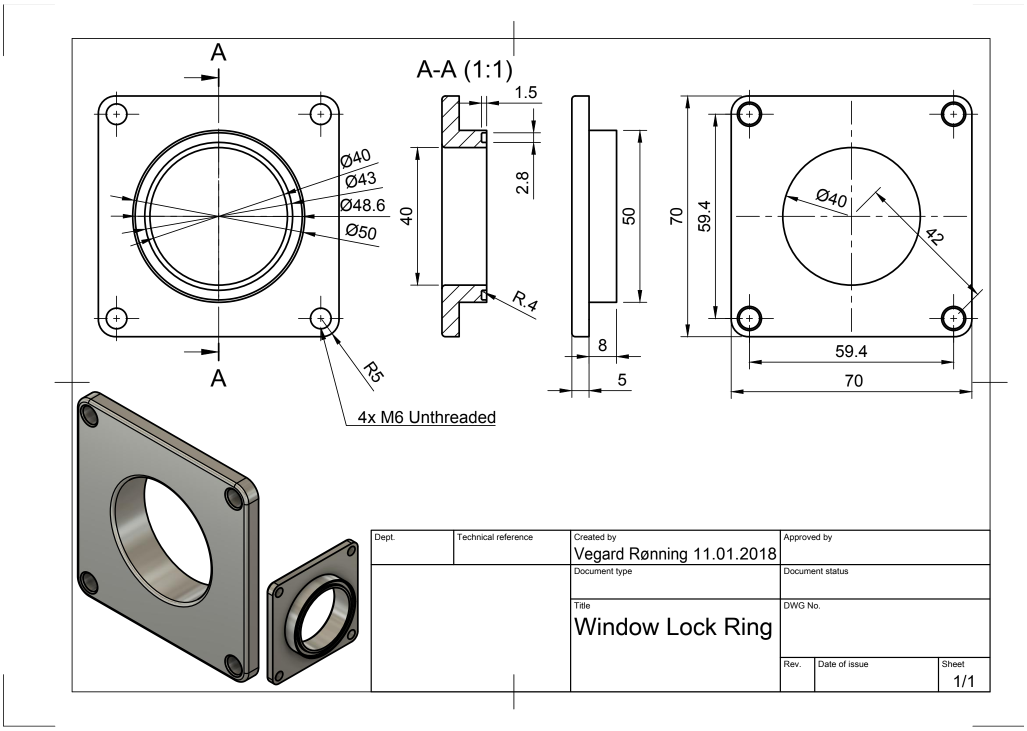

Figure 56: Caption

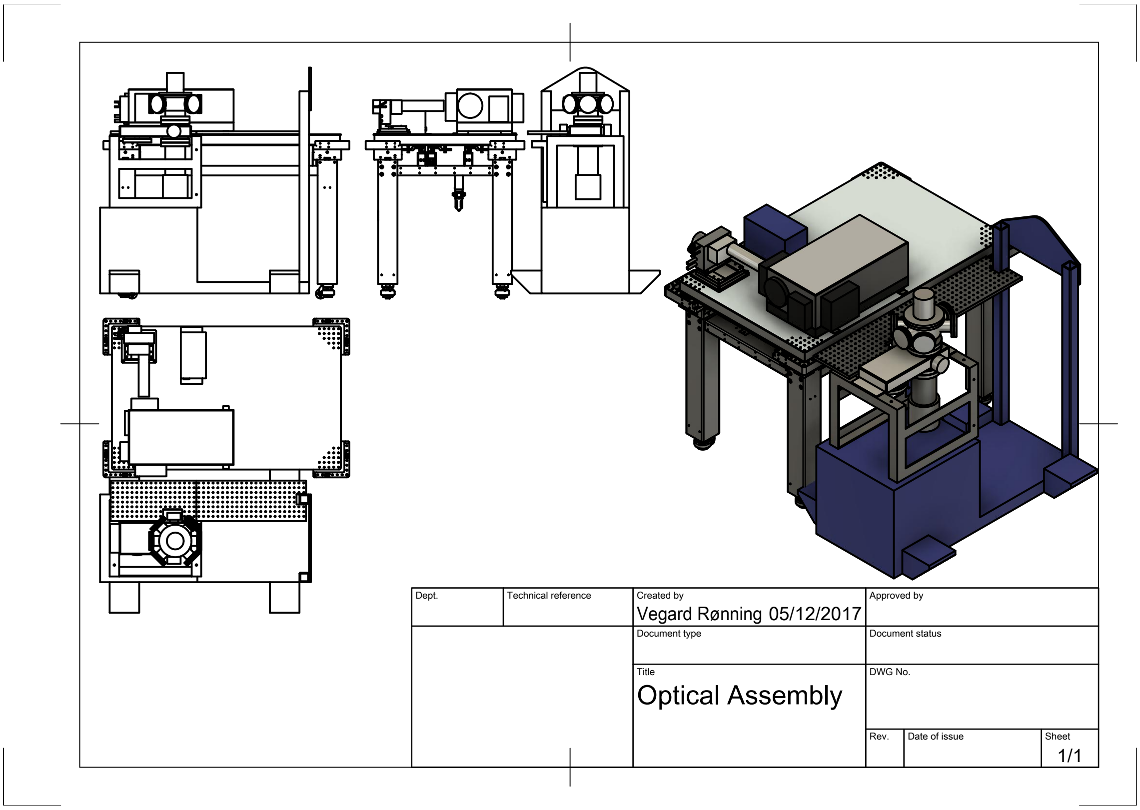

Figure 57: Sequence diagram

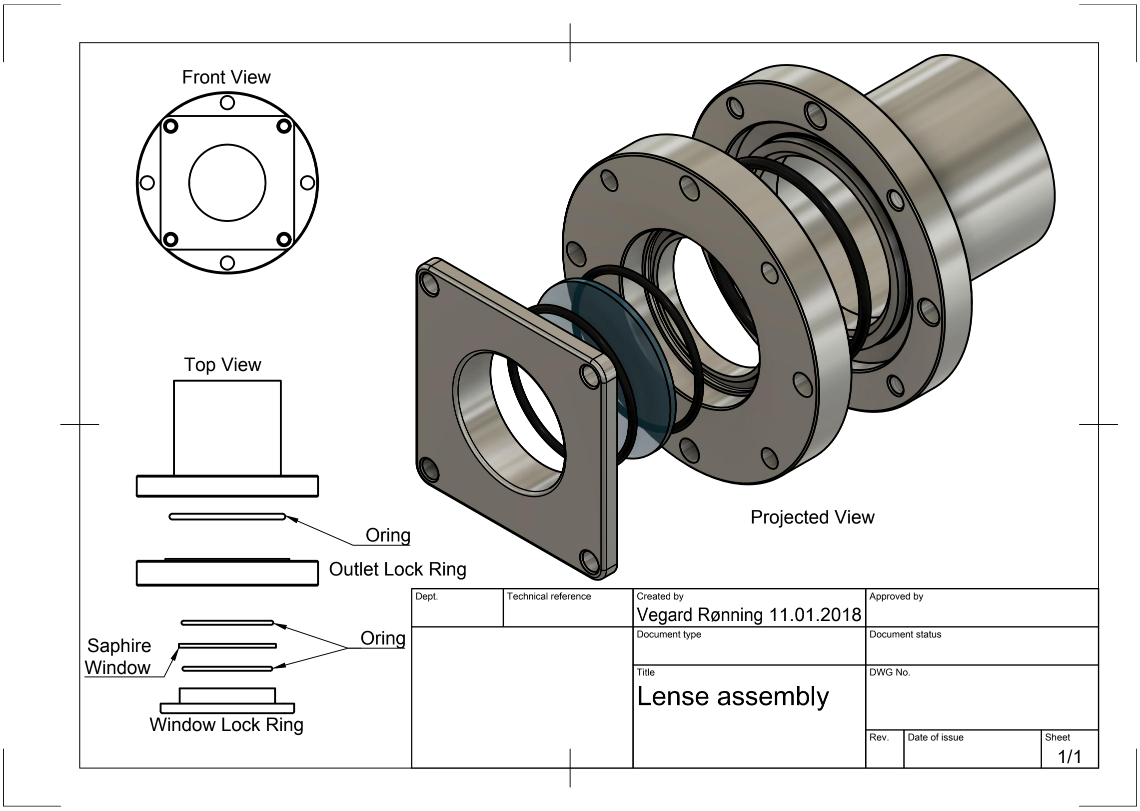

Figure 58: Sequence diagram

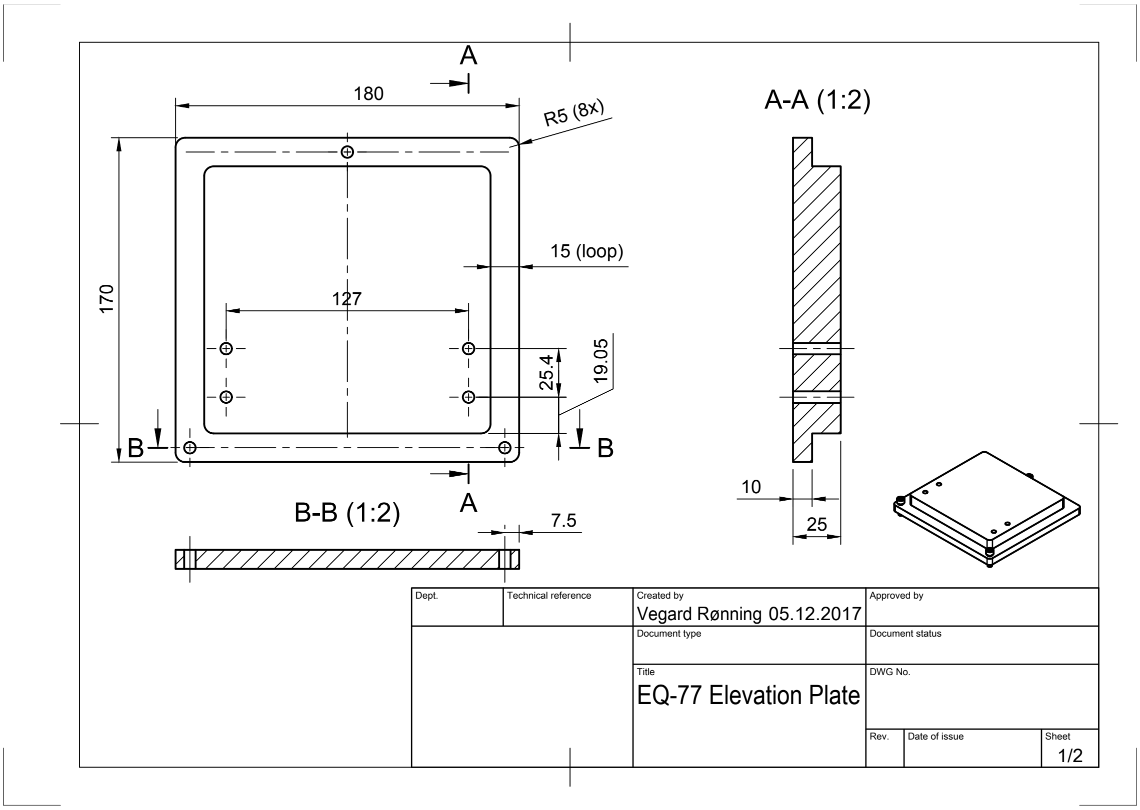

Figure 59: Sequence diagram

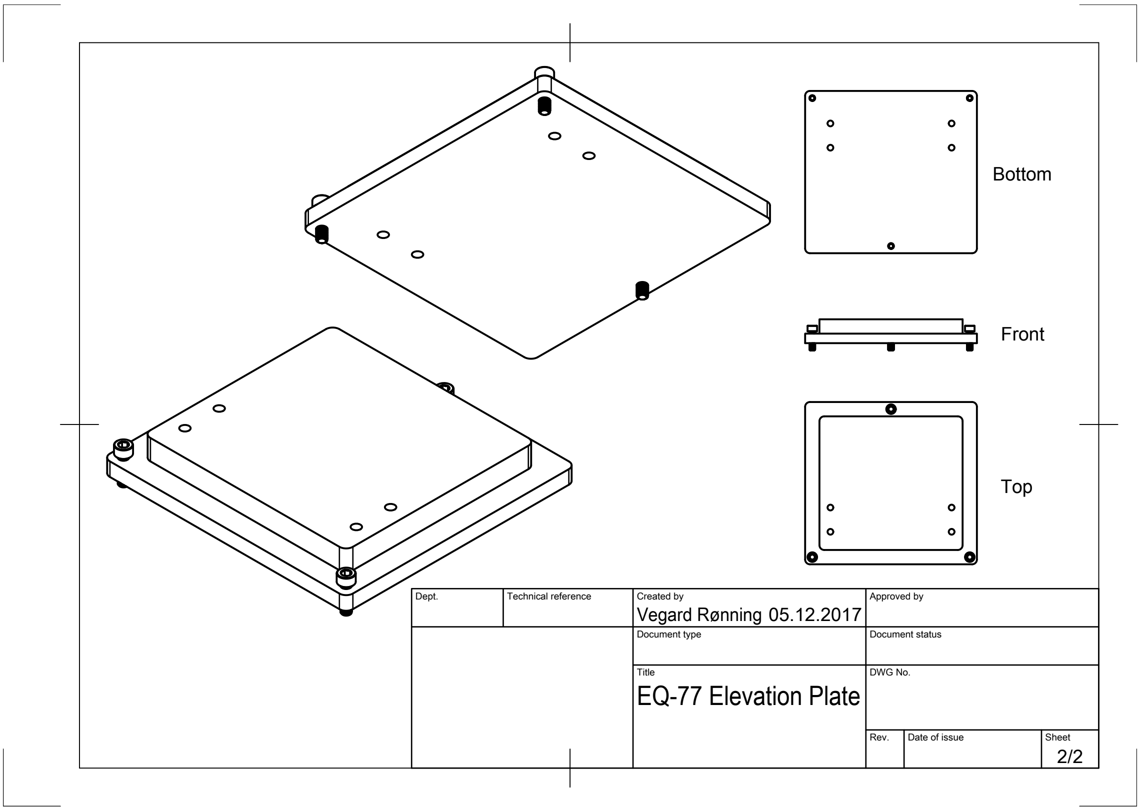

Figure 60: Sequence diagram

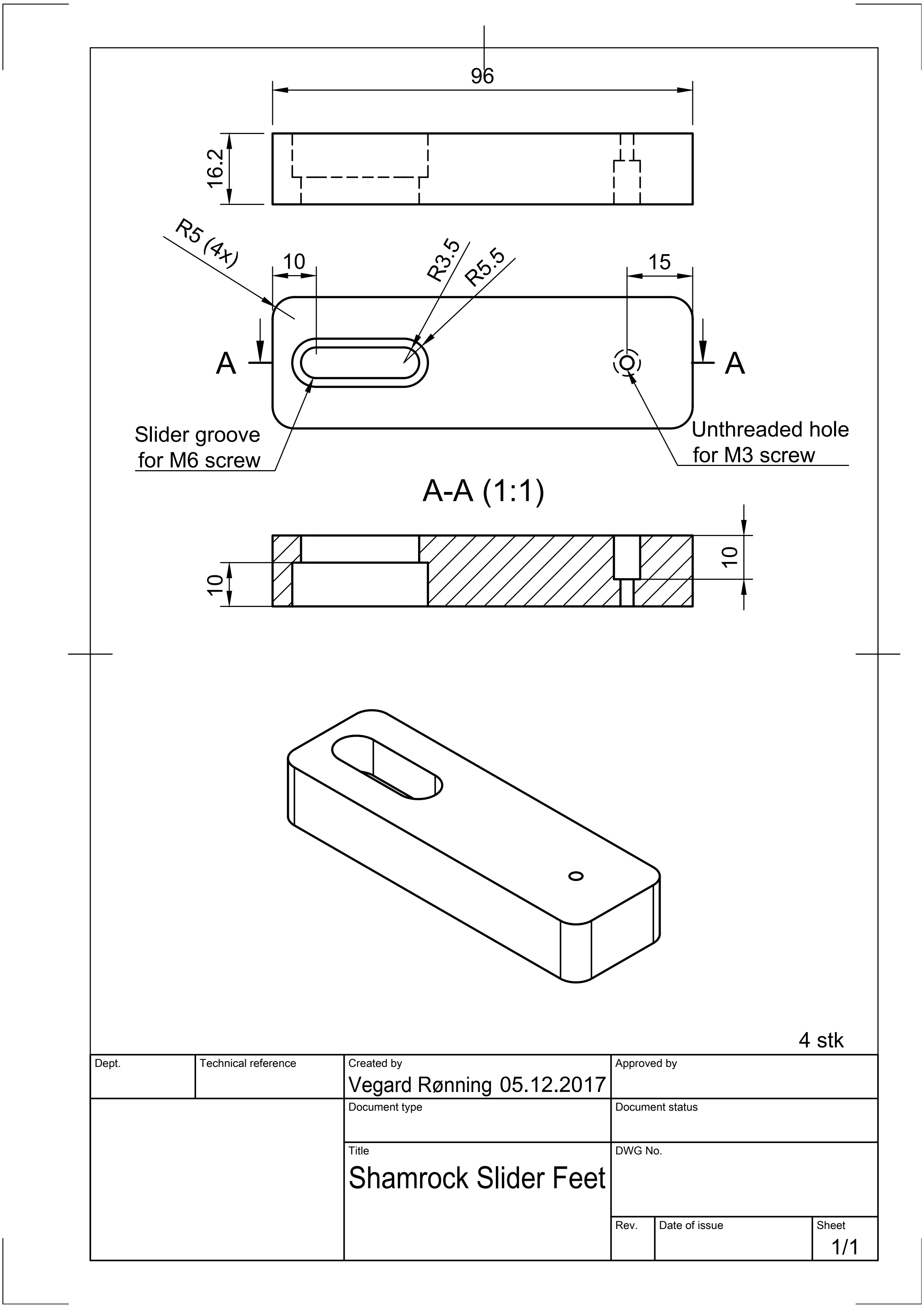

Figure 61: Sequence diagram

# B Illustrations

All optical components from Thorlabs and Newport was acquired from the company website [20, 21]

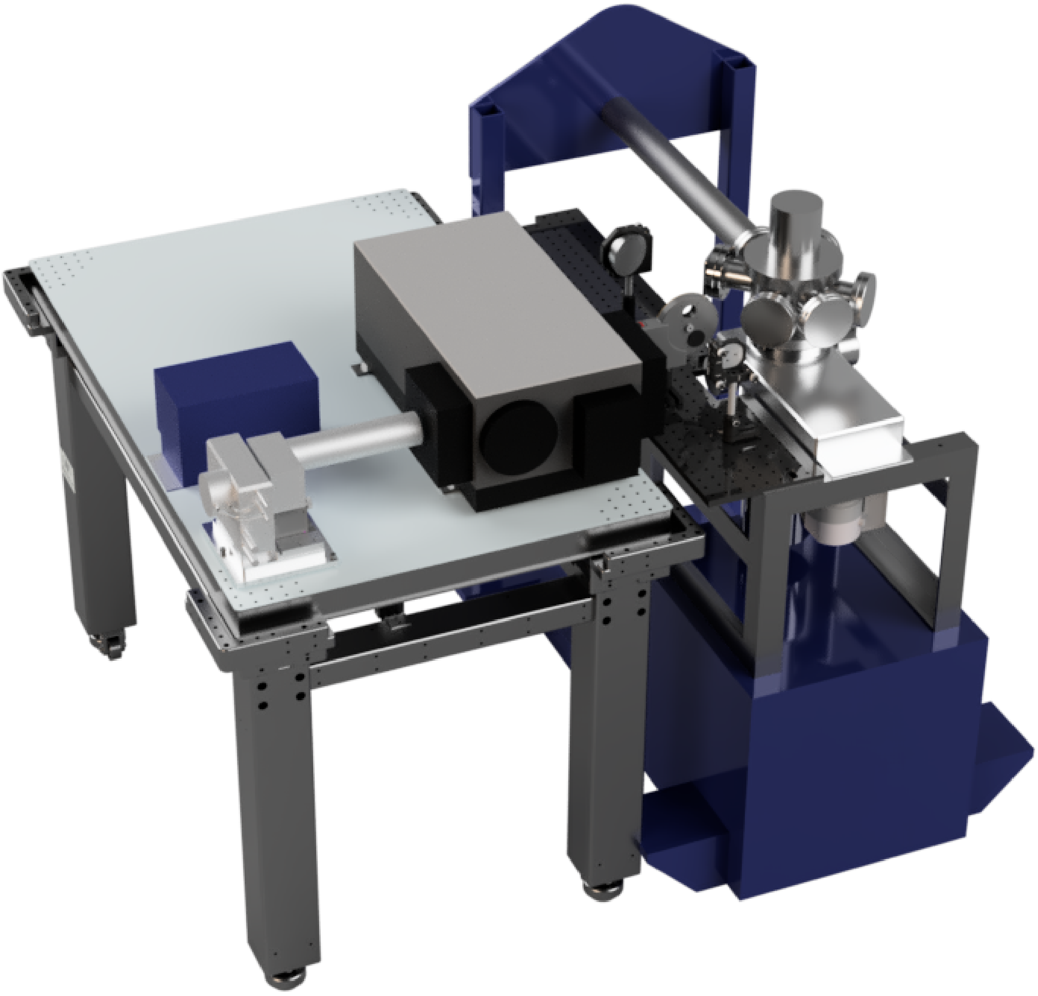

Figure 62

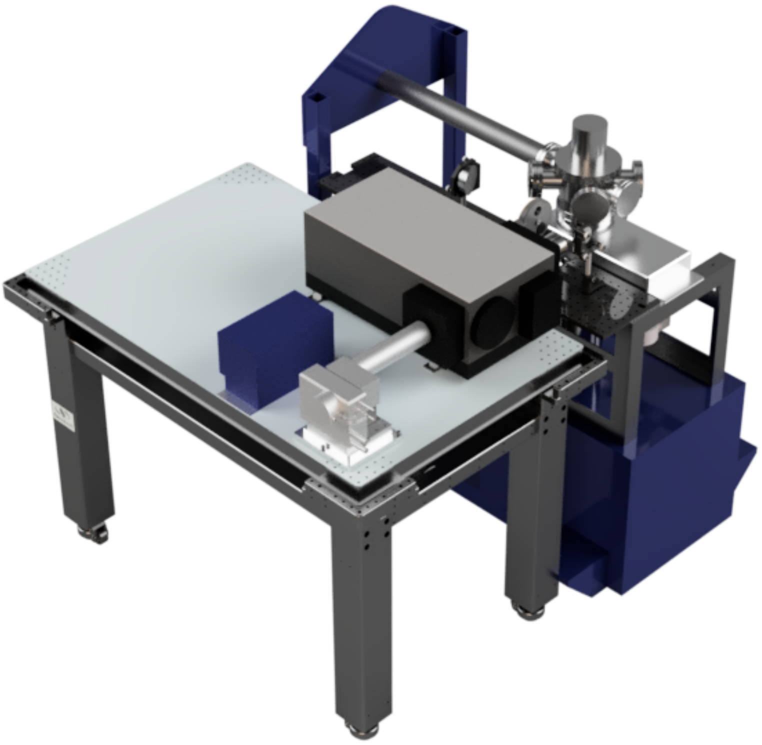

Figure 63

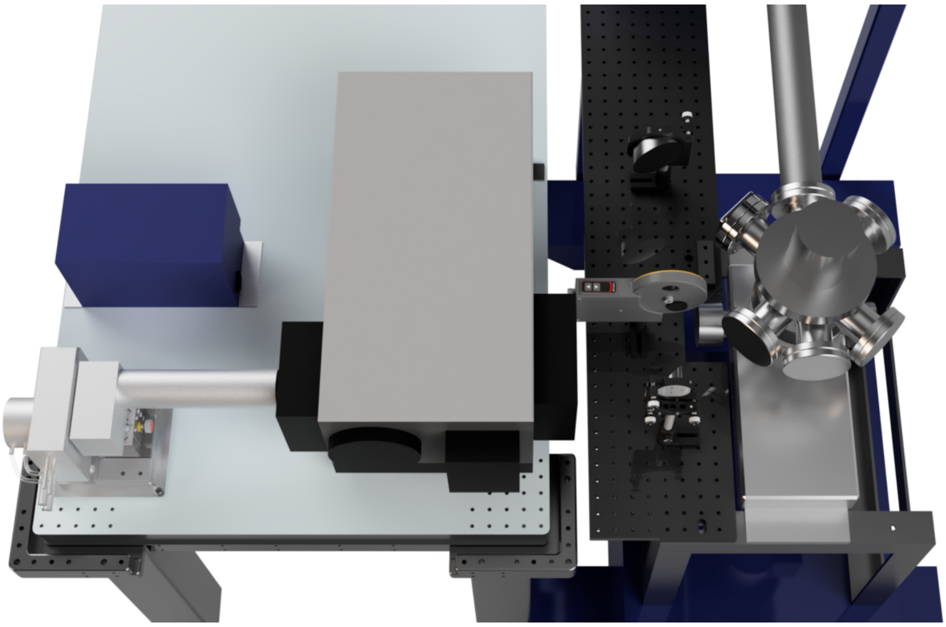

Figure 64

# C Data Sheets

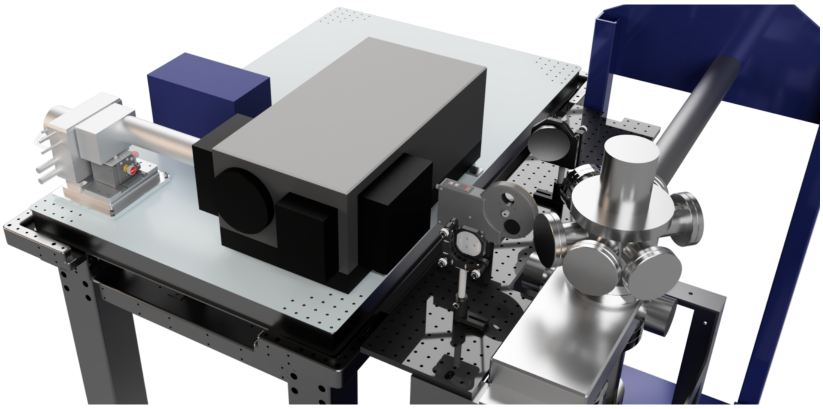

Figure 65

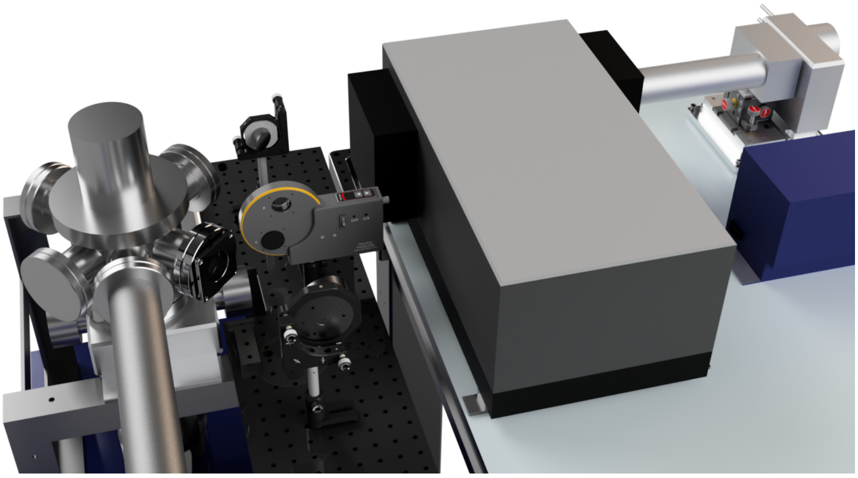

Figure 66

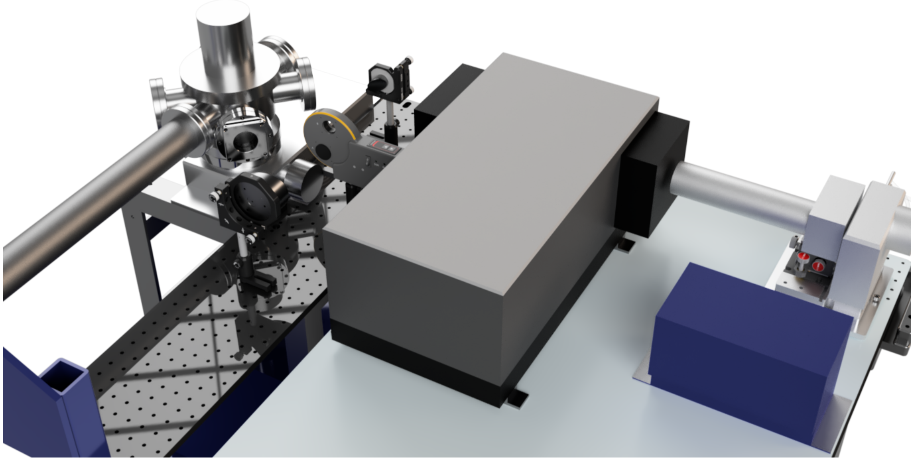

Figure 67

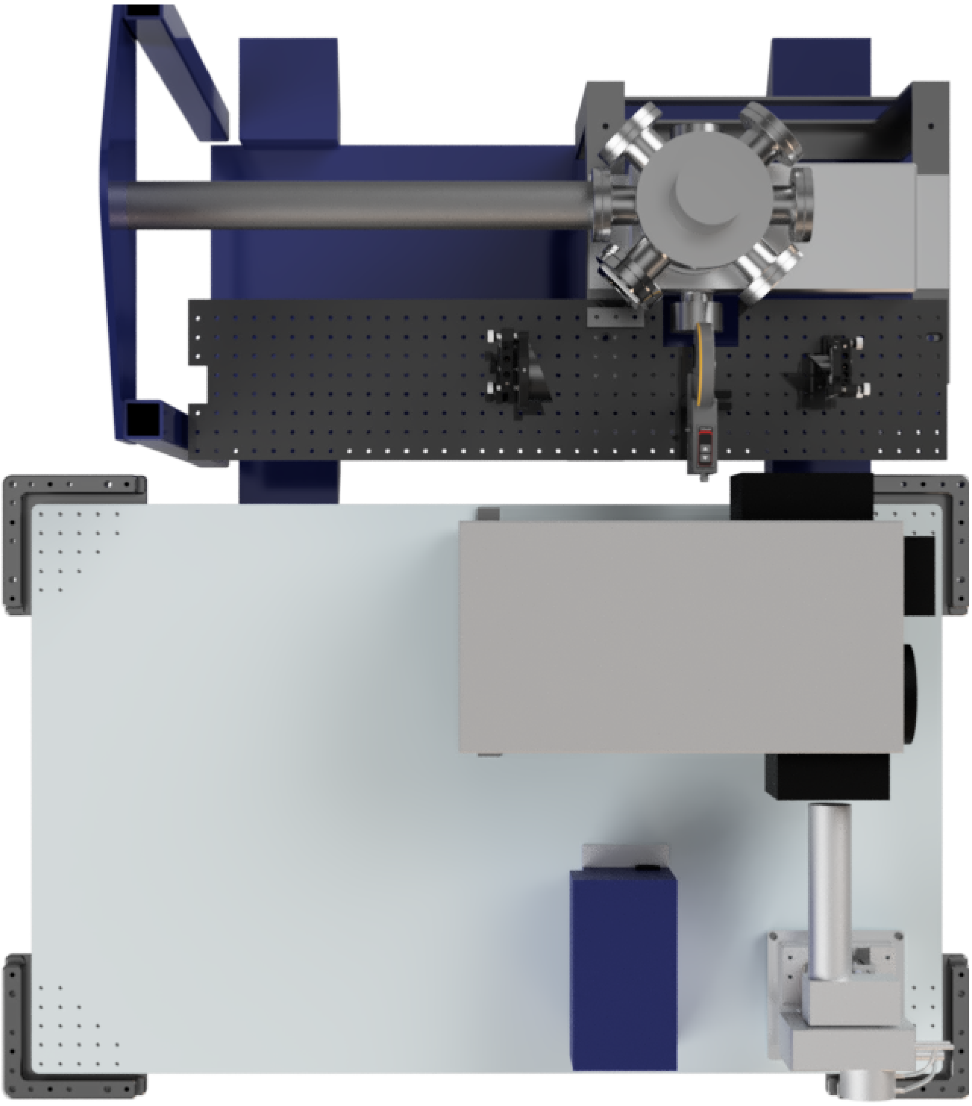

Figure 68

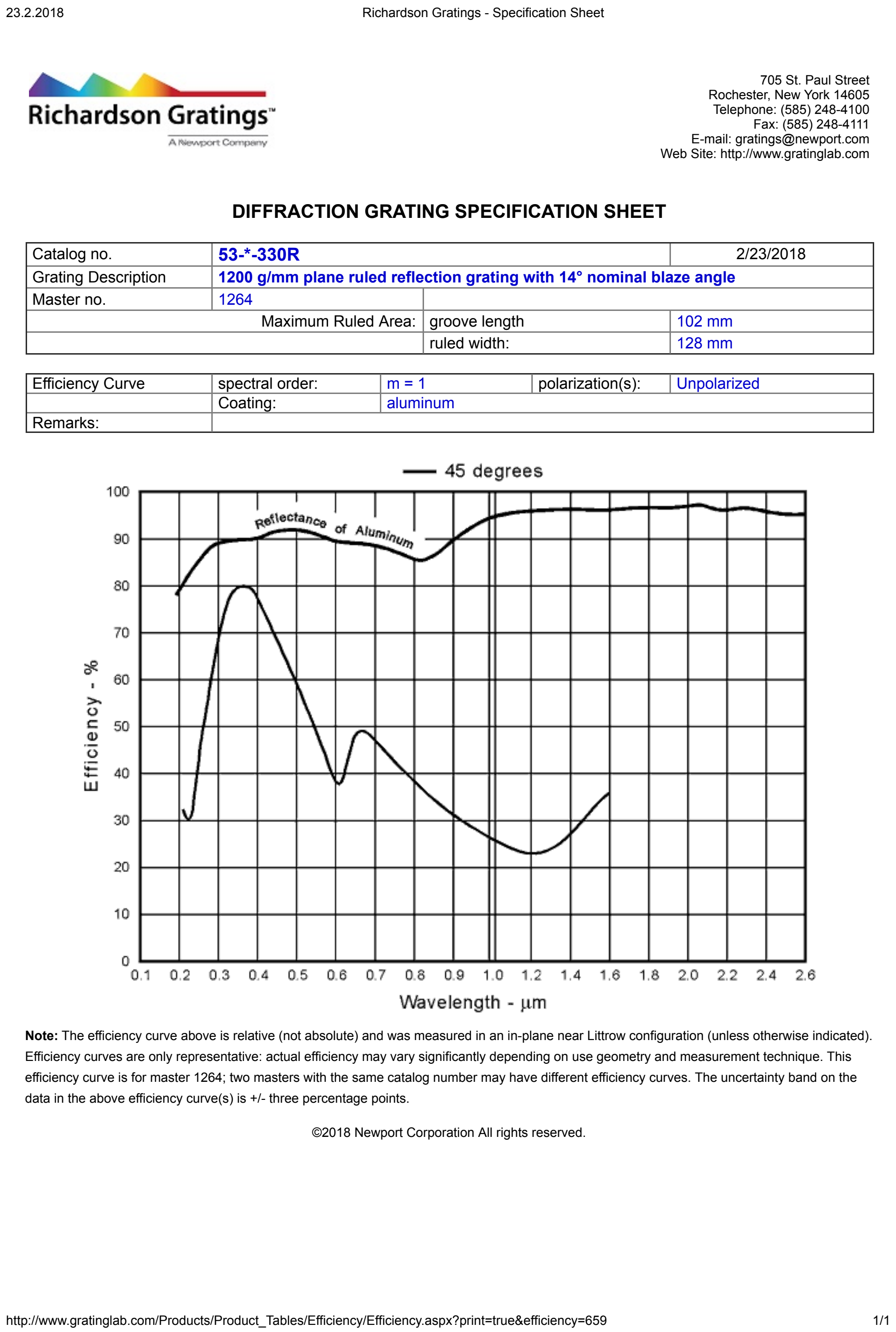

23.2.2018 Richardson Gratings - Specification Sheet

Richardson Gratings™
A Newport Company

705 St. Paul Street
Rochester, New York 14605
Telephone: (585) 248-4100
Fax: (585) 248-4111
E-mail: gratings@newport.com
Web Site: http://www.gratinglab.com

**DIFFRACTION GRATING SPECIFICATION SHEET**

| | | | |
|---|---|---|---|
| Catalog no. | **53-*-330R** | | 2/23/2018 |
| Grating Description | **1200 g/mm plane ruled reflection grating with 14° nominal blaze angle** | | |
| Master no. | 1264 | | |
| | Maximum Ruled Area: | groove length | 102 mm |
| | | ruled width: | 128 mm |

| | | | | |
|---|---|---|---|---|
| Efficiency Curve | spectral order: | m = 1 | polarization(s): | Unpolarized |
| | Coating: | aluminum | | |
| Remarks: | | | | |

**Note:** The efficiency curve above is relative (not absolute) and was measured in an in-plane near Littrow configuration (unless otherwise indicated). Efficiency curves are only representative: actual efficiency may vary significantly depending on use geometry and measurement technique. This efficiency curve is for master 1264; two masters with the same catalog number may have different efficiency curves. The uncertainty band on the data in the above efficiency curve(s) is +/- three percentage points.

©2018 Newport Corporation All rights reserved.

http://www.gratinglab.com/Products/Product_Tables/Efficiency/Efficiency.aspx?print=true&efficiency=659 1/1

Figure 69: Caption

# References

[1] Energy - United Nations Sustainable Development. URL `https://www.un.org/sustainabledevelopment/energy/`.

[2] Ben G Streetman. *Solid state electronic devices.* Pearson, seventh ed edition, 2015. ISBN 9780133356038.

[3] Charles Kittel. *Introduction to solid state physics.* Wiley, Hoboken, N.J, 8th ed. edition, 2005. ISBN 9780471415268.

[4] P Blood. *The electrical characterization of semiconductors : majority carriers and electron states*, volume 14 of *Techniques of physics.* Academic Press, London, 1992. ISBN 0125286279.

[5] G. Lucovsky. On the photoionization of deep impurity centers in semiconductors. *Solid State Communications*, 88(11-12):879–882, 12 1993. ISSN 0038-1098. doi: 10.1016/0038-1098(93)90261-K. URL `https://www.sciencedirect.com/science/article/pii/003810989390261K`.

[6] John Bardeen. Surface States and Rectification at a Metal Semi-Conductor Contact. *Physical Review*, 71(10):717–727, 5 1947. ISSN 0031-899X. doi: 10.1103/PhysRev.71.717. URL `https://link.aps.org/doi/10.1103/PhysRev.71.717`.

[7] S. Geller. Crystal Structure of $\beta$-Ga ¡sub¿2¡/sub¿ O ¡sub¿3¡/sub¿. *The Journal of Chemical Physics*, 33(3):676–684, 9 1960. ISSN 0021-9606. doi: 10.1063/1.1731237. URL `http://aip.scitation.org/doi/10.1063/1.1731237`.

[8] J. Åhman, G. Svensson, and J. Albertsson. A Reinvestigation of $\beta$-Gallium Oxide. *Acta Crystallographica Section C Crystal Structure Communications*, 52(6):1336–1338, 6 1996. ISSN 01082701. doi: 10.1107/S0108270195016404. URL `http://scripts.iucr.org/cgi-bin/paper?S0108270195016404`.

[9] A E Romanov, S I Stepanov, V I Nikolaev, and V E Bougrov. Gallium Oxide: Properties and Applica 4 98 a Review. *Rev. Adv. Mater. Sci*, 44:63–86, 2016.

[10] D. V. Lang. Deep-level transient spectroscopy: A new method to characterize traps in semiconductors. *Journal of Applied Physics*, 45(7):3023–3032, 7 1974. ISSN 0021-8979. doi: 10.1063/1.1663719. URL `http://aip.scitation.org/doi/10.1063/1.1663719`.

[11] A. Chantre, G Vincent, and D. Bois. Deep-level optical spectroscopy in GaAs. *Physical Review B*, 23(10):5335–5359, 1981. ISSN 01631829. doi: 10.1103/PhysRevB.23.5335. URL `https://journals.aps.org/prb/pdf/10.1103/PhysRevB.23.5335`.

[12] LabVIEW 2018 - National Instruments. URL `http://www.ni.com/en-no/shop/labview/labview-details.html`.

[13] National Instrument. Introduction to Data Acquisition - National Instruments, . URL `http://www.ni.com/white-paper/3536/en/`.

[14] National Instrument. Using a State Machine (Event Driven) Architecture - National Instruments, . URL `http://www.ni.com/white-paper/2926/en/`.

[15] John E. Mahan. *Physical vapor deposition of thin films.* Wiley, 2000. ISBN 0471330019.

[16] D. M. Mattox. *Handbook of physical vapor deposition (PVD) processing.* William Andrew, 2010. ISBN 9780815520382.

[17] Stephen A. Campbell. *Engineering at the Micro- and Nanoscale.* 2008. ISBN 9780195320176.

[18] James F. Ziegler. James Ziegler - SRIM &amp; TRIM. URL `http://www.srim.org/`.

[19] Autodesk — 3D Design, Engineering &amp; Entertainment Software. URL `https://www.autodesk.com/`.

[20] Newport. Newport - Photonics Solutions for Extending the Frontiers of Science. URL `https://www.newport.com/`.

[21] ThorLabs. Thorlabs, Inc. - Your Source for Fiber Optics, Laser Diodes, Optical Instrumentation and Polarization Measurement &amp; Control. URL `https://www.thorlabs.com/`.

[22] Edwards. WRG-S-NW25. URL `https://shop.edwardsvacuum.com/products/d14701000/view.aspx`.

[23] OTTO OLSEN AS. URL `http://www.oo.no/mediabank/store/2/2914/Tetninger.pdf`.

[24] M. E. Ingebrigtsen, J. B. Varley, A. Yu. Kuznetsov, B. G. Svensson, G. Alfieri, A. Mihaila, U. Badstübner, and L. Vines. Iron and intrinsic deep level states in Ga ¡sub¿2¡/sub¿ O ¡sub¿3¡/sub¿. *Applied Physics Letters*, 112(4):042104, 1 2018. ISSN 0003-6951. doi: 10.1063/1.5020134. URL `http://aip.scitation.org/doi/10.1063/1.5020134`.

[25] Energetiq Technology Inc. EQ-77 LDLS$^{\mathrm{TM}}$ Data Sheet. URL `https://www.energetiq.com/DataSheets/EQ77-data-sheet.pdf`.

[26] Energetiq. Energetiq - Application Note - PEEM. URL `https://www.energetiq.com/TechLibrary/Application_Notes/FAQs/FAQs.html`.

[27] Thorlabs. UV Fused Silica, Optical Substrates. URL `https://www.thorlabs.com/newgrouppage9.cfm?objectgroup_id=6973&tabname=UVFusedSilica`.

[28] Edmind optics. Off-Axis Parabolic Mirror Selection Guide — Edmund Optics. URL `https://www.edmundoptics.com/resources/application-notes/optics/off-axis-parabolic-mirror-selection-guide/`.

[29] Jose Pinto. Peixoto and Abraham H. Oort. *Physics of climate.* American Institute of Physics, 1992. ISBN 0883187124.

[30] K Irmscher, Z Galazka, M Pietsch, R Uecker, and R Fornari. Electrical properties of $\beta$-Ga 2 O 3 single crystals grown by the Czochralski method Electrical properties of b-Ga 2 O 3 single crystals grown by the Czochralski method. *Journal of Applied Physics Applied Physics Letters The Journal of Chemical Physics Applied Physics Letters*, 110(10):13504–142106, 2011. doi: 10.1063/1.3642962. URL `https://doi.org/10.1063/1.3642962http://aip.scitation.org/toc/jap/110/6`.

[31] Z Zhang, E Farzana, A R Arehart, and S A Ringel. Deep level defects throughout the bandgap of (010) $\beta$ Ga 2 O 3 detected by optically and thermally stimulated defect spectroscopy. *Citation: Appl. Phys. Lett. Applied Physics Letters Journal of Applied Physics Applied Physics Letters*, 1081(10):52105–13504, 2016. doi: 10.1063/1.

3642962. URL `https://doi.org/10.1063/1.4941429http://aip.scitation.org/toc/apl/108/5`.

[32] A Kurtz, A Hierro, M Lopez-Ponce, G Tabares, and J M Chauveau. Electrical mechanisms for carrier compensation in homoepitaxial nonpolar m-ZnO doped with nitrogen. *Semiconductor Science and Technology*, 31(3):035010, 3 2016. ISSN 0268-1242. doi: 10.1088/0268-1242/31/3/035010. URL `http://stacks.iop.org/0268-1242/31/i=3/a=035010?key=crossref.705632d6598c37ad93bf91f67b21aec8`.

[33] Z. Zhang, C. A. Hurni, A. R. Arehart, J. Yang, R. C. Myers, J. S. Speck, and S. A. Ringel. Deep traps in nonpolar m-plane GaN grown by ammonia-based molecular beam epitaxy. *Applied Physics Letters*, 100(5):052114, 1 2012. ISSN 0003-6951. doi: 10.1063/1.3682528. URL `http://aip.scitation.org/doi/10.1063/1.3682528`.

[34] R Schifano, E V Monakhov, U Grossner, and B G Svensson. Electrical characteristics of palladium Schottky contacts to hydrogen peroxide treated hydrothermally grown ZnO. *Citation: Appl. Phys. Lett. Applied Physics Letters Journal of Applied Physics contact Applied Physics Letters Journal of Applied Physics Journal of Applied Physics*, 91(109):112101–121301, 1935. doi: 10.1063/1.2806194. URL `https://doi.org/10.1063/1.2806194http://aip.scitation.org/toc/apl/91/19`.

[35] F D Auret, S A Goodman, M J Legodi, W E Meyer, and D C Look. Electrical characterization of vapor-phase-grown single-crystal ZnO Green luminescent center in undoped zinc oxide films deposited on silicon substrates Electrical characterization of vapor-phase-grown single-crystal ZnO. *Citation: Appl. Phys. Lett. Journal of Applied Physics Journal of Applied Physics Journal of Applied Physics Defects in ZnO Journal of Applied Physics Applied Physics Letters ZnO Applied Physics Letters*, 80(10):1340–41301, 2002. doi: 10.1063/1.1452781. URL `https://doi.org/10.1063/1.1452781http://aip.scitation.org/toc/apl/80/8`.

[36] A. Hupfer, C. Bhoodoo, L. Vines, and B. G. Svensson. The E3 center in zinc oxide: Evidence for involvement of hydrogen. *Applied Physics Letters*, 104(9):092111, 3 2014. ISSN 0003-6951. doi: 10.1063/1.4867908. URL `http://aip.scitation.org/doi/10.1063/1.4867908`.